

The Two Point Correlation Structure of a Cylinder Wake

Nicholas Joseph Molinaro

Thesis submitted to the faculty of the Virginia Polytechnic Institute and State University in
partial fulfillment of the requirements for the degree of

Master of Science

in

Aerospace Engineering

William J. Devenport

W. Nathan Alexander

K. Todd Lowe

05/1/2017

Blacksburg, Virginia

Keywords: turbulence, wake flows, two-point correlation, proper orthogonal decomposition,
compact eddy structure

The Two Point Correlation Structure of a Cylinder Wake

Nicholas Joseph Molinaro

Abstract

In this study the complete four dimensional space time correlation function was measured in the wake of an untripped circular cylinder at a Reynolds number of 60 000. This correlation serves as the complete inflow boundary condition for an open rotor ingesting inhomogeneous turbulence. An important aspect of the turbulence ingestion problem is understanding how different inflow boundary conditions effect the sound produced by a rotor. In the present study the turbulence structure of two plane wakes were compared. Measurements completed by a previous study in the wake of a NACA 0012 airfoil were compared with the measurements completed by the present study in the wake of a cylinder. The mean flows of both plane wakes were found to be very similar, however the Reynolds stress profiles show that the cylinder wake is substantially more turbulent. The structures of the two-point correlation function in each wake are also similar, although the cylinder wake had greater maximum correlation values and was correlated at greater separations. The two-point correlation was used along with proper orthogonal decomposition to compute the average instantaneous velocity fields of both wake flows. These velocity fields represent the average eddy structures present in each wake flow. The eddy structure comparisons show that the structures in the cylinder wake are larger and better correlated at longer time delays.

The Two Point Correlation Structure of a Cylinder Wake

Nicholas Joseph Molinaro

Abstract: General Audience

Any fan or propeller that ingests any unsteady flow will produce noise. This is especially important in propeller aircraft and marine vehicles where turbulence is generated from appendages on the vehicle's body. This self-generated turbulence travels downstream and is eventually drawn into the propeller and produces noise. The broad study that the present work is a part of is concerned with understanding this ingestion noise problem so that the interaction can be better modeled and the sound produced can be predicted. To predict the sound produced by a fan or propeller ingesting turbulence, detailed information about the inflow condition is needed. In the present study the turbulence structure of the wake shed by a circular cylinder at 20 meters per second. The two-point velocity correlation in the wake serves as the complete inflow condition for the turbulence ingestion problem. The structure of the cylinder wake inflow condition was compared with the structure of an airfoil wake to evaluate how the differences in the two flows would influence the sound produced by a rotor ingesting the two conditions. The two flows were found to be quite similar in the mean flow. The cylinder wake was found to be significantly more turbulent than the airfoil wake and was correlated over greater distances. This suggests that the structures in the cylinder wake are larger and remain coherent longer than those in the airfoil wake. The average instantaneous velocity fields were estimated in both wake flows and showed that the structures in the cylinder wake were significantly different from the structures in the airfoil wake. These flow structure comparisons show why the differences seen in the turbulence profiles and two-point correlations exist.

Acknowledgements

I would first like to thank my parents for their continued support throughout my undergraduate and graduate careers. Without their love and encouragement, I would not be in the position that I am in today. I also could not have done this without my girlfriend Kristina. She had to put up with me working at all hours of the day or night, especially when finishing my thesis. I would not have made it through graduate school without her constant support.

I would also like to thank Dr. William Devenport for all he has taught me throughout my time spent working with his research group. He taught me everything I know about aerodynamic testing, hotwire probes and the complex analysis methods that I would go on to use in my research. While working with Dr. Devenport I have certainly developed a greater appreciation for the amount of care required to conduct meaningful research and an important appreciation for the little accomplishments that lead toward the final result.

I would also like to thank my committee members Dr. Nathan Alexander and Dr. Todd Lowe for all they have taught me about being a good experimentalist and researcher.

I would like to thank Dr. Aurelien Borgoltz for teaching me how to repair hotwire probes. Fixing probes without the tips he gave me would have been even more painful.

I also would like to thank everyone in my research group including Liselle Joseph, Ian Clark, Anthony Millican, Christopher Hickling, Henry Murray and Agastya Balantrapu for all of their help in the hotwire measurements I made in several Stability Wind Tunnel test entries. We made a good team, and all of the measurements made would not have been possible without your help. During wind tunnel testing Tim Meyers and Bill Oetjens were invaluable in helping setup measurement systems and test models. I would also like to thank the AOE machine shop, specifically Andy Tawney, Cameron Hollandsworth and James Lambert. They saved me many times during testing when things went wrong.

Finally, I would like to thank the Office of Naval Research, specifically Dr. Ki-Han Kim, for their support of this research through grants N00014-14-1-0141 and N00014-16-1-2395.

Thank you all,

Nick Molinaro

Table of Contents

Chapter 1: Introduction	1
1.1 Literature Review	2
1.1.1 The Physics of the Plane Wake	2
1.1.2 Universality and Self-Preservation.....	3
1.1.3 The Two Point Time Delay Correlation, Proper Orthogonal Decomposition and Characteristic Eddy Structures	6
1.2 Description of the NACA 0012 Wake Measurements.....	7
1.3. Description of the Two-Point Correlation and Proper Orthogonal Decomposition Analysis Methods	9
1.3.1 The Two Point Time Delay Correlation	9
1.3.2 Proper Orthogonal Decomposition.....	9
1.4 Literature Review Conclusion.....	11
Chapter 2: Experimental Setups	12
2.1 Virginia Tech Stability Wind Tunnel Test Entry	12
2.1.1 Stability Wind Tunnel Reference Measurement Systems	13
2.1.2 Test Model Setup	14
2.1.3 Coordinate System	15
2.1.4 Test Matrix.....	16
2.1.5 Stability Wind Tunnel Traverse and Measurement Techniques.....	16
2.2 Open Circuit Wind Tunnel Test Entry.....	17
2.2.1 The Virginia Tech Open Circuit Wind Tunnel	18
2.2.2 Reference Measurement Systems	20
2.2.3 Test Model Setup	22
2.2.4 Coordinate System	22
2.2.5 Test Matrix.....	23
2.2.6 Open Circuit Wind Tunnel Traverse System.....	24
2.2.7 Flow Characterization Measurements	25
2.3 Hotwire Anemometry	27
2.3.1 Hotwire Probes.....	27
2.3.2 Constant Temperature Anemometry	27
2.3.3 Velocity and Angle Calibration	28
2.3.4 Quad-Hotwire Measurement Uncertainty.....	29

Chapter 3: Results	31
3.1. Stability Wind Tunnel Measurements	31
3.1.1. Measurement Summary	31
3.1.2. Wake Profiles	31
3.2 Open Circuit Wind Tunnel Measurements	37
3.2.1 Documenting the Two-Dimensionality of the Cylinder Wake	38
3.2.2 Comparing the Stability Wind Tunnel and Open Circuit Wind Tunnel Wakes	40
3.2.3 Description of the Two Point Time Delay Correlation	41
3.2.4 Quad-wire Two-Point Grids	42
3.2.5 Measurement Consolidation and Symmetry in the Two-Point Correlation	44
3.2.6 Initial Two-Point Measurement Results	46
3.2.7 Shifting the Measurement Grid Data.....	47
3.2.8 Correction for the Angle Sensitivity of the Hotwire Probes.....	49
3.2.9 Hotwire Probe Coherence.....	53
3.2.10 The Cylinder Wake Two-Point Correlation.....	55
3.2.11 Cylinder Wake Proper Orthogonal Decomposition	59
3.2.12 Cylinder Wake Compact Eddy Structure	64
3.3 Comparison with Airfoil Wake Data	65
3.3.1 Comparison of Normalized Single Point Profiles	65
3.3.2 Zero Separation Time Delay Correlation Coefficients in the Wake Center.....	70
3.3.3 Cylinder and Airfoil Wake Two Point Zero Time Delay Correlation Comparison for $y/L_w = 1$	71
3.3.4 Modal Velocity Profile Comparisons.....	77
3.3.5 Compact Eddy Structure Comparison.....	79
3.4 Discussion	82
Chapter 4: Conclusions	83
References	85
Appendix A: Accessing the Two-Point Correlation Function.....	88
Appendix B: Transformation of the Open Circuit Wind Tunnel Reynolds Stress Profiles	90
Appendix C: Complete Set of Cylinder and Airfoil Two-Point Correlation Comparisons	95
C.1 Zero Time Delay Correlation Comparison for an Anchor Point of $y/L_w = 0$	95
C.2 Zero Time Delay Correlation Comparison for an Anchor Point of $y/L_w = 0.5$	99
C.3 Zero Time Delay Correlation Comparison for an Anchor Point of $y/L_w = 1$	102

C.4 Zero Time Delay Correlation Comparison for an Anchor Point of $y/L_w = 1.5$ 102
C.5 Zero Time Delay Correlation Comparison for an Anchor Point of $y/L_w = 2$ 105
C.6 Zero Time Delay Correlation Comparison for an Anchor Point of $y/L_w = 2.5$ 108

List of Tables

Table 3.1. The absolute uncertainty in the single point statistics.....	30
Table 3.2. The absolute uncertainties in the two point statistics.....	30

List of Figures

Figure 1.1. Definition of the wake scaling variables.	4
Figure 2.1 Layout of the Stability Wind Tunnel. (Illustration credit: William J. Devenport).....	12
Figure 2.2 The Stability Wind Tunnel test section in the anechoic configuration. (Illustration credit: William J. Devenport).....	13
Figure 2.3. Mounting setup of the cylinder model.....	15
Figure 2.4. Cylinder end plate dimensions and mounting system.	15
Figure 2.5 The cylinder mounted in the test section with the coordinate system defined.....	16
Figure 2.6 Stability Tunnel three-dimensional traverse mounted downstream of the cylinder.	17
Figure 2. 7. Schematic of the open circuit wind tunnel. Not drawn to scale.	18
Figure 2.8. The closed test section.	19
Figure 2.9 View looking upstream into the closed test section.....	19
Figure 2.10. The pressure tap locations in to closed section of the Open Circuit Wind Tunnel.....	21
Figure 2.11. The Pitot static probe mounted inside the test section.....	21
Figure 2.12. Boundary layer measurement setup (left) and the dimensions of the opening of the flattened Pitot probe in millimeters (right).	21
Figure 2.13. Flow fences tested in the open circuit test.	22
Figure 2.14 View looking upstream showing the cylinder mounted 13 inches downstream of the inlet.	23
Figure 2.15 The fixed and moving probe traverses mounted to the Open Circuit Wind Tunnel test section (left) and the moving probe directions.....	24
Figure 2.16. Empty test section velocity contour.	26
Figure 2.17. Boundary layer profile measured in the center of the test section.....	26
Figure 2.18. Wake cross section measured without cylinder end plates.....	26
Figure 2. 19. Wake cross section measured with cylinder end plates.....	26
Figure 2.20 Close up of quad hotwire probes.....	27
Figure 2.21 Description of the quad wire geometry described by Wittmer <i>et al.</i> (1998).....	27
Figure 3.1 Stagnation pressure coefficient wake cross section without the fences installed.....	32
Figure 3.2. Stagnation pressure coefficient wake cross section with the fences installed.....	32
Figure 3.3. Stagnation pressure coefficient profiles from the wake survey.....	32
Figure 3.4 Mean velocity profiles measured in the Stability Wind Tunnel.....	33
Figure 3.5. Normal Reynolds stress profiles measured in the SWT wake.	33
Figure 3.6. Cross Reynolds stress profiles measured in the SWT wake.	33
Figure 3.7. The variation in the half wake width (left) and the deficit velocity (right).....	34
Figure 3.8. Evolution in the mean u velocity of the SWT wake.	35
Figure 3.9. Evolution in the $\overline{u^2}$ Reynolds stress profile.....	35
Figure 3.10. Evolution in the $\overline{v^2}$ Reynolds stress profile.....	35
Figure 3.11. Evolution in the $\overline{w^2}$ Reynolds stress profile.	36
Figure 3.12. Evolution in the \overline{uv} Reynolds stress profile.....	36
Figure 3.13. Evolution in the \overline{vw} Reynolds stress profile.....	36
Figure 3.14. Evolution in the \overline{uw} Reynolds stress profile.....	36
Figure 3.15. Evolution in the G_{uu} autospectral density.....	37
Figure 3.16. Evolution in the G_{vv} autospectral density.	37
Figure 3.17. Evolution in the G_{ww} autospectral density.....	37

Figure 3.18. A wake cross section 20D downstream of the cylinder center.....	39
Figure 3.19. Comparison of pressure profiles from the cylinder wake cross section measurement.....	39
Figure 3.20. Mean flow comparison of the cylinder wakes measured in each facility.	40
Figure 3.21. $\overline{u^2}$ stress comparisons	41
Figure 3.22. $\overline{v^2}$ stress comparisons	41
Figure 3.23. $\overline{w^2}$ stress comparisons.....	41
Figure 3.24. \overline{uv} stress comparisons.....	41
Figure 3.25. R_{22} and R_{23} two-point correlation data in the airfoil wake measured by Devenport <i>et al.</i> (2001).....	44
Figure 3.26. The positive fixed probe grid.....	45
Figure 3.27. The negative fixed probe grid.....	45
Figure 3.28. The consolidated grid.....	45
Figure 3.29. Extracted CJWT $\overline{u^2}$ wake profiles.	46
Figure 3.30. Extracted CJWT $\overline{v^2}$ wake profiles.	46
Figure 3.31. Extracted CJWT $\overline{w^2}$ wake profiles	47
Figure 3.32. Extracted CJWT \overline{uv} wake profiles.....	47
Figure 3.33. Shifted CJWT $\overline{u^2}$ wake profiles.....	48
Figure 3.34. Extracted CJWT $\overline{v^2}$ wake profiles.	48
Figure 3.35. Extracted CJWT $\overline{w^2}$ wake profiles.	48
Figure 3.36. Extracted CJWT \overline{uv} wake profiles.....	48
Figure 3.37. Grid 2 RMS voltages.....	48
Figure 3.38. Grid 19 RMS voltages.....	49
Figure 3.39. The error in the quad-hotwire measured v velocity.	50
Figure 3.40. Transformed $\overline{u^2}$ Reynolds stress.....	51
Figure 3.41. Transformed $\overline{v^2}$ Reynolds stress profiles	51
Figure 3.42. Transformed $\overline{w^2}$ Reynolds stress profiles.....	52
Figure 3.43. Transformed \overline{uv} , \overline{vw} and \overline{uw} Reynolds stress	52
Figure 3.44. Transformed $\overline{u^2}$ Reynolds stress profile comparison.	52
Figure 3.45. Transformed $\overline{v^2}$ Reynolds stress profile comparison.	52
Figure 3.46. Transformed $\overline{w^2}$ Reynolds stress profile comparison.	52
Figure 3.47. Transformed \overline{uv} Reynolds stress profile comparison.....	52
Figure 3.48. Fixed and moving probe locations.	53
Figure 3.49. Fixed and moving probe autospectra at the probe locations shown in Figure 3.48.....	53
Figure 3.50. Coherence spectra at the probe locations shown in Figure 3.48	54
Figure 3.51. Fixed and moving probe locations.....	54
Figure 3.52. Fixed and moving probe autospectra at the probe locations shown in Figure 3.51.....	54
Figure 3.53. Coherence spectra at the probe locations shown in Figure 3.51.....	54
Figure 3.54. Cylinder wake correlation for a fixed probe location of $y/L_w = 1$	57
Figure 3.55. Cylinder wake correlation for a fixed probe location of $y/L_w = 1$	58
Figure 3.56. Correlation figures for the R_{23} correlation component for a fixed probe location of $y/L_w = 1$ (left) and $y/L_w = -1$ (right).....	58
Figure 3.57. Modal profiles and relative energy for the first twenty modes in the streamwise (a)(d), wake normal (b)(e) and spanwise (c)(f) directions.....	60
Figure 3.58. Modal velocity profiles for the first mode.	60
Figure 3.59. Modal velocity profiles for the second mode.....	61
Figure 3.60. Modal velocity profiles for the third mode.	61
Figure 3.61. Modal velocity profiles for the fourth mode.....	61
Figure 3.62. Zero separation correlation at zero time delay.	63
Figure 3.63. Cumulative eigenvalue spectrum for the first 20 modes in the wake normal direction.	63
Figure 3.64. Modal profiles for the first six modes in the cylinder wake. Figures (a)-(f) correspond to modes 1-6 respectively.....	64

Figure 3.65. Compact eddy structure for the first mode.	65
Figure 3.66. Compact eddy structure for the second mode.	65
Figure 3.67. Compact eddy structure for the third mode.	65
Figure 3.68. Compact eddy structure for the fourth mode.	65
Figure 3.69. Comparison of the mean flow velocity.	67
Figure 3.70. Comparison of the $\overline{u^2}$ Reynolds stress profiles between the cylinder and airfoil wakes.	68
Figure 3.71. Comparison of the $\overline{v^2}$ Reynolds stress profiles between the cylinder and airfoil wakes.	68
Figure 3.72. Comparison of the $\overline{w^2}$ Reynolds stress profiles between the cylinder and airfoil wakes.	69
Figure 3.73. Comparison of the \overline{uv} stress profiles between the cylinder and airfoil wakes.	69
Figure 3.74. Comparison between the $\overline{u^2}$ stress profiles for different wakes from literature.	70
Figure 3.75. Time delay correlation coefficient in the cylinder wake.	71
Figure 3.76. Time delay correlation coefficient in the airfoil wake.	71
Figure 3.77. Comparison between the cylinder (left) and airfoil (right) R_{11} correlations at $y/L_w = 1$	74
Figure 3.78. Comparison between the cylinder (left) and airfoil (right) R_{22} correlations at $y/L_w = 1$	74
Figure 3.79. Comparison between the cylinder (left) and airfoil (right) R_{33} correlations at $y/L_w = 1$	74
Figure 3.80. Comparison between the cylinder (left) and airfoil (right) R_{12} correlations at $y/L_w = 1$	75
Figure 3.81. Comparison between the cylinder (left) and airfoil (right) R_{13} correlations at $y/L_w = 1$	75
Figure 3.82. Comparison between the cylinder (left) and airfoil (right) R_{21} correlations at $y/L_w = 1$	75
Figure 3.83. Comparison between the cylinder (left) and airfoil (right) R_{23} correlations at $y/L_w = 1$	76
Figure 3.84. Comparison between the cylinder (left) and airfoil (right) R_{31} correlations at $y/L_w = 1$	76
Figure 3.85. Comparison between the cylinder (left) and airfoil (right) R_{32} correlations at $y/L_w = 1$	76
Figure 3.86. Modal profiles for the first six modes in the cylinder wake. Figures a-f correspond to modes 1-6 respectively.	78
Figure 3.87. Modal profiles for the first six modes in the airfoil wake. Figures a-f correspond to modes 1-6 respectively.	78
Figure 3.88. Comparison of the eigenvalue spectrum in the cylinder and airfoil wakes.	79
Figure 3.89. Comparison of the zero separation correlations for the cylinder (left) and airfoil (right) wakes.	80
Figure 3.90. Comparison of the eddy structures for the first mode in the cylinder (left) and airfoil (right) wakes. ...	81
Figure 3.91. Comparison of the eddy structures for the second mode in the cylinder (left) and airfoil (right) wakes. ...	81
Figure 3.92. Comparison of the eddy structures for the third mode in the cylinder (left) and airfoil (right) wakes. ...	81
Figure 3.93. Comparison of the eddy structures for the fourth mode in the cylinder (left) and airfoil (right) wakes. ...	82
Figure B.1. Comparison between scaled OCWT and SWT normal Reynolds stress profiles.	90
Figure B.2. Comparison between scaled OCWT and SWT cross stress profiles.	91
Figure B.3. Transformed OCWT normal stress profiles.	91
Figure B.4. Transformed OCWT cross stress profiles.	92
Figure B.5. Comparison between scale OCWT and SWT normal Reynolds stress profiles for the fixed probe.	92
Figure B.6. Comparison between scale OCWT and SWT cross stress profiles for the fixed probe.	93
Figure B.7. Transformed OCWT normal Reynolds stresses for the fixed probe.	93
Figure B.8. Transformed OCWT cross stresses for the fixed probe.	94
Figure C.1. R_{11} correlation comparison between the cylinder (left) and airfoil (right) wakes.	95
Figure C.2. R_{12} correlation comparison between the cylinder (left) and airfoil (right) wakes.	96
Figure C.3. R_{13} correlation comparison between the cylinder (left) and airfoil (right) wakes.	96
Figure C.4. R_{21} correlation comparison between the cylinder (left) and airfoil (right) wakes.	96
Figure C.5. R_{22} correlation comparison between the cylinder (left) and airfoil (right) wakes.	97
Figure C.6. R_{23} correlation comparison between the cylinder (left) and airfoil (right) wakes.	97
Figure C.7. R_{31} correlation comparison between the cylinder (left) and airfoil (right) wakes.	97
Figure C.8. R_{32} correlation comparison between the cylinder (left) and airfoil (right) wakes.	98
Figure C.9. R_{33} correlation comparison between the cylinder (left) and airfoil (right) wakes.	98
Figure C.10. R_{11} correlation comparison between the cylinder (left) and airfoil (right) wakes.	99
Figure C.11. R_{12} correlation comparison between the cylinder (left) and airfoil (right) wakes.	99
Figure C.12. R_{13} correlation comparison between the cylinder (left) and airfoil (right) wakes.	99

Chapter 1: Introduction

This thesis describes an experimental study of the two-point correlation structure of a cylinder wake. Measurements were performed on an untripped cylinder wake at a Reynolds number based on the cylinder diameter and freestream velocity of 60 000. The majority of the measurements were performed in the mid-wake region 20 diameters downstream of the cylinder center. These measurements were made to provide the inflow boundary condition to a larger study, described by Alexander *et al.* (2016), where the sound radiated by an open rotor due to the ingestion of the cylinder wake was studied. The four-dimensional space-time correlation of the wake at the rotor disk location, measured without the rotor installed, provides the complete linear inflow boundary condition to this problem.

A major goal of the larger study is to develop more accurate prediction methods for an open rotor ingesting turbulence. Glegg *et al.* (2015) discusses the methodology for computing the far field sound spectrum generated by a rotor ingesting turbulence. The authors show that to predict the far field sound spectra, the blade loading correlation and upwash velocity correlation function are required. The upwash velocity is the velocity perpendicular to the blades of a rotor disk, and its correlation function directly depends on the two-point time delay correlation function of the inflow. The two-point time delay correlation function is also important in the larger study because it can be used to calculate the dominate eddy structures present in a flow. Identifying coherent structures in the wake flow is of interest to the larger study because the broadband noise generated by a rotor blade can be broken down into predictions of the noise generated by individual characteristic eddies of the flow.

This thesis discusses the structure of the undisturbed cylinder wake in terms of its turbulence statistics and two-point time delay correlation. Detailed comparisons will be made with the fully developed airfoil wake data measured by Devenport *et al.* (2001). The available data includes the results of similar turbulence statistic and two-point correlation measurements to the data measured in the present study. The two-point correlation functions in each wake flow were used to infer the characteristic eddy structures in each wake using proper orthogonal decomposition. The comparisons between the cylinder and airfoil wake data sets show some similarities, but also some significant differences. Most surprisingly, the two wakes were found to have quite similar mean flows while at the same time supporting markedly different turbulence structures. This comparison is significant to the larger study because a cylinder may not always be the best representation of a real world turbulence ingestion scenario. For example, an airfoil wake would be a better inflow condition for an aircraft with rear-mounted control surfaces and a rear mounted propeller. The comparisons between the structures of the cylinder and airfoil turbulent wake flows will give insight into how and why these different inflow conditions will produce different sound fields when an open rotor ingests either one of these wake flows.

1.1 Literature Review

1.1.1 *The Physics of the Plane Wake*

The wake behind a circular has been widely studied for its relative simplicity and inhomogeneity. The plane wake specifically is statistically stationary, two-dimensional and symmetric about the axis aligned with the cylinder's span. That is not to say that completely understanding turbulence is an easy task. Fluid turbulence is a complex subject especially when applied to separated flow, jet noise, boundary layers and ingestion as described by Roshko (1977).

It has been accepted that the flow over a circular cylinder produces periodic vortex shedding known as von Karman vortex streets. Roshko (1954) performed an experimental study designed to characterize the development of the cylinder wake at Reynolds numbers between 40 and 10,000. The cylinder diameters ranged from 0.0235 to 0.635 cm and spanned the width of the 50 cm wind tunnel test section. Hotwire probes were used to measure the velocity fluctuations in the cylinder wake. Roshko (1954) showed that there are three ranges in the cylinder wake: the stable range, transition range and the irregular range. In the stable range, between Reynolds numbers of 40 and 150 the classical stable vortex streets are formed and were observed in the experimental results. In the irregular range between Reynolds numbers of 300 and 10,000 the periodic vortex shedding is observed along with turbulent velocity fluctuations. In the stable range the large free vortices convect downstream and dissipate through viscous diffusion. In the so called irregular range the free vortices contain turbulent fluid and thus diffuse faster. Roshko states that the measured wake became fully turbulent 40 to 50 cylinder diameters downstream.

The work of better understanding the flow behind a cylinder was continued by Gerrard (1966) who aimed to better understand the dimensionality of the wake. He used an array of hotwire probes distributed along a cylinder's length designed to measure the three dimensional structure of the wake flow of the near wake where $x/d \leq 10$. Measurements were made at a Reynolds number based on cylinder diameter of 3900. Gerrard presented Reynolds stress profiles and autospectra and ultimately concluded that the very near wake is two-dimensional. The experiments also showed that for larger streamwise separations three-dimensional effects result from the occurrence of laminar and turbulent vortices at the same time at different positions along the cylinder span. This shows that the three-dimensional flow around a two dimensional body is complicated where two-dimensional flow only exists in the very near wake.

Understanding the turbulent structures present in wake flows was continued by the work of Townsend (1979). Townsend performed measurements at a cylinder diameter Reynolds number of 8000 and at a streamwise station 170 diameters downstream of the cylinder. He studied the coherent organized eddy structures in turbulent shear flows by recording velocity fluctuations in the flow. He found that the eddy life cycle from generation to decay makes it difficult to determine a single eddy structure using eigenfunction analysis since the characteristic eddy will be assumed combination of eddies at different stages in its life cycle. To obtain a better description of the wake eddies one half of the wake must be sampled such that the eddy structures can be computed over this range.

Wake flows have also been studied in more recent times. The structure of the near field wake was further investigated in a PIV study performed by Braza *et al.* (2006). The goal of this study was to measure the structure of the wake to use for simulation validation. A 1.4 cm cylinder was placed in a wind tunnel test section 670 mm x 670 mm. The aspect ratio of the cylinder in this study was 4.8. PIV measurements taken between 0.5 and 2.5 diameters downstream at a Reynolds number based on cylinder diameter and freestream velocity of 140 000. The measurements reveal a symmetric pattern in u velocity and an antisymmetric pattern in v velocity due to the averaging of alternating eddies. This caused a similar asymmetry in the Reynolds shear stress as shown by Agelinchaab *et al.* (2009) who studied the wake of circular and square cylinders at streamwise locations of 1.25, 2.5 and 5 diameters in a water tunnel at a Reynolds number based on side length and upstream velocity of 5 715. In both studies The streamlines show a strong recirculation region directly downstream of the cylinder. The full Reynolds stress tensor was computed in each study and yielded similar results. Agelinchaab *et al.* (2009) also investigated the two-point correlation using the streamwise and transverse velocity components. The study showed that as the correlation center moves downstream the size of the correlation structure becomes wider. The correlation in the transverse direction is stretched perpendicular to the wake as the center moves downstream.

Recent studies have been performed where understanding the wake flow in detail is necessary for understanding the noise produced by a wake generator. Noise reduction has become increasingly important in the design of new and existing commercial and military flight vehicles. It is important to study how this noise is generated from two dimensional bodies such as cylinder so that it can be reduced. Matsuzaki *et al.* (2004) investigated the sound pressure level (SPL) changes with respect to aspect ratio and inclined angle of a circular cylinder. The work attributed the change in SPL to changes in the vortex structure of the wake. Hotwire measurements were performed in a low noise wind tunnel 1.25 diameters downstream for cylinder diameter Reynolds numbers between 300 and 20,000. The wake study concluded that the influence on the spanwise structure in the wake becomes greater as the aspect ratio decreases and the inclined angle increases. They also found that as the inclination angle increases the spanwise wake structures are highly influenced by the bottom wall. The von Karman vortex street becomes stronger in the direction of the cylinder axis as the inclination angle increases, Matsuzaki *et al.* (2004). As the inclination increases the vortex street structure begins to break down. These flow structure observations were made using the hydrogen bubble flow visualization technique in a closed circuit water tunnel at a cylinder diameter Reynolds number of 450. Understanding this mechanism is important so that appendages can be designed to have a quieter acoustic profile.

1.1.2 Universality and Self-Preservation

A common theme in the literature is the hypothesis that at some location downstream of a wake generator the turbulence profiles will be similar regardless of the generator. Many authors have investigated wake flows shed from different generators and evaluated whether wakes shed by different generators can be considered universal. The earliest ideas of self-preservation are those of Townsend *et al.* (1947, 1949). Townsend hypothesized that sufficiently far downstream of the wake generator the wake reaches a state where it can be described by a single velocity scale, the deficit velocity given by U_w , and a single length scale, the half wake width given by L_w . The deficit velocity is defined by the difference between the freestream and the minimum velocity on the wake

centerline. The half wake width is defined as the distance between the wake centerline and the location of half the deficit velocity. These variables have been used by many authors to scale wakes generated from different bodies to assess the universality of wake flows. Figure 1.1 shows the self-preserving plane wake and highlights the half wake width and deficit velocity. This description of the wake and its scaling variables is described by Wygnanski *et al.* (1986).

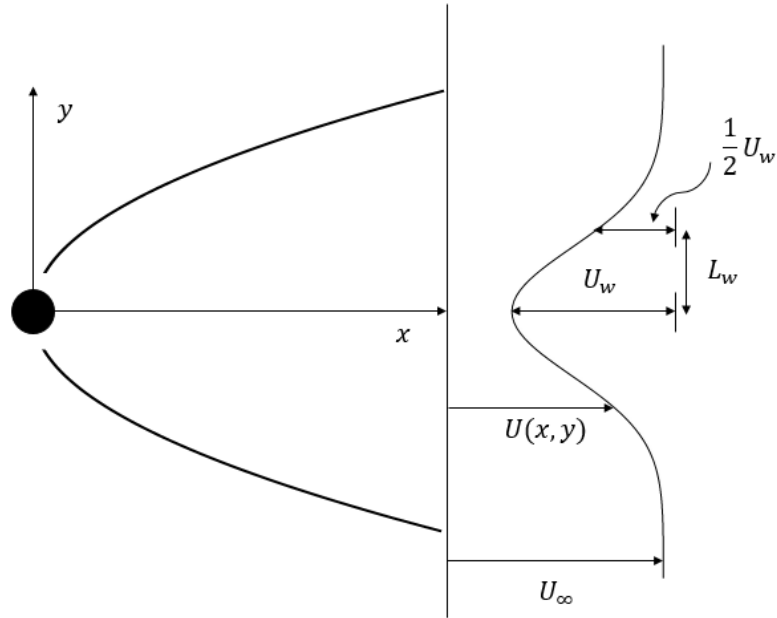


Figure 1.1. Definition of the wake scaling variables.

Self-preservation or self-similarity implies that the mean velocity and Reynolds stress profiles are independent of the streamwise location when normalized on U_w and L_w . Wygnanski *et al.* (1986) measured the wakes behind an airfoil, a cylinder, a solid strip and a 70% solid screen. The solid strip and screen were specially designed to have wakes with the same momentum thickness as the cylinder at a cylinder diameter Reynolds number of 4 000. Reynolds numbers ranged from 1 360 to 6 500 for each model tested. Wygnanski *et al.* (1986) found that the velocity and length scales, U_w and L_w respectively, were indeed dependent on the wake generator. The geometry of the generator had a significant effect on the scales when normalized on the momentum thickness and the free-stream velocity of each flow. This implies that no universal behavior was observed in these quantities determine in the wake flows of different generators. Although L_w and U_w were not similar for different generators, the mean velocity profiles normalized on the deficit velocity and the half wake width were nearly identical for each generator. Wygnanski *et al.* (1986) also found that the turbulence intensities in each wake were nearly self-preserving sufficiently downstream of the generator. Although the Reynolds stresses were nearly self-similar for each individual generator, the stress profiles measured behind different generators showed significant variation in magnitude. The wake growth rates behind each generator also varied significantly. For example, the airfoil wake had a larger growth in the same normalized streamwise distance than the growth rate seen in the flows behind the solid strip and turbulence screen, although each wake was

individually self-preserving. This further suggests that turbulence is not completely universal. George (1989) confirmed and further argued that there are no simple conclusions for the self-preservation of turbulent wakes. George acknowledges that wake flows reach a preserving state downstream of a wake generator and that some believe that all plane wakes should evolve independently of their generators. George reviewed two decades of experimental work to reach the conclusion in some cases a wake can become self-preserving and independent of the generator while in some cases the wake structure is strongly dependent on generator.

Direct numerical simulations of three different plane wakes performed by Moser *et al.* (1998) further confirmed the findings from the study performed by Wygnanski *et al.* (1986). The wakes were simulated using two realizations of a turbulent boundary layer each at a momentum thickness Reynolds number of 670. The two boundary layers were used to produce a simulation for a zero thickness flat plate at zero angle of attack. To account for the two-dimensional disturbances in a plane wake such as the von Karman vortex street, forcing was added to the simulations. Two wakes each with excitation (strong and weak) and one unforced wake were studied. The forcing was applied to the flows by amplifying the two-dimensional modes in the initial condition in the streamwise and wake-normal velocity components. This resulted in an uncontrolled disturbance that did not have a characteristic streamwise wavelength (Moser *et al.* 1998). In the case of the weakly forced wake the fluctuations were amplified by a factor of 5 while in the strongly forced wake the fluctuations were amplified by a factor of 20. Moser ultimately concluded that the mean streamwise velocity profiles of three wake flows were similar when normalized on the deficit velocity and half wake width. The Reynolds stress profiles normalized on these variables did not show any agreement and thus were not universal. Moser showed that there was better agreement when the stress profiles were normalized on wake growth rate in addition to the deficit velocity. This suggests that the half wake and deficit velocity cannot be used to solely assess the preservation of wakes shed by different generators, since the growth rates of different wakes can be significantly different.

More recently Tang *et al.* (2016) also investigated only self-preservation in the wake of a circular cylinder at a cylinder diameter and freestream velocity Reynolds number of 2000. Measurements were performed at streamwise stations between 20 and 601 diameters. The study showed as previous have before it that the mean velocity deficit and Reynolds stress do indeed exhibit self-similar behavior for a single geometry and some location downstream of the generator. The energy spectra were also self-preserving when normalized on the half wake and deficit velocity. The authors state the effect of initial conditions such as the geometry of the generator cannot be ruled out as they have only considered the wake from one generator. This agrees with the authors work presented here. George (2012) revisits the idea of universality of wakes flow and came to the same conclusion as his previous work discussed in George (1989). George again ended his review by stating that the upstream generator conditions indeed do matter, where in some flows the geometry has a greater influence on the wake structure than in others.

1.1.3 The Two Point Time Delay Correlation, Proper Orthogonal Decomposition and Characteristic Eddy Structures

Turbulent fluid flow is an important subject in the aerodynamic and aeroacoustic fields and is still perhaps one of the least understood. It seems that since the physical laws of fluid flows are well understood and described by the Navier-Stokes equations and that over a century of complex experiments have been performed and discussed, this flow should be well defined in the analytical and computational sense. However it is still difficult to model turbulent flow for even simple geometries at high Reynolds numbers as described by Berkooz *et al.* (1993) due to the nonlinearity of the governing equations. Another complication is that the experimental and mathematical data show that turbulence involves the interaction of many degrees of freedom over a wide range of temporal and spatial scales as described by Berkooz *et al.* (1993). One approach is to reduce the complexity of the flow by removing the nonessential degrees of freedom. According to Berkooz *et al.* (1993), Liu (1986) was among the first to suggest that this reduction of complexity was possible and document the experimental discovery of coherent structures. Lumley (1989) reviewed an extensive amount of experimental studies investigating coherent structures, which lead to the definition given by Berkooz *et al.* (1993). Coherent structures are organized spatial features that repeatedly appear and have a characteristic temporal life cycle. The existence of these large structures directly contrast the idea that turbulence is a completely random phenomenon.

Proper Orthogonal Decomposition (POD) is a method used to extract turbulent structures from turbulent flow measurements. The proper orthogonal decomposition is a mathematical method of extracting basis functions for a modal decomposition of a set of signals. The mathematical basis is described by Loeve *et al.* (1955) and Berkooz *et al.* (1993). POD was used in turbulence by Lumley (1967) where second order statistics were used to extract large scale structures from turbulent flow. The velocity fluctuation components are used to compute the second order statistics, or the two-point time delay correlation, needed to perform a POD analysis. This two-point correlation can be computed by correlating the velocity components between two velocity probes, or using laser diagnostic methods. POD is a popular method especially in the application of turbulence since it is a purely mathematical procedure. The POD method does not need assumptions of linearity in order to compute the modes that describe the turbulent structures. The method is as blind and as general as Fourier analysis (Berkooz *et al.* 1993). POD works by describing turbulence in terms of a set of orthogonal modes by maximizing the energy of the modes where the eigenvalues correspond to the kinetic energy of the modes (Stanislav, 2006). There have been many experimental studies performed with the intention of using POD to characterize the turbulent structures. Kline *et al.* (1967) and Cantwell (1981) were among the first to apply POD techniques to boundary layer flows. Kirby *et al.* (1990) and Glauser *et al.* (1987) applied POD methods to investigate jet flows and Payne and Lumley (1967) used POD to investigate the large eddy structures in wake flows.

Proper orthogonal decomposition has been a useful tool for identifying the shape of eddy structures more recently in different turbulent flows. Wang *et al.* (2014) used PIV to measure a square cylinder wake 1, 3.5 and 6 diameters downstream of the cylinder. The data was used to compute the two-point correlation and ultimately the POD modes at each streamwise location at a Reynolds number of 9,300. They found that more than half of the TKE was in the first POD mode which

represents the vortex shedding. The near wake is dominated by the first two modes, which shows alternately arranged vortices organized in a coherent street. They found that a flow structure could be described qualitatively and quantitatively using POD coefficients. Neumann *et al.* (2009) showed that a novel LDV system could also be used to compute the two-point correlation in a wake at a cylinder diameter Reynolds number of 1200. Waclawczyk *et al.* (2002) made PIV measurements in the near wall region of a turbulent channel flow at a Reynolds number based on channel half width of 6600. Both authors computed two point velocity statistics and performed a POD to gain insight into the eddy structures present in the flow. Two point correlation functions are also relevant to numerical simulations. Johansson *et al.* (2004) created a system that used the full two-point correlation function of a channel flow for a given aspect ratio and Reynolds number to generate inlet turbulence models for channels of different aspect ratio and Reynolds numbers. The generated turbulence models were used as the boundary conditions for DNS and LES methods.

The aeroacoustics field can also make use of proper orthogonal decomposition. POD is especially useful when predicting the sound produced by a turbulent flow interacting with rigid surfaces, such as in the present study. Glegg *et al.* (2000) used compact eddy structures, defined as the projection of the POD modes onto the correlation function, to describe the sound radiated from a fan rotor. This approach eliminates the need for turbulence modeling by assuming a form of the turbulence spectrum. The modes were computed using the cross correlation function estimated from the Reynolds stresses and the wake width. Glegg *et al.* (2001) found that proper orthogonal modes are a better approach than spectral analysis for inhomogeneous flows. The POD of a time stationary flow can be given in terms compact eddy structures which represents the time averaged flow structure. The sound radiated from a particular interaction can then be related to specific features of the flow, where the dominant eddy structures account for most of the sound produced from the interaction between turbulence and rigid surfaces. Proper orthogonal decomposition is important because it provides a mathematical method to interpret turbulent flows and define structures as described by Glegg *et al.* (2001).

1.2 Description of the NACA 0012 Wake Measurements

As previously stated a primary goal of the present study is to evaluate the similarities and differences in the wake structure shed by a cylinder and a NACA 0012 airfoil. Devenport *et al.* (2001) measured a comprehensive data set in the wake of a NACA 0012 airfoil with a chord of 0.2 meters at zero angle of attack. Measurements were performed in the airfoil wake at a chord and freestream velocity Reynolds number of 330 000. This study has provided the data set that will be used to present the wake structure in the airfoil wake and compare with the structure of the cylinder wake measured by the present study. In this section, the measurement setup and results of the study completed by Devenport *et al.* (2001) are discussed.

The airfoil measurements were performed in the Virginia Tech Low-Speed Wind Tunnel which has a test section cross section of 610 mm by 914 mm. The NACA 0012 model was mounted in the center of the test section and featured a 0.5 glass bead trip. Four sensor hotwire probes were used to resolve three components of velocity in the wake flow. From these velocities the Reynolds stress tensor could be computed. Each sensor of the four sensor probes were operated by a Dantec 56C17/56C01 constant temperature anemometer. The units each had a matched frequency

response of 20 kHz. An Analogic 12 bit HSDAS-12 analog-to-digital converter was used to record the probe outputs.

The probes used in the study completed by Devenport *et al.* (2001) are described in Sections 2.5.1 and 2.5.3 as the hotwire probes and calibration procedures as they were also used in the present study. A two-axis computer controlled traverse was used to position the probes for single and two-point hotwire measurements. Reynolds stress profiles were measured at several streamwise stations between $1.67 \leq x/c \leq 12.07$ to determine the location where the wake became fully developed. The study found that the wake reached its self-preserving state at a location of $x/c = 7.5$. In the case of the two point hotwire measurements, one four-sensor probe was positioned using the two-dimensional traverse while the second probe was mounted to a fixed support. The moving probe was traversed in a grid around the fixed probe for 17 fixed probe positions from $y/L_w = 0$ to 3 where y is the coordinate normal to the wake and L_w is the half wake width. Two point measurements were conducted at $x/c = 8.33$ in the fully developed region of the wake. For each fixed probe position the moving probe was positioned at some 400 points each at a different vertical and horizontal separations. The spacing was varied depending on the position in the wake since at large separation a low correlation is expected. As the separation between probes increased the point spacing became coarser. Positive and negative y separations were measured but only $-z$ separations were measured. The wake was assumed to be symmetric about $z = 0$. The flow was sampled for 50 records at 50 kHz with a record length of 3072 to provide sufficient averaging for the cross spectral matrix between the two probes.

A goal of the study performed by Devenport *et al.* (2001) was to reduce the two-point time delay correlation in a form suitable for distribution and for use in aeroacoustics calculations. The fully reduced two-point correlation function of the wake was used as the input to a proper orthogonal decomposition analysis. The authors investigated the energy spectrum and the modal profiles for the first 41 modes in the airfoil wake. The POD analysis concluded with an estimation of the characteristic eddy structures for the first four orthogonal modes. The first four POD modes showed that the fluctuation in the w velocity was negligible and that the symmetric and anti-symmetric profiles in the u and v velocities were associated with the generation of the Reynolds stresses. Modes 3 and 4 showed the most complex motions in the u and v profiles. The eddy structures, or the three dimensional modes, for the first four modes were also presented at $z = 0$, or the mid-span of the airfoil model. The modes showed that eddies appeared singularly and in symmetric pairs in the wake flow. Modes 1 and 3 showed single eddies while modes 2 and 4 showed eddies appear in pairs. The results of this study will be presented and discussed in Section 3.3 when they are compared with the analogous cylinder wake measurement results from the present study.

1.3. Description of the Two-Point Correlation and Proper Orthogonal Decomposition Analysis Methods

1.3.1 The Two Point Time Delay Correlation

The two-point correlation is the basis for the wake structure analysis that will be presented in later sections. The two-point time delay cross correlation function is a correlation between velocities at any two points in a flow. In general terms the two-point time delay correlation is defined in terms of the velocity fluctuations u_i and u_j and the positions at i and j by Wygnanski *et al.* (1986) and Berkooz *et al.* (1993). The two-point correlation is expressed as a function of time and position in Equation 1.1 as,

$$R_{ij}(x, r, \tau) = \overline{u_i(x, t)u_j(x + r, t + \tau)} \quad \text{Equation 1.1}$$

In this equation x refers to the first point in the correlation. In this case x has only one dimension. The variable r is the separation between points in the same dimension such that $x + r$ is the location of the second point used in the correlation. The time delay is given by τ such that the time associated with the first point is t and the time associated with the second point at some time delay is $t + \tau$. The cross spectrum computed at the points x and $x + r$ can be determined using the two point correlation, R_{ij} , as shown in Equation 1.2.

$$G_{ij}(x, r, \tau, f) = \frac{1}{2\pi} \int_{-\infty}^{\infty} R_{ij}(x, r, \tau) e^{i2\pi f\tau} d\tau \quad \text{Equation 1.2}$$

1.3.2 Proper Orthogonal Decomposition

Proper orthogonal decomposition is used to determine the optimum velocity profile that describes the average instantaneous shape of the structures in a flow. Lumley (1967) and Berkooz *et al.* (1993) show that these orthogonal modes are equivalent to the eigenfunctions of the two-point correlation tensor. The formulation as defined by Berkooz *et al.* (1993) begins by defining the inner product between two fields as, $(f, g) = \int_{\Omega} f(x)g^*(x)dx$, where Ω is the domain of the flow. The norm of the inner product is also defined as, $\|f\| = (f, f)^{1/2}$. The analysis begins with a set of realizations of the function $u(x)$. The goal of the POD analysis is to find a single function that is most similar to the members $u(x)$ on average (Berkooz *et al.*, 1993). The mathematical definition of seeking the most similar function is defined as seeking a function ϕ such that ψ is maximized is shown in Equation 1.3.

$$\max_{\psi} \frac{\overline{|u, \psi|^2}}{(\psi, \psi)} = \frac{\overline{|u, \phi|^2}}{(\phi, \phi)} \quad \text{Equation 1.3}$$

This formulation aims to find the function ϕ in the set ψ which maximizes the inner product with the field u . A necessary condition for Equation 1.3 to hold is that ϕ is an eigenfunction of the two-point correlation tensor shown by Equation 1.4.

$$\int_{\Omega} \overline{u(x)u^*(x')} \phi(x') dx' = \lambda \phi_k(y) \quad \text{Equation 1.4}$$

The two-point correlation is defined as, $R(x, x') = \overline{u(x)u^*(x')}$. There are multiple eigenfunction solutions of Equation 1.4 defined by ϕ_k and λ .

In the present study and in the study performed by Devenport *et al.* (2001) the two-point correlation function was a four-dimensional function. Although the turbulent flow that is two-dimensional on time average, the time delay correlation between every point and every other point in a given cross section is a four-dimensional function. In the case of the plane wake where y is the wake-normal component, and of a four dimensional correlation the POD formulation given above by Equation 1.4 differs slightly. In the case of the four-dimensional time delay correlation there are three spatial dimensions y, y' and Δz and the time delay, τ . The variables y and y' describe the positions of the two points used in the correlation in the same dimension while Δz is the separation between probes in a second direction. A detailed description of the formulation of the two-point correlation in the plane wake at it applies to the present study is included in Section 3.2.3. The two-point correlation in this form can be used in a one dimensional POD on analysis is performed by solving Equation 1.5.

$$\int R_{ij}(y, y', \Delta z, \tau) \phi_j(y') dy' = \lambda \phi_i(y) \quad \text{Equation 1.5}$$

The integral equation given by Equation 1.5 has multiple eigenfunction solutions, $\phi_i^{(n)}(y)$ which represent orthogonal modes of the instantaneous velocity profiles of the wake for the n^{th} mode. The eigenvalues, $\lambda^{(n)}$, represent the turbulent kinetic energy produced by the n^{th} mode.

One problem with POD is that in the homogeneous directions, x and z in the plane wake, it reduces to Fourier decomposition. In this case the modal velocity profiles are represented as sinusoids, which are not good representation of eddies. Devenport *et al.* (2001) used Linear Stochastic Estimation to linearly estimate the velocities in the homogeneous directions. LSE gives the best linear estimate of the velocity field given the velocity component at some point, $u_i(y)$. The velocity field is estimated using the velocity at one point and the two-point correlation tensor as shown in Equation 1.6.

$$u_j^{LSE}(y', z', \tau) \Big|_{LSE} = R_{ij}(y, y', \Delta z, \tau) \frac{u_i(y)}{u_i(y)^2} \quad \text{Equation 1.6}$$

Using the combined modes in the homogeneous computed using LSE and in the inhomogeneous direction using POD, the three dimensional velocity field associated with each mode can be obtained by projecting the mode onto the two-point correlation function shown in Equation 1.7.

$$u_j^{(n)}(y', \Delta z, \tau) \Big|_{CES} = \frac{1}{\lambda^{(n)}} \int \phi_i^{(n)}(y) R_{ij}(y, y', \Delta z, \tau) dy \quad \text{Equation 1.7}$$

The resulting three-dimensional modes are termed compact eddy structures (CES) by Devenport *et al.* (2001) and are obtained by computing the inner product between the correlation function and the proper orthogonal mode. The compact eddy structures do not necessarily occur in the turbulent flow, but they do represent the average instantaneous velocity field of the flow. This processing technique of using POD and CES to extract information about the instantaneous structure of the velocity field provides a mathematically rigorous method for evaluating coherent structures in a

flow. This is useful since it is difficult to make conclusions on the structure of the eddies in a flow solely based on the two-point correlation and turbulence stresses.

1.4 Literature Review Conclusion

This literature review has presented work focused on developing an understanding the of the structures and flow phenomena in wake flows, the concept of self-preservation in wake flows and how the two-point correlation function can be used to compute the average instantaneous modal velocity profiles of a flow using proper orthogonal decomposition.

The first section of this review serves as the background for the work completed by the present study. The work by other authors included in this section each discusses the overall flow structure of the plane wake. Self-preservation and non-universality is of particular importance to the present study. A primary goal of the present study is to assess the similarities and differences in the turbulence and two-point correlation between the cylinder and airfoil wakes. The turbulence statistics and correlations will both be normalized on the half wake width and the deficit velocity so that profiles and two-point correlation measured in the cylinder and airfoil wakes can be quantitatively compared. The idea that the plane wake is self-preserving and evolves independently of the wake generator will also be assessed. The relevance of the similarities or differences to the larger study will be discussed. POD is an important analysis tool that will be used to evaluate the differences between the cylinder and airfoil wake flows. Over the past few decades many authors have used POD to extract the modal velocity profiles from the two-point correlation to gain insight into the coherent structures present in a turbulent flow. The POD analysis will be applied to the cylinder and airfoil wake flows to begin to assess the differences in the eddy structures of each flow. The projection of the proper orthogonal modes onto the correlation function, called the compact eddy structure, is an analytical way to determine the instantaneous velocity field in a turbulent flow. The three-dimensional modes that describe the compact eddy structures in each flow will serve as the ultimate comparison between the cylinder and airfoil wake flows. The eddy structures will allow conclusions to be drawn as to why the two wake flows show similarities and differences in their turbulence profiles and correlation structures.

The following sections in this thesis will discuss the apparatus and instrumentation used in the present study and ultimately the results of the present study. Chapter 2 describes the flow facilities, experimental setups and instrumentation used to measure the cylinder wake's turbulence statistics and the two-point correlation function. The detailed comparisons of the cylinder wake's turbulence statistics, correlation structure and eddy structure with the airfoil wake data are also included in Chapter 3. The wake comparisons between the airfoil and cylinder wake results will give insight on how and why the sound radiated from a rotor ingesting the airfoil or cylinder wake is different.

Chapter 2: Experimental Setups

2.1 Virginia Tech Stability Wind Tunnel Test Entry

The data presented in this thesis was measured in two facilities. The largest and most well-known is the Virginia Tech Stability Wind Tunnel. The facility is a closed-loop subsonic wind tunnel with a maximum flow velocity of 80 m/s in the test section with no blockage. This facility is unique in the fact that it can be used for both aerodynamic and acoustic testing. In its aerodynamic testing configuration, the facility has freestream turbulence intensities of 0.021% and 0.031% at 21 and 57 m/s respectively. These turbulence intensities were measured for flow velocities between 12 and 57 m/s in 2006 by facility personnel. The wind tunnel has two interchangeable test sections to accommodate both types of testing. In its anechoic configuration, the wind tunnel is acoustically quiet without distorting the aerodynamics of the flow. The present study was conducted in this anechoic configuration. The wind tunnel is powered by a 0.45 MW variable speed DC motor. The motor is controlled by a custom Emerson VIP ES-6000 SCR Drive which was designed to limit unsteadiness from the motor. The wind tunnel fan is 4.27 meters in diameter and made up of eight Clark-Y airfoil section blades. The layout of the wind tunnel is shown below in Figure 2.1. The air exchange tower seen in the figure above is used to regulate the temperature in the test section. The tower is located downstream of the fan. After the air exchange tower the flow enters a 5.5-meter square settling chamber which contains 7 turbulence reduction screens. After the settling chamber the flow experiences a 9:1 contraction in the nozzle before entering the test section.

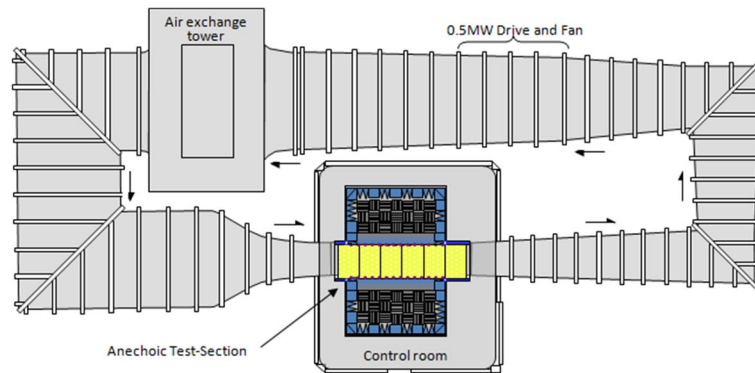


Figure 2.1 Layout of the Stability Wind Tunnel. (Illustration credit: William J. Devenport)

The test section used for acoustic testing has a square cross section of 1.83 meters with a length of 7.3 meters. The floor and ceiling panels consist of perforated aluminum panels covered with Kevlar to limit acoustic reflections and are also backed by foam wedges to help control the facility noise. Along the length of the test section anechoic chambers extend 5.6 meters along both sides. Acoustically transparent Kevlar windows are used to create the test section walls and serve as a flow barrier for the acoustic chambers. These ‘windows’ span 4.2 meters of the test section. The chambers are designed to control the acoustic reflections produced by the wind tunnel facility and test setup. The facility is anechoic down to 180 Hz (Devenport *et al.*, 2013). Figure 2.2 provides a view of the anechoic test section and details the dimensions of the acoustic test section.

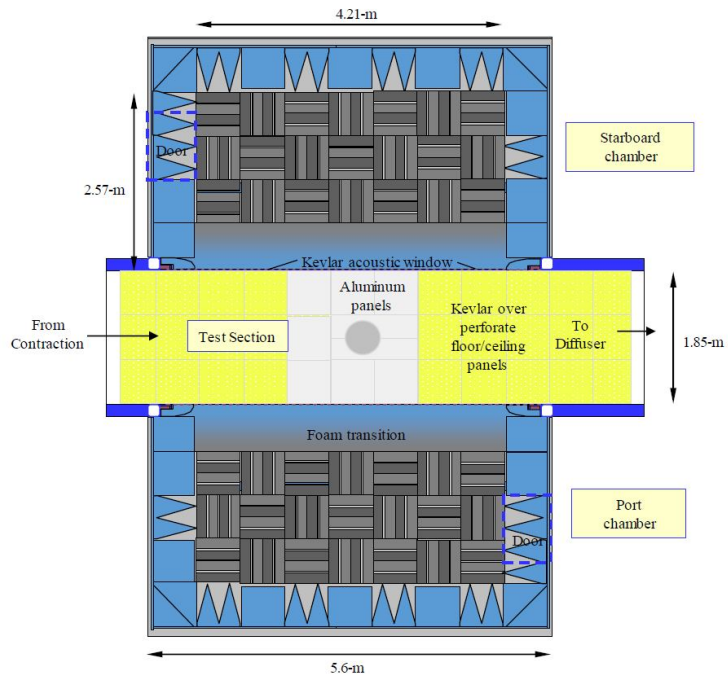


Figure 2.2 The Stability Wind Tunnel test section in the anechoic configuration. (Illustration credit: William J. Devenport)

2.1.1 Stability Wind Tunnel Reference Measurement Systems

In the measurements performed in the Stability Wind Tunnel by the present study the wind tunnel reference conditions were recorded using the facility’s pressure and temperature measurement systems. Two pressure ports in the contraction and two in the settling chamber are used to compute the reference velocity. These pressures were measured using an Esterline 9816/98RK pressure scanner with a rated accuracy of 0.05% and a range of ± 2.5 psi. The flow temperature was measured using an Omega type 44004 Thermistor with an accuracy of $\pm 0.2^\circ C$ located in the wind tunnel contraction. An accurate temperature is crucial for the hotwire calibrations discussed in later sections. The ambient pressure was measured using a Validyne DB-99 Digital Barometer with an accuracy of 0.01 inches of mercury. The reference measurement systems were used to compute the wind tunnel freestream velocity with an uncertainty of 0.5 m/s .

An integral system of the Stability Wind Tunnel in each configuration is the wake rake. This instrument spans the width of the test section, 1.83 meters, and features 126 mixed Pitot and Pitot static probes. The probe tips are located 6.31 meters downstream of the start of the test section. The rake driven by two HT34 – 497 Applied Motion high torque stepper motors controlled by two independent Applied Motion STAC5 controllers. The traverses are operated using an in house Matlab code that sets the rake to a desired height in the test section and samples the pressure probes on the rake using the Esterline scanner. The stagnation pressure coefficient is computed with an uncertainty of 3%, at 20 m/s , using each Pitot probes on the rake to give a wake profile.

2.1.2 Test Model Setup

The model used to generate the wake under investigation in the present study was a circular cylinder with a diameter of 50.8 mm. The cylinder was a machined aluminum tube with an inner diameter of 38.1 mm. The test model was turned on a lathe to produce a smooth, near polished surface finish. The cylinder was mounted in the anechoic test section 1.91 meters from the upstream edge of the test section with an uncertainty of ± 1.6 centimeters. The cylinder was 1.83 meters in span and was designed to span the full height of the test section. The center of the cylinder was positioned in the lateral center of the test section, 0.93 meters from each Kevlar window also with an uncertainty of ± 1.6 centimeters. The cylinder was bolted to half inch thick floor and ceiling panels. An insert was slid into the inner diameter of the hollow center of the cylinder and anchored to a slot cut from the end of the cylinder. The insert was positioned such that it was in contact with the floor or ceiling panel. A 3/8 inch threaded rod through the center of the insert was aligned with a 3/8 inch hole in the panel. The threaded rod was fastened to the panel such that the cylinder model was securely anchored in place and unable to rotate. Figure 2.3 shows a diagram of the mounting system used to install the cylinder model inside the test section with each component labeled.

Pressure taps with a diameter of 0.0625 inches were installed every 15 degrees around the cylinder circumference in a spiral spanning two inches centered around the mid-span of the cylinder. The spiral was inclined at an angle of 51.8 degrees. The pressure taps were used to ensure repeatability between runs and to ensure that there was no influence on the cylinder due to the measurement systems installed in the test section. Flow fences were attached to the cylinder 152.4 mm above and below the floor and ceiling to control the boundary layer interactions with the model at the walls. These positions were determined by inspecting wake-cross section measurements performed with the wake rake in the Stability Wind Tunnel. The end plates needed to be close to the cylinder ends so that they did not influence the wake near center span, but far enough outside of the test section boundary layers. These fences were machined from quarter inch thick aluminum sheet in a hand drawn teardrop shape with a two-inch hole in the center for the cylinder to pass through. The fences were then cut on the center of the cylinder diameter so that they could be easily mounted to the cylinder model when the cylinder was installed inside the test section. Figure 2.4 shows the dimensions of the end plates and the mounting system. In the figure the line where the end plate was split is shown along with the clamshell component that was designed to secure the two end plate halves together and to the cylinder model. The fences are shown installed on the cylinder inside the test section in Figure 2.5.

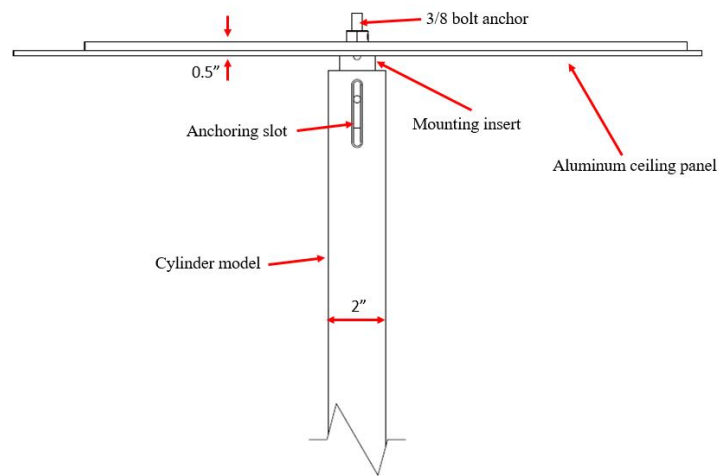


Figure 2.3. Mounting setup of the cylinder model.

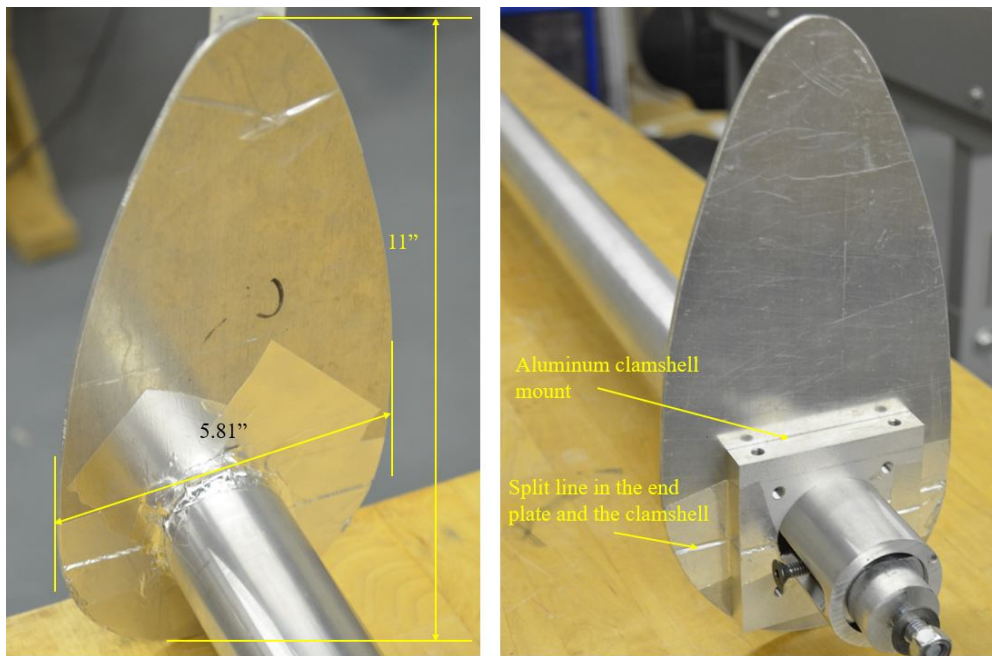


Figure 2.4. Cylinder end plate dimensions and mounting system.

2.1.3 Coordinate System

The origin of the wake coordinate system was located at the midspan of the cylinder's axis. The x axis was positive in the direction of the freestream. The y axis was perpendicular to the wake and was positive pointing towards the starboard side of the test section. The z axis pointed directly upward and was aligned with the cylinder axis. Figure 2.5 shows the cylinder mounted inside the

test section with the coordinate system labeled. The flow fences are also shown in the figure 152 millimeters \pm 0.5 millimeters from the floor and ceiling of the test section.

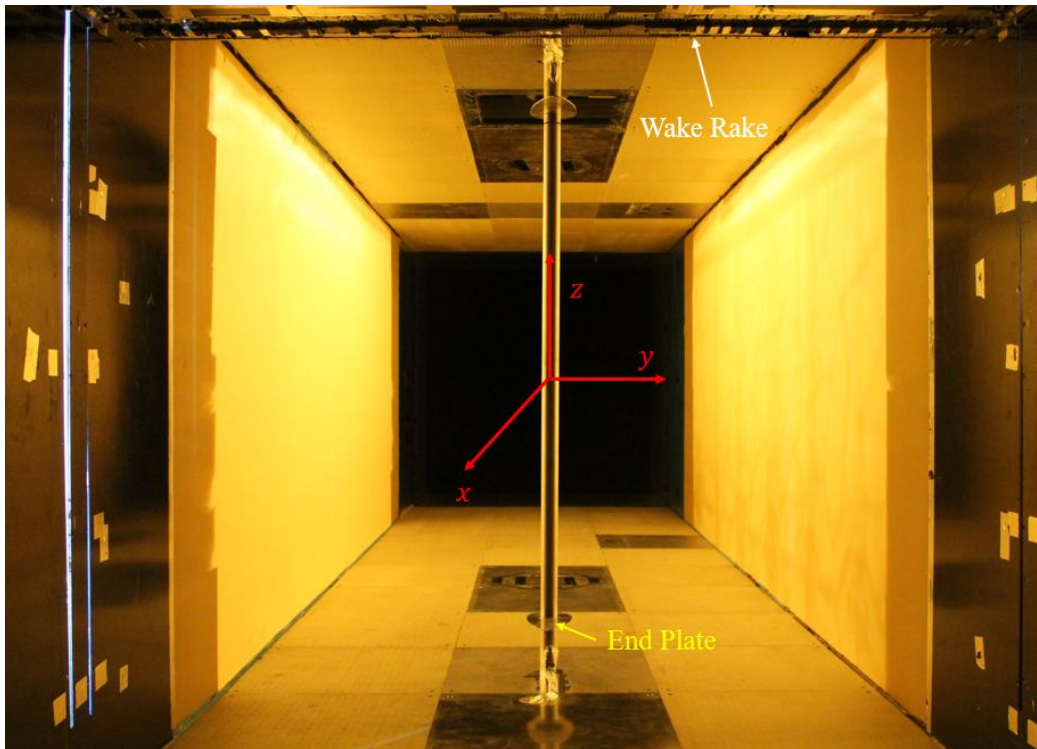


Figure 2.5 The cylinder mounted in the test section with the coordinate system defined

2.1.4 Test Matrix

The measurement goals in the Stability Wind Tunnel test were focused on documenting the wake velocity and turbulence stress profiles. Pressure rake measurements were conducted to assess the two-dimensionality of the cylinder wake before any other measurement was made. Four-sensor hotwire probes were used to measure the Reynolds stress profiles in the cylinder wake at 20, 15 and 10 diameters downstream of the cylinder's center. The streamwise position was set using the computer controlled traverse. The probes were initially aligned 40 inches (20 diameters) downstream of the cylinder center using a metal ruler and was accurate within one sixteenth of an inch. For subsequent profiles measured 15 and 10 diameters downstream of the cylinder center the traverse system was used. The relative streamwise positioning was accurate within one thousandth of an inch. Single hotwire measurements were also performed to validate the four-sensor hotwire measurements. For all wake survey measurements the wind tunnel was operated at a reference velocity of 20 m/s \pm 0.5 meters per second and an actual Reynolds number based on the cylinder diameter of $61\,278 \pm 195$.

2.1.5 Stability Wind Tunnel Traverse and Measurement Techniques

In the Stability Wind Tunnel a computer controlled three-dimensional traverse was used to position the single and quad-hotwire probes in the wake of the cylinder to measure wake profiles. The full

system comprised of seven individual traverse rails. Each rail used an Applied Motor HT34-497 motor to control a screw-rod that moved an aluminum carriage. Figure 2.6 below shows the computer controlled traverse mounted in the anechoic test section with each of the seven rails labeled. Four rails were mounted on the floor and ceiling allowed the hotwire probes to be accurately positioned in the streamwise direction and had about 60 inches of travel. Two vertical rails allowed the probe height inside the test section to be set while a single horizontal rail was used to position the hotwire probes at different locations in the cylinder wake. Each rail was connected to a STAC5 controller with encoder feedback capable of reporting the traverse position within 0.001 inches. A Dewalt DW088K laser level was used to align the hotwire probes directly behind the cylinder center. The traverse system allowed the probes to be precisely positioned 20 diameters downstream of the cylinder and at the midspan of the cylinder. The probes were traversed through the wake and measured 0.228 meters on each side of the cylinder. An in house Matlab code was developed to position the hotwire probes using the three axis traverse system and record the outputs of the hotwire probes. The system allowed for a predetermined set of measurement locations to be defined to automate acquisition code. The traverse was positioned at each desired location then the acquisition system sampled the hotwire signals and stored the data.

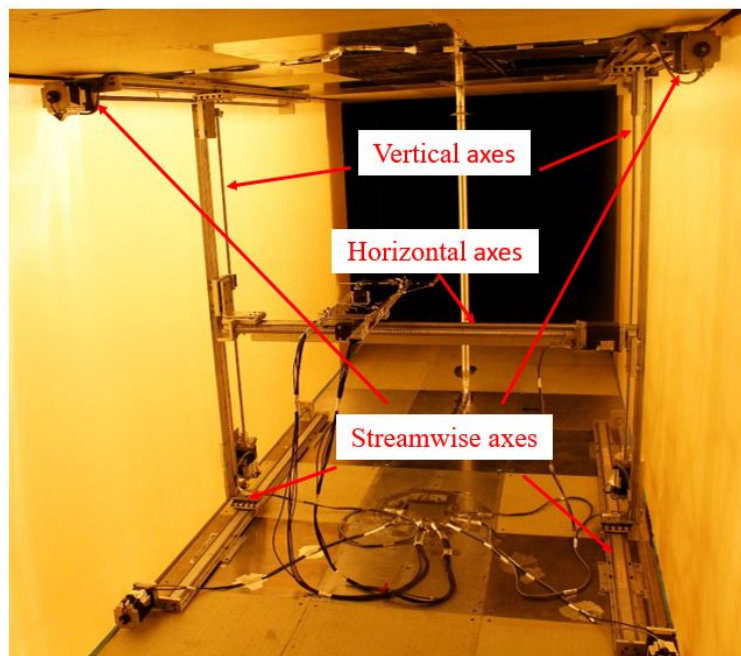


Figure 2.6 Stability Tunnel three-dimensional traverse mounted downstream of the cylinder.

2.2 Open Circuit Wind Tunnel Test Entry

An auxiliary wind tunnel test was used to measure the two-point correlation function of the cylinder wake. This measurement involves measuring the cross-spectral matrix at some 2500 individual points. The Virginia Tech Open Circuit 0.71 meter by 0.71 meter Wind Tunnel was chosen for this study as opposed to the Stability Wind Tunnel for its size and availability. It would be unrealistic to schedule a dedicated test entry in the SWT for the time required to complete a

measurement of this scale. The size of the open circuit tunnel also made the probe mounting and traverse systems simpler. In the Stability Wind Tunnel, the probes would have needed to traverse far greater distances due to the test section size. A simpler probe setup is also favored to avoid probe collisions and vibrations in the probe mounts.

2.2.1 The Virginia Tech Open Circuit Wind Tunnel

The Open Circuit Wind Tunnel (OCWT) is powered by a 30 hp BC – SW Size 395 Twin City centrifugal fan controlled by an AF-600 General Electric variable frequency drive. The fan discharges into a 4 meter long diffuser before entering a 1.78 meter by 1.47 meter settling chamber. Aluminum honeycomb with a 0.01 meter cell size and a depth of 0.09 meters and turbulence reduction screens made from 0.3 millimeter diameter fiberglass are used to reduce the flow instabilities due to the blower. The contraction is based on a fifth order polynomial profile with a contraction ratio of 5.5:1. The maximum speed of this facility is 26 m/s at a fan setting of 1180 RPM. The wind tunnel has a freestream turbulence intensity of 0.4% of the freestream velocity. A schematic of the open circuit facility is shown in Figure 2.7. The facility exhausted into a jet catcher constructed from an aluminum frame and composite panels. The catcher deflects and diffuses the incoming jet using flow reduction screens to limit the impact of the flow on the surroundings. The closed test section had a square cross section with a side length 0.71 meters and an overall length of 1.22 meters and was installed directly downstream of the contraction exit.

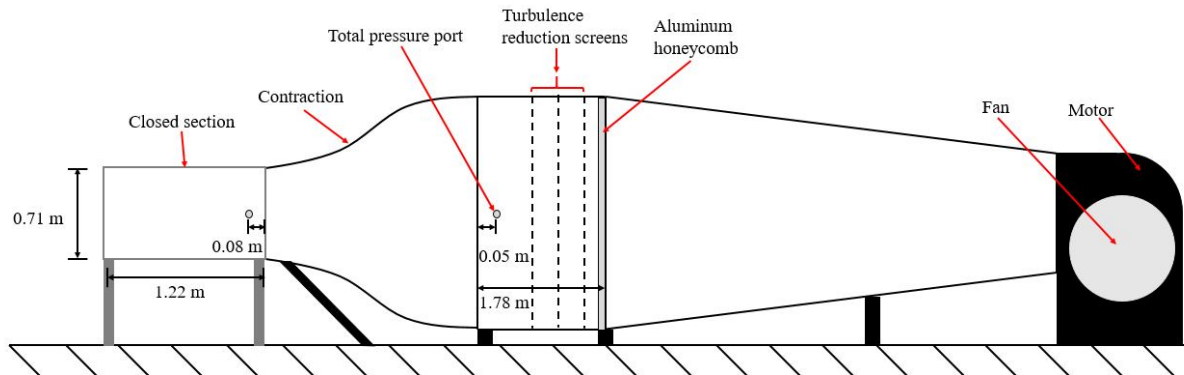


Figure 2.7. Schematic of the open circuit wind tunnel. Not drawn to scale.

The top and port side panels of the test section are made from 0.25 in aluminum sheet while the floor and starboard wall were machined pieces of half inch thick Lexan. The setup of the closed section is shown in Figure 2.8 with the aluminum extrusions that make up the test section and the aluminum anchors used to secure the side panels labeled. The wall panels were inserted into the slots of the aluminum extrusions and anchored at the upstream and downstream ends of the test section using aluminum stock secured to the aluminum extrusions. To provide a clean transition between the perpendicular wall panels triangular fillets with base lengths of 2.25 inches were printed from model resin using an Objet30 rapid prototyping machine. The fillets were secured to the wall and ceiling panels using double sided carpet tape. When the closed section was properly aligned there was a small gap, no more than half of an inch, between the nozzle exit and the start of the closed test section. Mylar transitions were installed along the 0.71 upstream edges of the test section to ensure that the flow entering the test section did not encounter a step upon entering

the test section. Foil tape was used to securely fasten the transitions and provide a smooth transition between surfaces. Figure 2.9 below shows the closed section positioned downstream of the nozzle. In this figure the flow is out of the page. Measurements documenting the flow quality of this facility are presented in Section 2.2.10.

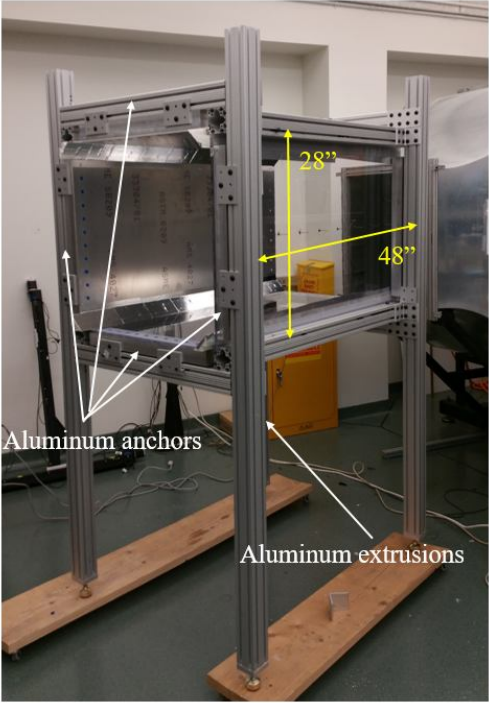


Figure 2.8. The closed test section.

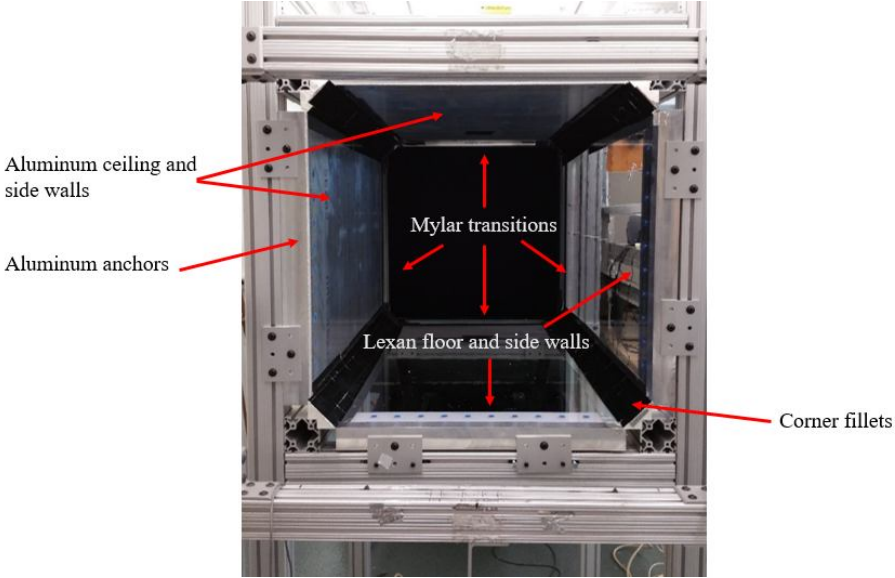


Figure 2.9 View looking upstream into the closed test section

2.2.2 Reference Measurement Systems

The test section has 19 pressure taps that are installed in a streamwise row on the starboard wall to measure the reference velocity and measure the pressure distribution on the test section wall. During the measurements the freestream total and static wall pressures were measured using a Measurement Specialties 9816/98RK pressure scanner with an accuracy of 0.05% full scale. The 19 wall static ports were measured along with the plenum pressure. The pressure ports are spaced every 5 inches (0.127 meters) in the streamwise direction with the first port 3 inches (0.076 meters) from the start of the test section. The pressure tap locations are shown in Figure 2.10. The two pressure ports located 43 inches downstream of the start of the test section were used for probe calibration in the two-point hotwire measurement. The taps were located at the mid-height of the port-side test section wall. The reference velocity was computed using the farthest upstream static port located 3 inches downstream of the nozzle exit and the plenum port located 2 inches (0.05 meters) upstream of the start of the nozzle downstream of the turbulence reduction screens. These reference ports are located in the wind tunnel diagram shown in Figure 2.7 above. The flow temperature was measured during testing using a bare wire thermocouple placed near the test section exit. The thermocouple was operated using an Omega DP80 digital process indicator. The flow temperature was resolved within 0.5 degrees Fahrenheit. The ambient pressure was recorded at the beginning of each measurement using a CNMC Model DBT-100T digital barometer and did not fluctuate during the measurements. For initial flow quality and wake verification measurements a straight Dwyer 167 twelve inch Pitot static probe was sampled using the Measurement Specialties scanner. The probe computed the static pressure by averaging over 6 static ports that were 0.875 inches from the probe tip. The Pitot static probe is shown in Figure 2.11 inside the test section where a cross section measurement was being performed in initial flow quality measurements 10 inches from the start of the test section. A flattened Pitot probe manufactured in house was used to measure boundary layer profiles in the test section. The flattened Pitot probe setup for a measurement characterizing the boundary layer of the floor of the test section and probe dimensions are shown in Figure 2.12. Note that the coordinate normal to the test section floor is z in this figure.

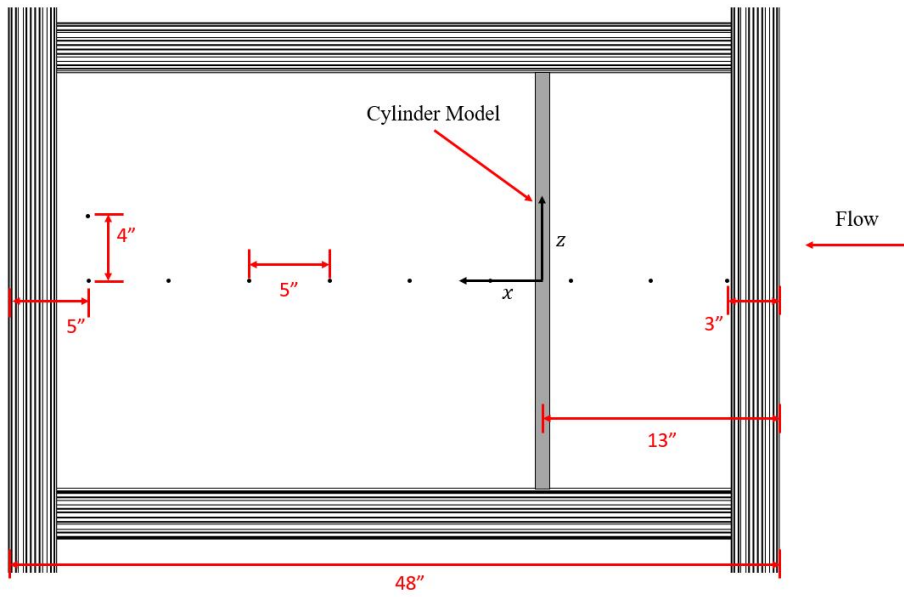


Figure 2.10. The pressure tap locations in to closed section of the Open Circuit Wind Tunnel



Figure 2.11. The Pitot static probe mounted inside the test section.

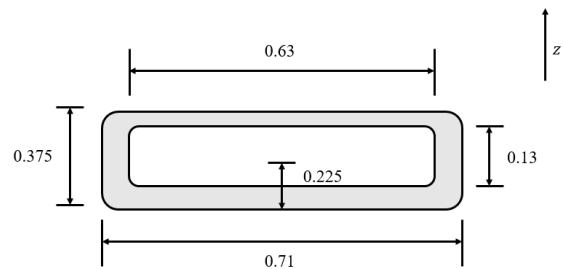


Figure 2.12. Boundary layer measurement setup (left) and the dimensions of the opening of the flattened Pitot probe in millimeters (right).

2.2.3 Test Model Setup

In the Open Circuit Wind Tunnel test a new cylinder model was required due to the size of the facility. A 38.1 millimeter diameter aluminum bar was turned on a lathe to produce the cylinder test model. The machine finish was near polished to match the model used in the Stability Wind Tunnel. The cylinder was mounted 0.33 meters downstream of the test section entrance and centered between the port and starboard walls, 0.35 meters from each wall. The cylinder was vertically mounted in the aluminum and Lexan panels. A hole was cut from the aluminum panel such that the cylinder would easily pass through without damaging the surface finish. The top of the cylinder was mounted using an aluminum extrusion that ran horizontally across the test section. A bracket was bolted to the top of the cylinder and was used to secure the top of the cylinder model to the test section frame. The cut out in the Lexan floor panel was aligned with the hole cut in the top panel and was a slightly undersized so that the cylinder needed to be rotated and pressed into place. This tight fit was used as the only anchor on the bottom surface of the test section. Like in the Stability Wind Tunnel, flow fences were designed for the new cylinder model and are shown in Figure 2.13. The fences followed the same designs as the Stability Wind Tunnel fences, but were scaled down for the cylinder and test section size. The difference in flow quality with and without the fences installed is shown in Section 3.2.1. Note that based on these measurements, the flow fences were not ultimately used in the Open Circuit Wind Tunnel experiment.

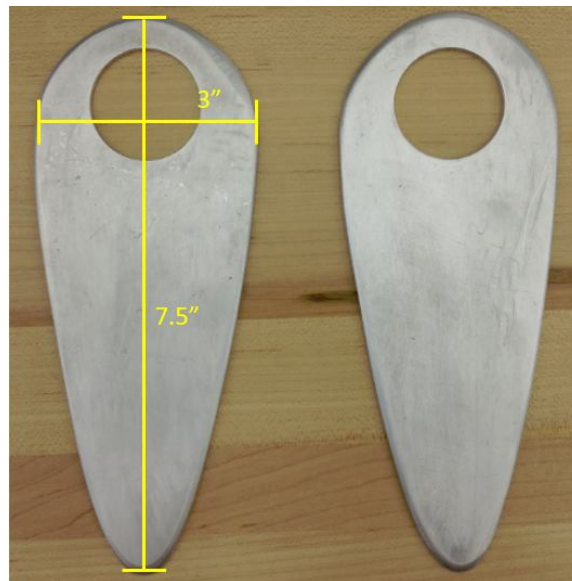


Figure 2.13. Flow fences tested in the open circuit test.

2.2.4 Coordinate System

By design the coordinate system in the open circuit test was chosen to be identical to the system used in the Stability Tunnel measurements. The origin of the wake coordinate system was located at the mid-span of the cylinder. The x axis was positive in the direction of the freestream with the center located 0.33 meters downstream of the start of the test section when looking upstream. The y axis was perpendicular to the wake and was positive pointing towards the starboard side of the

test section. The z axis pointed directly upward and was aligned with the cylinder axis. Figure 2.14 shows the cylinder mounted inside the test section with the coordinate system labeled.

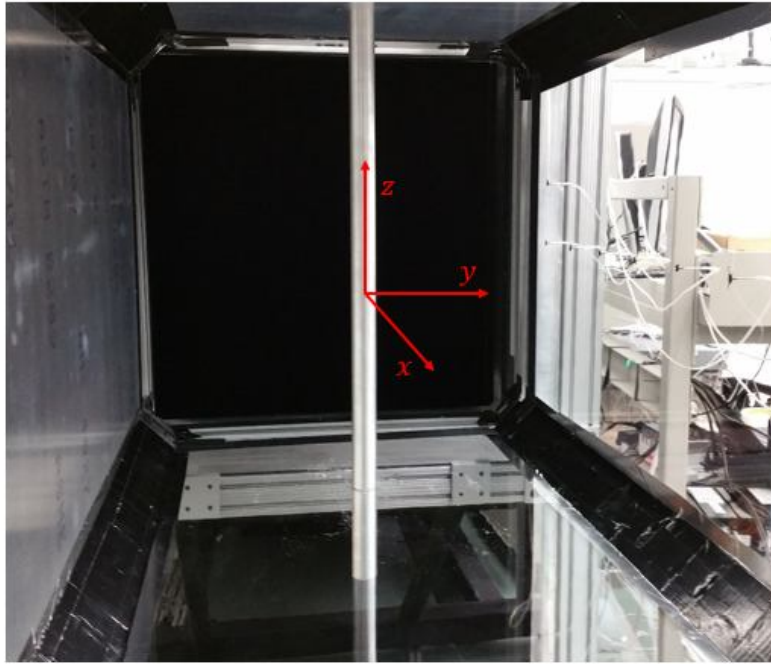


Figure 2.14 View looking upstream showing the cylinder mounted 13 inches downstream of the inlet.

2.2.5 Test Matrix

Several measurements types were made in the open circuit wind tunnel. The empty test section flow quality was measured at twenty diameters downstream of the cylinder location using a Pitot static probe. To further document the flow through the empty test section a flattened Pitot probe with an opening of 0.3 mm was used to measure boundary layer profiles 0.6 meters downstream from the start of the test section on the floor, ceiling and side walls. In the flattened Pitot measurements the flow velocity was computed using the upstream most wall static port located 3 inches from the start of the test section. Preliminary cylinder wake measurements included Pitot probe cross sections twenty diameters downstream of the cylinder with and without boundary layer flow fences installed. These measurements were designed to assess the two-dimensionality of the cylinder wake. For each pressure measurement the Pitot-static probe was sampled using the Measurement Specialties pressure scanner. These preliminary flow measurements that documented the clean flow of the test section and the two-dimensionality of the cylinder are presented in Section 2.2.6. For each pressure measurement the wind tunnel was operated at a velocity of $26 \text{ m/s} \pm 0.5 \text{ m/s}$ and an actual cylinder diameter Reynolds number of $60\,979 \pm 195$. The Pitot static probe was used to measure mean velocity profiles, and four sensor hotwire probes were used to measure three component velocity profiles and Reynolds stresses. The primary goal of the Open Circuit Wind Tunnel test was to measure the two-point correlation tensor in the cylinder wake. To accomplish this goal, two quad-hotwire probes were sampled simultaneously.

One probe was held in a fixed position while the second probe was traversed in a grid around the fixed probe. In total nineteen independent grids were measured for fixed probe positions spanning from $-3.4 < y/L_w < 3.4$ where L_w is the half wake width. The hotwire probes are discussed in Section 2.3 and the measurement approach is discussed in Section 3.2.4.

2.2.6 Open Circuit Wind Tunnel Traverse System

A separate traverse system from that used in the Stability Wind Tunnel was used in the Open Circuit Wind Tunnel to complete the single point profiles and the two point hotwire measurements. Three independent Velmex BiSlide traverses were used in this setup. A three axis VXM controller was used with a VRO digital encoder readout were used to position the hotwire probes within 0.001 inches. Two BiSlides were attached together to form a two-axis traverse system that could be mounted to the top of the test section frame. A single axis BiSlide traverse was mounted to the downstream end of the test section to position the fixed probe in the cylinder wake in the y direction. In all of the discussion that follows, the fixed probe position variables are y and z while the moving probe position variables are y' and z' . The moving probe was traversed in the y' and z' directions around the fixed probe using the two axis system. In Figure 2.15 (right) the directions that each probe was traversed are labeled. Each probe was held on a support such that the probe tip was twenty diameters downstream of the cylinder center. The probe positions were controlled using an in house Matlab code capable of positioning the moving probe at locations in a predetermined grid. At each independent point, the acquisition code sampled the fixed and moving probes simultaneously. Figure 2.15 below shows the traverse setup in the closed section with the traverse axes labeled.

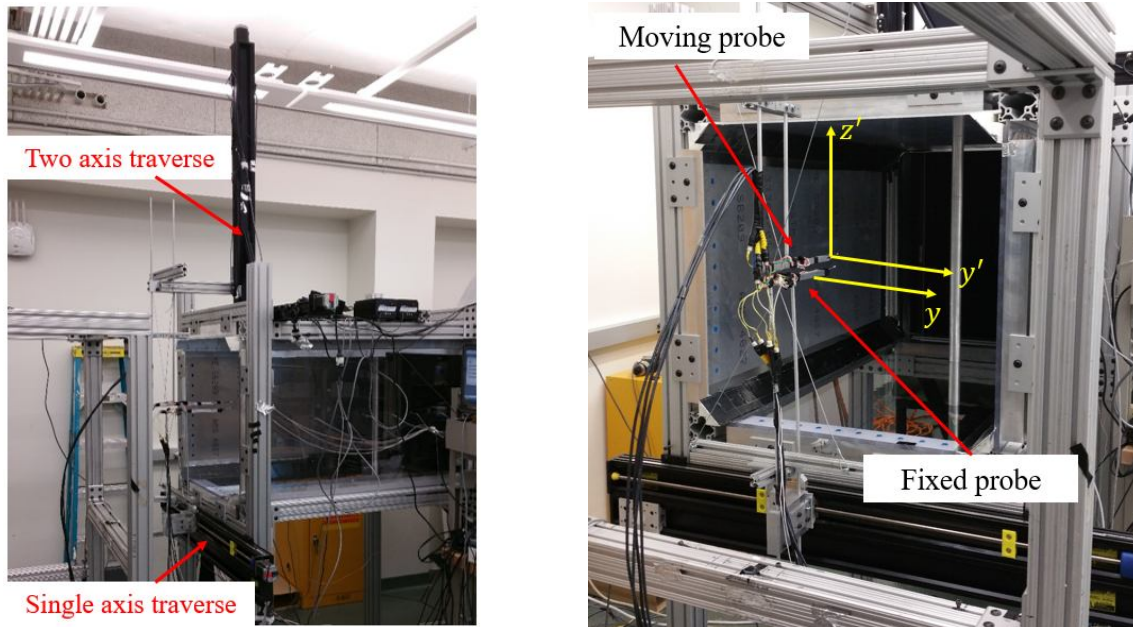


Figure 2.15 The fixed and moving probe traverses mounted to the Open Circuit Wind Tunnel test section (left) and the moving probe directions.

2.2.7 Flow Characterization Measurements

In the Open Circuit Facility measurements to document the flow through the test section with no blockage preceded any cylinder wake measurements. The mean-flow uniformity of the empty test section flow is shown in Figure 2.16. The flow was sampled using the Pitot-static probe and Measurement Specialties pressure scanner previously described. The cross section was measured by traversing the Pitot static probe in a uniform grid on y and z using the two-axis moving probe traverse. The color levels correspond to the probe velocity normalized on freestream velocity. The axis limits represent the walls of the closed section. The velocity points in the grid have all been normalized on the nominal freestream value of 26.5 m/s. The figure shows that the flow is uniform within $\pm 2\%$ of the nominal freestream. The results from the boundary layer profile measured 0.61 meters downstream of the start of the test section and in the test section center using the flattened Pitot probe are shown in Figure 2.17. The velocity was normalized on the freestream velocity of 26.5 m/s. The boundary layer thickness can be computed from this profile by finding the vertical location where the normalized velocity is 99 percent of the freestream. This analysis determines that the boundary layer thickness in the center of the test section is 42.7 ± 0.1 mm.

Cylinder wake cross sections were measured to assess the two dimensionality of the flow with and without flow fences. The same Pitot static probe was traversed in an identical grid to the empty test section measurements and the pressures were recorded using the same Measurement Specialties scanner. Figure 2.18 plots a cross section of the flow measured twenty diameters downstream of the cylinder center without the fences installed while Figure 2.19 plots a wake cross section measured with the fences installed at the same streamwise cross section location. The end plates were installed 76.2 millimeters from the floor and ceiling of the test section. This position was chosen since it would be double the boundary layer thickness at the test section center. The boundary layer would of course be thinner at the cylinder location than the boundary layer thickness measured 0.28 meters downstream of the cylinder center. As in the plot of the empty test section flow quality, the axis limits represent the walls of the test section. The white rectangles included in these figures correspond to the measurement region sampled in the full two-point measurement. The two-dimensionality of the flow in this region was the most important. The cross section results show that the two dimensionality of the flow is better without the boundary layer splitter plates installed and thus the cylinder wake was studied without the flow fences for all of the following measurements.

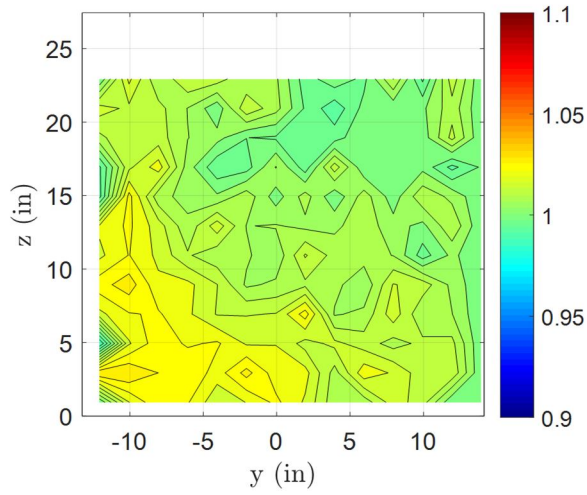


Figure 2.16. Empty test section normalized velocity contour.

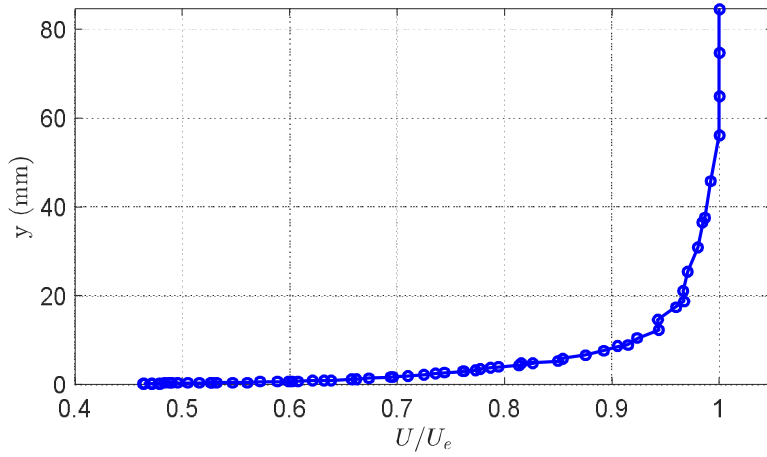


Figure 2.17. Boundary layer profile measured in the center of the test section.

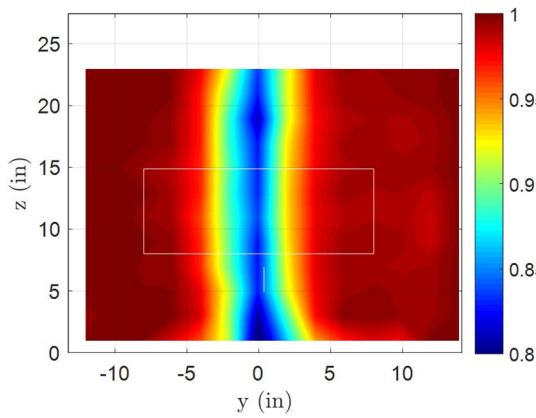


Figure 2.18. Wake cross section measured without cylinder end plates

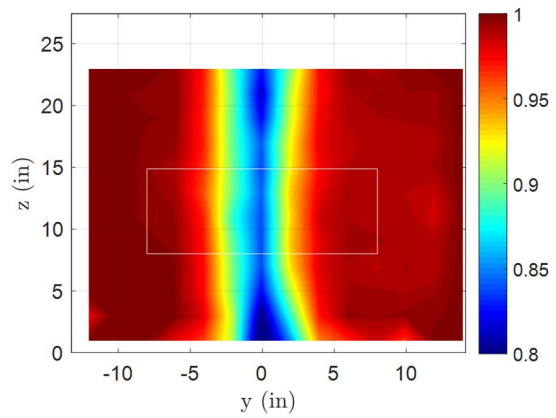


Figure 2.19. Wake cross section measured with cylinder end plates.

2.3 Hotwire Anemometry

2.3.1 Hotwire Probes

The wake profiles measured in the Stability Wind Tunnel and the two-point hotwire measurements performed in the Open Circuit Facility were completed using two four-sensor probes. These quad wire probes used were manufactured by Auspex Corporation (type AVOP-4-100). Single hotwire probes also manufactured by Auspex Corporation (type AHWU-100) were also used in the Stability Wind Tunnel measurements. The single hotwire probe is only able to resolve the flow velocity perpendicular to the hotwire sensor. The four sensor probes are able to resolve three components of velocity simultaneously and have a measurement volume of 0.5 mm^3 (Wittmer *et al.*, 1998). The quad-wire probes use two x-wire arrays with each wire inclined at 45 degrees relative to the probe axis. Wittmer *et al.* (1998) fully describe the methods used to resolve three components of velocity using the four hotwire sensors on a single probe. Figure 2.21 shows the hotwire schematic of the probe geometry described by Wittmer *et al.* (1998). Before measurements were performed, the probes were calibrated for flow angle and velocity. During the measurements, the probes were recalibrated to adjust for temperature drift. Through careful calibration, the voltages measured by the anemometer system were converted to the three velocity components using King's Law. Figure 2.20 shows a close up of the two hotwire probes uses in the Stability Wind Tunnel test campaign. In this facility two probes were sampled simultaneously to provide redundant single-point measurements.

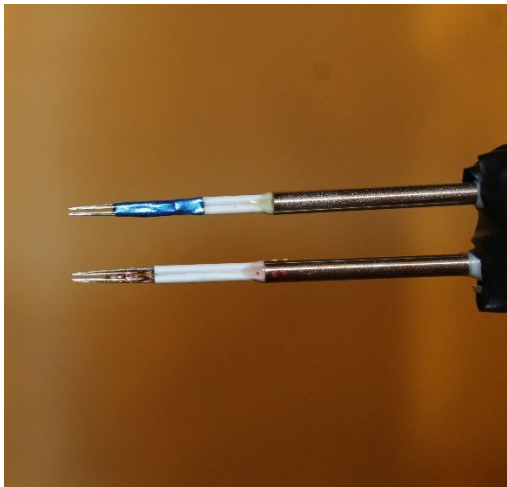


Figure 2.20 Close up of the two quad-hotwire probes.

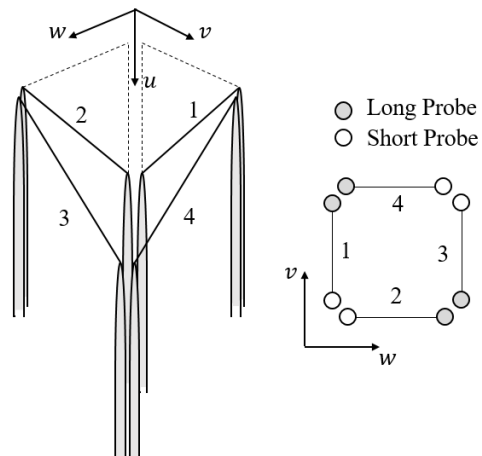


Figure 2.21 The quad-wire geometry of the probes described by Wittmer *et al.* (1998).

2.3.2 Constant Temperature Anemometry

The single-wire and quad-wire probes were operated by Dantec Dynamics Streamline Constant Temperature Anemometry System. Four Dantec 90C10 CTA modules were installed in a Dantec 90N10 frame. Each sensor on the four sensor probes required a separate bridge module to operate the sensor. The frequency response of each module was tested prior to any measurement. The CTA modules each had a built in feature where the bridge could be excited by a square wave. The square wave function was used to test the impulse response of each bridge module by setting the duration of the square wave to be 0.01 milliseconds. Each CTA bridge had a flat frequency response up to

10 kHz and had a built in signal conditioner and amplifier. The anemometer signals were amplified by a factor of 16 and offset by two volts for acquisition. Each of the CTA's signal output was recorded using an NI-9239 cDAQ module. For the two point hotwire measurement, two four-channel DAQ modules were required. Each module was installed in a NI 9174 USB cDAQ chassis. When installed in the chassis all eight channels from the two NI-9239 modules could be sampled simultaneously up to 50 kHz at an accuracy of 0.03% of the measurement. The NI-9239 DAQ module used had a range of ± 10 volts at a 24-bit resolution. In the present study the hotwire signals were sampled 10 000 times at 50 kHz for fifty consecutive records. The DAQ modules had a built in anti-aliasing filter that produced an alias free bandwidth of 22.6 kHz.

2.3.3 Velocity and Angle Calibration

The quad-wire probes required two calibrations, one for velocity and one for flow angle. To calibrate the probes for velocity the probe was positioned in a uniform jet or in the freestream of the wind tunnel. In a typical velocity calibration eleven to fifteen points were recorded. The flow velocity was usually varied ± 10 m/s from the speed of the wind tunnel measurement. In the Stability Wind Tunnel the flow speed was varied from 10 m/s to 30 m/s while in the blow down wind tunnel test the flow speed was varied from 6 m/s to the maximum possible flow velocity of 26 m/s. At each velocity point the exact flow velocity, computed using the reference instrumentation, was recorded along with the output voltages from each of the sensors on the four-sensor hotwire probe. The probe's velocity calibration was then computed using King's Law defined by Equation 2.1. King's Law states that the square of the measured hotwire voltage varies linearly with the flow velocity raised to the power of 0.45. The constant 0.45 is an assumed constant for the hotwire probes used. The calibration constants A and B are therefore determined by computing the linear regression between the reference velocity raised to the power of 0.45 and the square of the hotwire voltage.

$$E^2 = A + BU^{0.45} \quad \text{Equation 2.1}$$

King's Law is easily manipulated to determine the measured flow velocity using the hotwire voltage output and the calibration constants. Velocity calibrations must be regularly performed during wind tunnel measurements to account for the temperature drift during a single run and between consecutive runs.

Four sensor hotwire probes must also be calibrated for flow angles. To perform this calibration, the probe is first placed in a 1-inch diameter jet and calibrated for velocity using the approach defined above. The jet is powered by a Baldor M3613T 5 horsepower motor and Cincinnati Fan HP Series II blower. The motor is operated using a Rockwell Automation VTAC-9 controller. By increasing the fan frequency, the freestream velocity of the jet is increased. When performing an angle calibration controller was used to set a frequency of fan 17 Hz which corresponded to 20 m/s ± 0.5 meters per second. The flow speed was measured using a pressure transducer with a rated accuracy of 0.01 inches of water. To perform the angle calibration, the probe pitch and yaw angles was varied from -45 to 45 degrees using two Phase II planetary geared turntables. The turntables used to pitch and yaw the probe were operated using two Applied Motion HT23-553 high torque stepper motors. The stepper motors were able to position the probe angles during calibration within 0.25 degrees. The traverses were controlled by an in house Matlab code that

traversed the probe to about 600 independent angular positions. For a typical calibration the pitch and yaw and were both varied from -45 to 45 degrees in 5 degree increments. At each combination of pitch and yaw angle the flow velocity was measured along with the outputs of the four individual hotwire sensors. At large pitch and yaw angles the probe will resolve some erroneous v and w velocity, while the jet velocity remains purely in the axial direction. The error in the v and w velocities are computed using the measured v and w velocities and the true direction of the jet velocity. This error is then used to correct the measured velocity components seen in during a measurement for a given flow angle. Wittmer *et al.* (1998) further describes this calibration procedure. The angle calibration was performed before any measurements in the wind tunnel were made and needed to be repeated each time one of the four hotwire sensors were repaired. The velocity calibrations were repeated before and after each angle calibration to account for temperature drift.

2.3.4 Quad-Hotwire Measurement Uncertainty

All the error sources contributing to the error in the final single point and two point statistics were considered in a formal uncertainty analysis. The uncertainties from each source were combined using the root sum square method. The resolution of the data acquisition system and the error due to the sampling scheme were both used to characterize the total measurement system uncertainty. The sampling scheme was designed such that enough averages could be computed to limit the random error introduced into the system. For each hotwire measurement grid the two hotwire probes were sampled simultaneously using sampling rate of 50 kHz, a record length of 10 000. The probes were sampled 50 times per grid point to provide sufficient averaging. The error in the velocity calibration was characterized using the starting and ending velocity calibration data from a single run. The quality of the calibration fit and the effect of temperature were considered in the uncertainty analysis of the velocity calibration. The uncertainty due to each individual probes' angle calibration was found to be the largest uncertainty contribution to the computed quantities. Uncertainties in the v and w velocity components angle was assumed to be 0.25 degrees. The final uncertainty source considered was in the reference velocity. The total uncertainty in the reference head was assumed to be 0.01 inches of water. Table 3.1 presents the absolute uncertainty in the single point quad-hotwire measurement results due to all the error sources listed above. Table 3.2 presents the total uncertainty in the two-point hotwire statistics. In the two-point statistics the f and m subscripts denote the fixed and moving probes respectively.

<i>Quantity</i>	<i>Absolute Uncertainty</i>
U/U_{ref}	$1.06E - 02$
V/U_{ref}	$1.35E - 02$
W/U_{ref}	$1.35E - 02$
u^2/U_{ref}^2	$6.15E - 05$
v^2/U_{ref}^2	$3.39E - 04$
w^2/U_{ref}^2	$4.82E - 04$
uv/U_{ref}^2	$4.51E - 05$
vw/U_{ref}^2	$5.94E - 05$
uw/U_{ref}^2	$9.41E - 05$

Table 3.1. The absolute uncertainty in the single point statistics.

<i>Quantity</i>	<i>Absolute Uncertainty</i>
$u_f u_m / U_{ref}^2$	$8.70E - 05$
$v_f v_m / U_{ref}^2$	$4.79E - 04$
$w_f w_m / U_{ref}^2$	$6.82E - 04$
$u_f v_m / U_{ref}^2$	$6.37E - 05$
$v_f w_m / U_{ref}^2$	$8.39E - 05$
$u_f w_m / U_{ref}^2$	$1.33E - 04$

Table 3.2. The absolute uncertainties in the two point statistics.

Chapter 3: Results

3.1. Stability Wind Tunnel Measurements

3.1.1. Measurement Summary

The first measurements performed in the present study first took place in the Stability Wind Tunnel, where single point wake profiles were measured. Single point statistics and spectra were used to compare with the results from the two-point measurement performed in a separate facility. In the Stability Wind Tunnel a two-inch diameter cylinder was positioned in the test section and profiles were measured 10, 15 and 20 diameters downstream of the cylinder center. At each location, profiles of the mean velocity and the Reynolds stress profiles were measured using quad-hotwire probes.

3.1.2. Wake Profiles

The two dimensionality of the wake flow was first characterized in the Stability Wind Tunnel (SWT) before any other measurement was performed. Wake cross sections were measured using the SWT wake rake 20 diameters downstream of the cylinder center. As stated in Section 2.1.1, the probe tips of the rake were 6.31 meters from the start of the test section. The cylinder was moved into a position 20 diameters (40 inches) upstream of the probe tips of the rake. This instrumented rake was traversed the height of the test section to measure stagnation pressure coefficient cross sections using the Pitot and Pitot static pressure probes on the rake. Figure 3.1 below shows a stagnation pressure coefficient contour map of the wake cross section measured during a single run with the wake rake without the fences installed. The pressure coefficients and has an uncertainty of $\pm 3\%$ at 20 m/s . Notice that there are two lobes in the wake at $z = \pm 20$ inches. These are due to interactions from the boundary layers of the floor and ceiling of the test section with the wake. To limit these interactions and improve the two dimensionality of the wake, boundary layer fences were installed on the cylinder 152.4 mm from the floor and ceiling of the test section. Figure 3.2 presents a wake cross section measured at the same streamwise station with the boundary layer fences installed. The fences improved the lobes seen near the ends of the cylinder near $z = \pm 20$ inches. To quantify the two-dimensionality three profiles were extracted from the cross section. Figure 3.3 compares profiles extracted at 0 and ± 15 inches along the cylinder span. The dashed lines included in the comparison represent ± 3 uncertainty levels. The cylinder wake was therefore determined to be acceptably two dimensional, within the measurement uncertainty, over the centered 30 inches of the cylinder span. This proved sufficient for the present study.

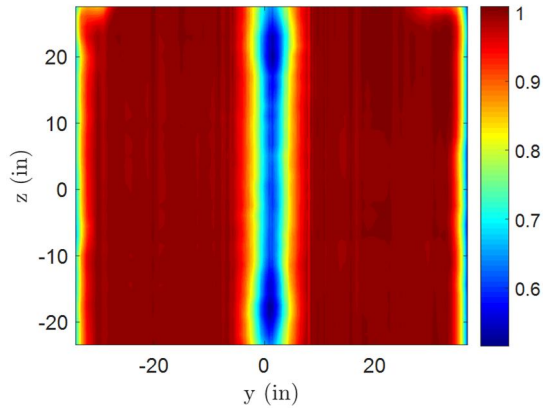


Figure 3.1 Stagnation pressure coefficient wake cross section without the fences installed

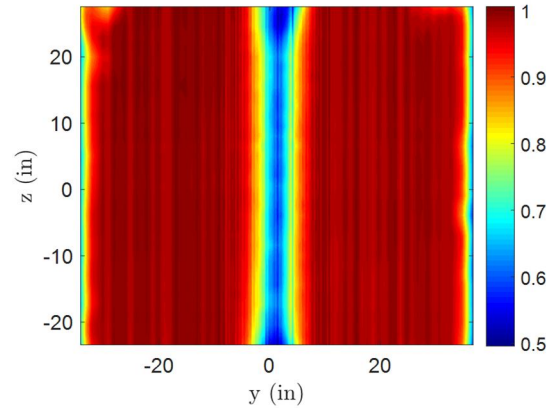


Figure 3.2. Stagnation pressure coefficient wake cross section with the fences installed

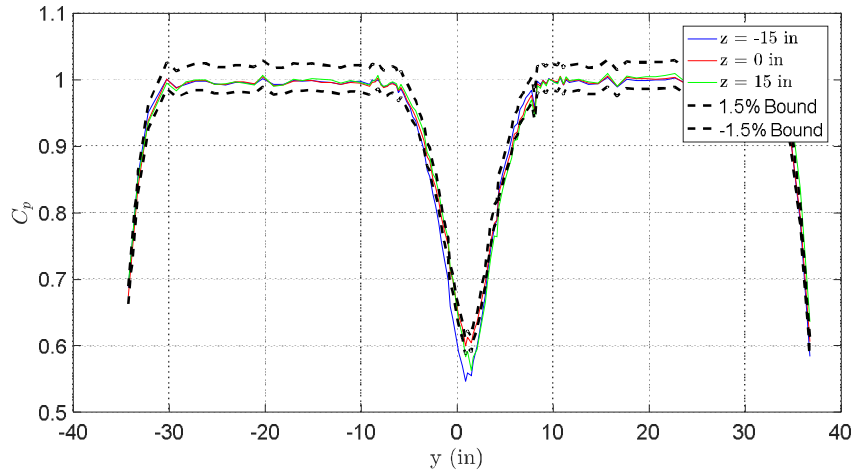


Figure 3.3. Stagnation pressure coefficient profiles from the wake survey

After the two-dimensionality of the cylinder was characterized, wake profile measurements were made with quad-hotwire to document the Reynolds stress profiles in the cylinder wake. The cylinder wake was measured for a freestream velocity of 20 m/s at stations 20, 15 and 10 diameters downstream of the cylinder center at the cylinder midspan, $z = 0$. Figure 3.4 shows the three components of velocity through the cylinder wake normalized on the freestream velocity for the measurements performed 20 diameters downstream of the cylinder center. As expected the v and w velocity components are near zero. The maximum deficit velocity was normalized on the free stream was 0.22 and the half wake width normalized on the cylinder diameter was 1.49 inches. Figure 3.5 and Figure 3.6 plot the Reynolds stress profiles normalized by the square of the freestream velocity at 20 diameters downstream of the cylinder center. The normal stresses show that the wake-normal Reynolds stress, $\overline{v^2}$, is largest, followed by the $\overline{u^2}$ stress and the $\overline{w^2}$ stress. The Reynolds shear stress, \overline{uv} , dominates the shear stresses as \overline{uw} and \overline{vw} are near zero. Devenport *et al.* (2001) and Wagnanski *et al.* (1986) show similar trends in the Reynolds relative magnitudes of the Reynolds stresses in the measurements both studies performed in plane wakes.

The uncertainties in the hotwire velocities and Reynolds stresses for the single point measurements were presented in Section 2.3.4.

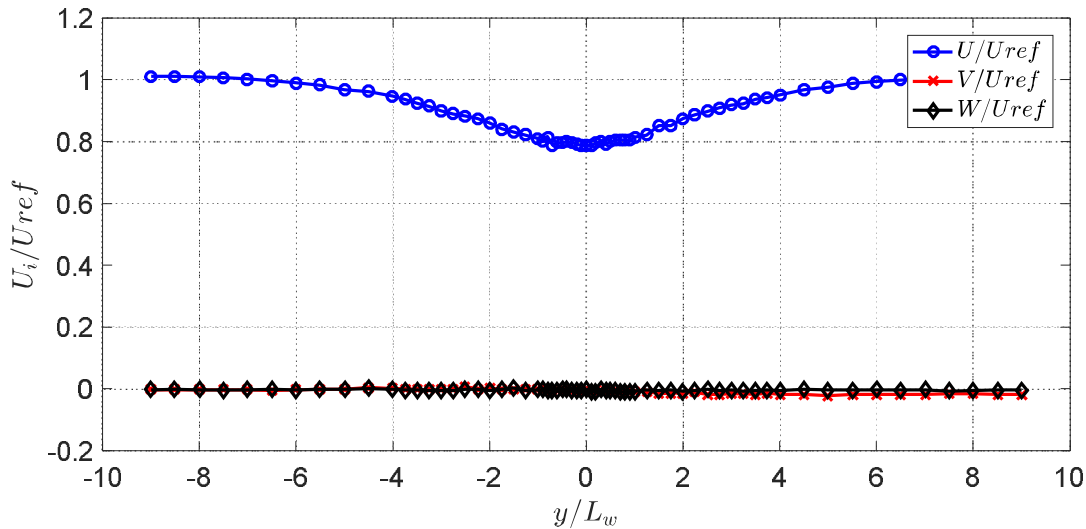


Figure 3.4 Mean velocity profiles measured in the Stability Wind Tunnel

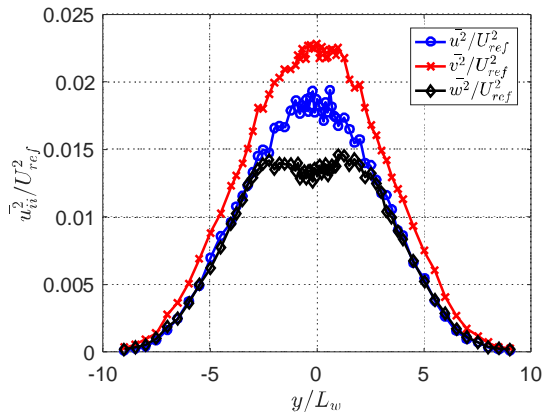


Figure 3.5. Normal Reynolds stress profiles measured in the SWT wake.

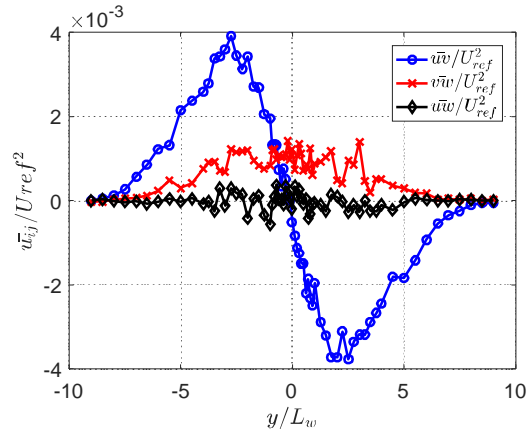


Figure 3.6. Cross Reynolds stress profiles measured in the SWT wake.

The single point hotwire measurements performed 10 and 15 diameters downstream of the cylinder center were analyzed to assess the growth rate of the wake. In Figure 3.7 the variations in the in the maximum velocity deficit U_w and half-wake width L_w normalized on the cylinder diameter are shown as functions of streamwise position for the cylinder wakes measured in the Stability Wind Tunnel and in the Open Circuit Facility. These scales were computed using the mean velocity profiles measured with the quad-hotwire probes. The variation in scales show that as the streamwise distance from the cylinder center increases the half wake width increases and the velocity deficit decreases. Included in Figure 3.7 are the length and velocity scales estimated using the square root growth and decay of the streamwise distance from the cylinder with an origin close to the cylinder center. Devenport *et al.* (2001) and Wygnanski *et al.* (1986) both show that when

the plane wake is fully developed, the half wake width and deficit velocity closely follow these growth and decay trends. Figure 3.7 shows that these estimations of scales do not yet agree with the measured length and velocity scales. This shows that the cylinder wake measured in the Stability Wind Tunnel was not fully developed 20 diameters downstream of the cylinder. The deficit velocity shows the biggest discrepancy where the estimated scales are higher in magnitude and decay more rapidly than the measured scales.

Figure 3.8 compares the mean velocity wake profiles at the three streamwise stations. The profiles have been normalized using the maximum deficit velocity and half wake width and show good agreement with each other. Each normalized profile is within 3% of each other. Figure 3.9 through Figure 3.14 show the Reynolds stresses measured at 20, 15 and 10 diameters downstream of the cylinder. Each component of the Reynolds stress tensor has been normalized on the deficit velocity squared and the half wake width. At each measurement location the \overline{uw} and \overline{vw} stresses are near zero at each as expected in a plane wake. Figure 3.9 and Figure 3.11 show that the normalized $\overline{u^2}$ and $\overline{w^2}$ stresses measured at 10 and 15 diameters downstream normalize to nearly the same profile while the $\overline{v^2}$ stress changes significantly between each streamwise station. The \overline{uv} stress shows nearly no variation in the three normalized profiles. These comparisons in the normalized Reynolds stress profiles show that the wake is not yet fully developed since the normalized profiles are not yet self-similar.

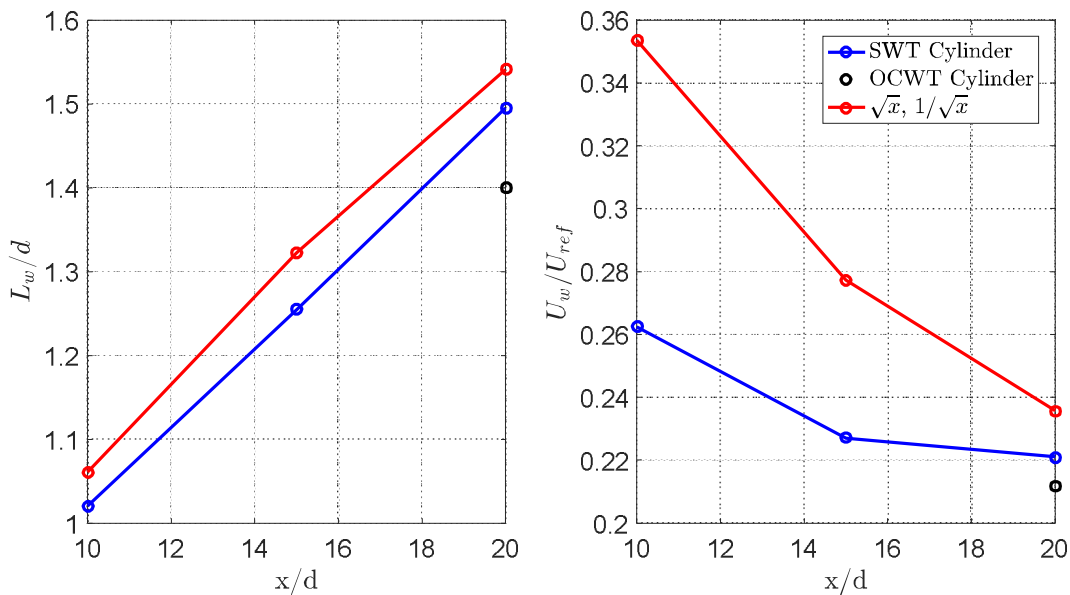


Figure 3.7. The variation in the half wake width (left) and the deficit velocity (right).

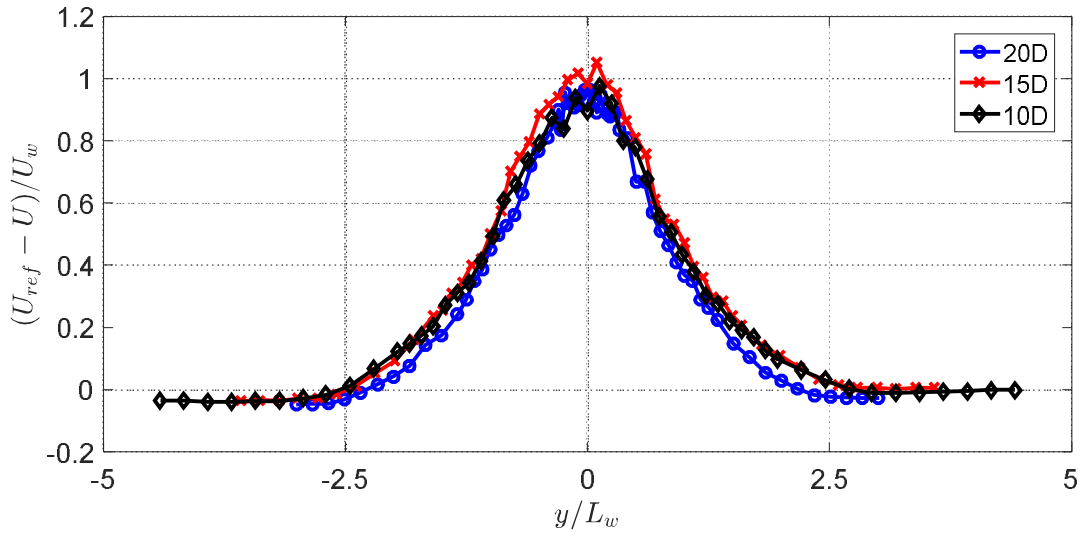


Figure 3.8. Evolution in the mean U velocity of the SWT wake.

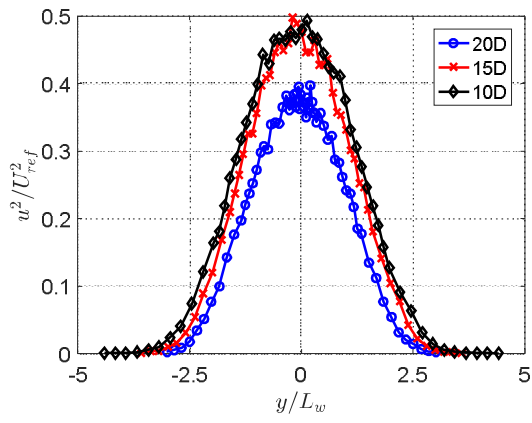


Figure 3.9. Evolution in the $\overline{u^2}$ Reynolds stress profile.

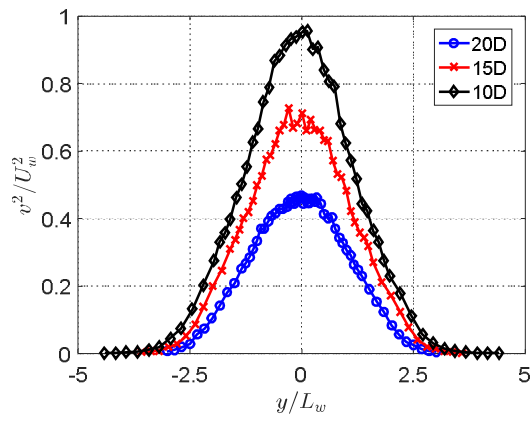


Figure 3.10. Evolution in the $\overline{v^2}$ Reynolds stress profile.

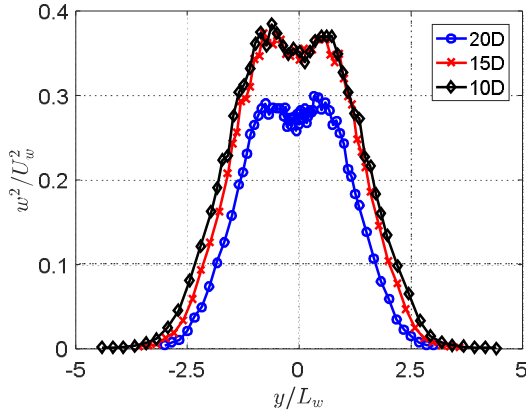


Figure 3.11. Evolution in the $\overline{w^2}$ Reynolds stress profile.

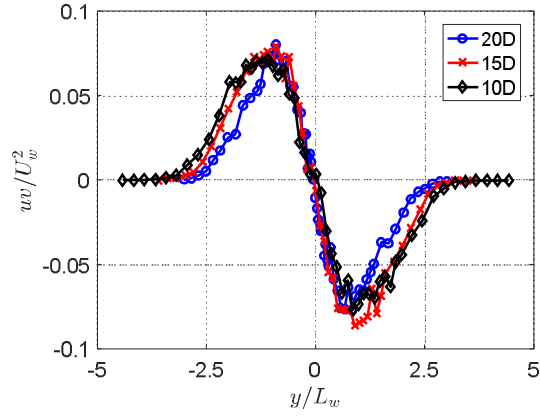


Figure 3.12. Evolution in the \overline{uv} Reynolds stress profile.

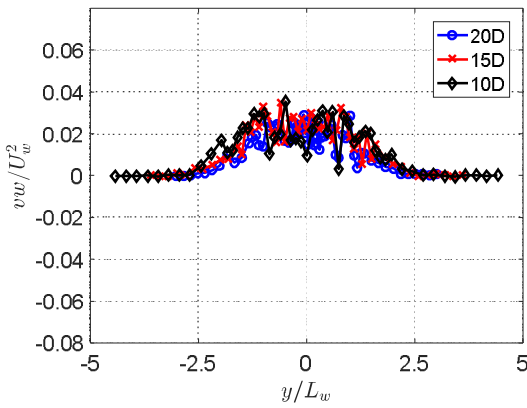


Figure 3.13. Evolution in the \overline{vw} Reynolds stress profile.

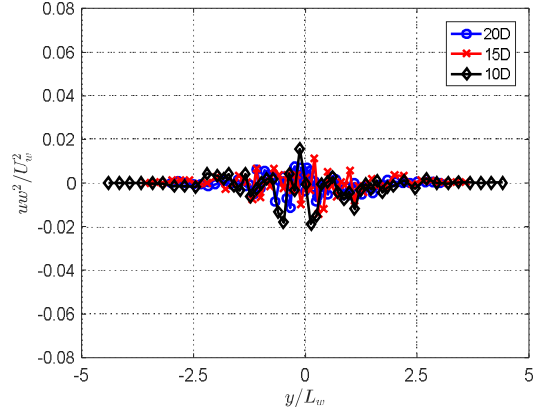


Figure 3.14. Evolution in the \overline{uw} Reynolds stress profile.

At each measurement point the full cross-spectral matrix was measured. Figure 3.15 through Figure 3.17 show the evolution in the autospectral densities for the u , v and w velocity components respectively measured at on the wake centerline. The autospectral density has been normalized on the reference velocity squared for each component of velocity. The autospectra are presented at the wake centerline for each fluctuating velocity component. In the spectral density comparison for the v component of velocity there are noticeable peaks located at 73.24 Hz due to the vortex shedding of the cylinder. The shedding frequency remains constant for the three measurements performed at the three streamwise distances. The shedding frequency of 73.24 Hz implies a Strouhal number of 0.19, which closely matches the Strouhal number of the study performed by Neumann *et al.* (2009) in a cylinder wake measured at a Reynolds number of 1200. In each comparison of the autospectra the data has been clipped at 20 kHz, before the data acquisition begins to alias the high frequency content. In each component of velocity the levels are on the same magnitude for the three streamwise stations, however there is a clear trend that the energy increases as the measurement location moves toward the cylinder. At each streamwise station and

in each component of the autospectrum there is a change in slope around 7 kHz. These features are not physical characteristics of the flow, but rather artifacts of the probe's dynamic response.

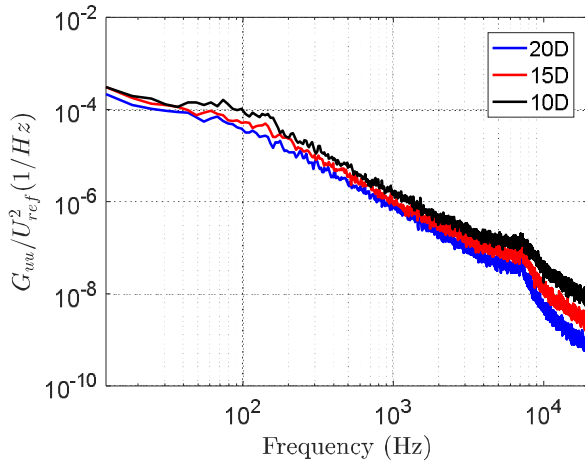


Figure 3.15. Evolution in the G_{uu} autospectral density.

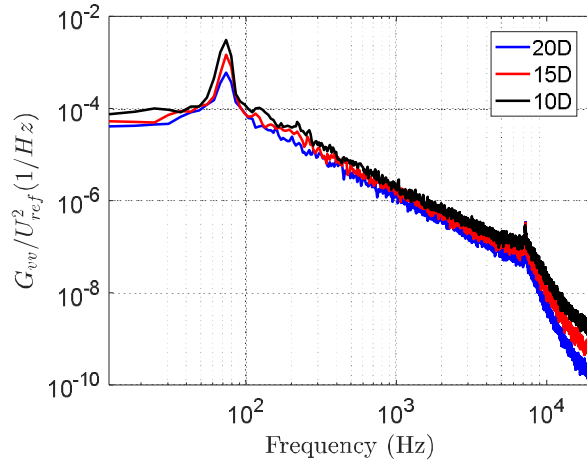


Figure 3.16. Evolution in the G_{vv} autospectral density.

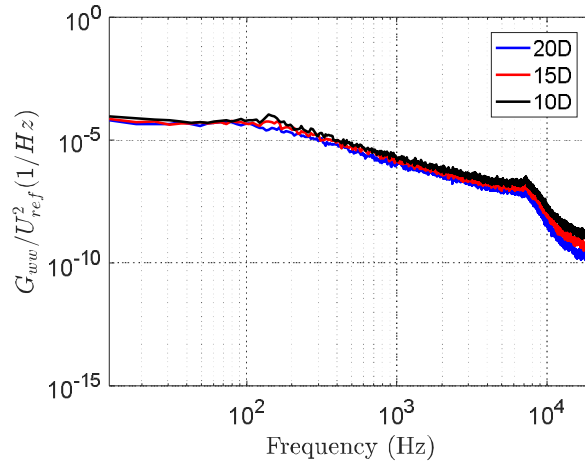


Figure 3.17. Evolution in the G_{ww} autospectral density.

3.2 Open Circuit Wind Tunnel Measurements

In this section the results from the Open Circuit Wind Tunnel test are discussed. To provide a clear sense of direction in this chapter, the order of the measurements performed and the steps taken in the data reduction must be discussed. The first cylinder wake measurements performed in the Open Circuit facility were Pitot-static probe cross sections to document the two-dimensionality of the wake. Pitot-static profiles were then performed in the cylinder wake to determine the deficit velocity and half wake width and to compare with the wake measured in the Stability Wind Tunnel. Reynolds stress profiles were measured to ensure that wakes measured in each facility were similar

when normalized on their appropriate length and velocity scales. After the two cylinder wakes were judged to be similar, the focus shifts to the two point measurement approach and data reduction. The two-point time delay correlation formulation is described in the context of the measurements performed by the present study to give context to the measurement approach and the results discussed in this results section. During acquisition the Reynolds stress profiles were plotted for each measurement grid to check that the stress profiles from each grid were consistent with each other. In checking the repeatability of the grid measurements, some inconsistencies were found in the Reynolds stresses measured at each grid point between different measurement grids. The cause of these inconsistencies will be discussed along with the corrections applied to the data set and the justifications for correcting the data.

The focus then moves to the two-point correlation results. The two-point correlation measurement consisted of 19 measurement grids each with between 120 and 230 individual points. The flow was sampled such that the full cross-spectral matrix could be computed at each measurement location. The methodology and assumptions made to combine the 19 measurement grids during data reduction are discussed. Then the fully reduced two-point correlation function measured in the cylinder wake, was used to analyze two-point correlation cross sections and in a proper orthogonal decomposition analysis. The decomposition analysis resulted in the determination of compact eddy structures in the cylinder wake. The two-point correlations, proper orthogonal modes and compact eddy structures were ultimately compared with the equivalent results computed using the correlation function measured by Devenport *et al.* (2001) so that the differences in the two wake flows could be assessed.

3.2.1 Documenting the Two-Dimensionality of the Cylinder Wake

The two dimensionality of the wake was investigated before any single or two point hotwire measurements were made. Figure 3.18 shows a wake cross section measured with a Pitot static probe 20 diameters downstream of the cylinder center. The uncertainty in the velocity computing using the Pitot probe was computed to be 0.3 m/s. In this cross section the wind tunnel walls correspond to the limits of the figure's axes. The contour levels correspond to the probe velocity normalized on the freestream. The full two-point measurement region spanned from -8 to 8 inches in y and from 8 to 15 inches in z . This region is shown in the figure as a white rectangle. Profiles have been extracted from the wake cross section at z locations of 7, 11 and 15 inches and are compared in Figure 3.19. Included in the comparison are $\pm 1\%$ uncertainty bounds computed using the mean of the extracted profiles. These error limits show that the minimum velocity and wake width do not vary more than $\pm 1\%$ inside the measurement region within the coarse resolution of the measured profiles. This comparison shows that the wake inside the measurement region was acceptably two-dimensional for the present study.

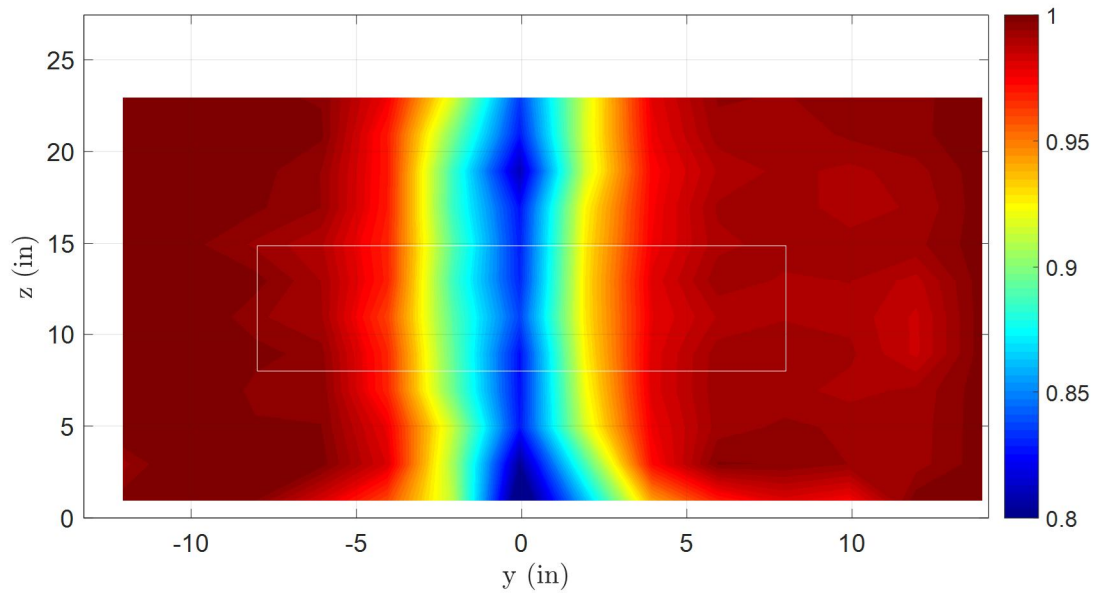


Figure 3.18. A wake cross section 20D downstream of the cylinder center.

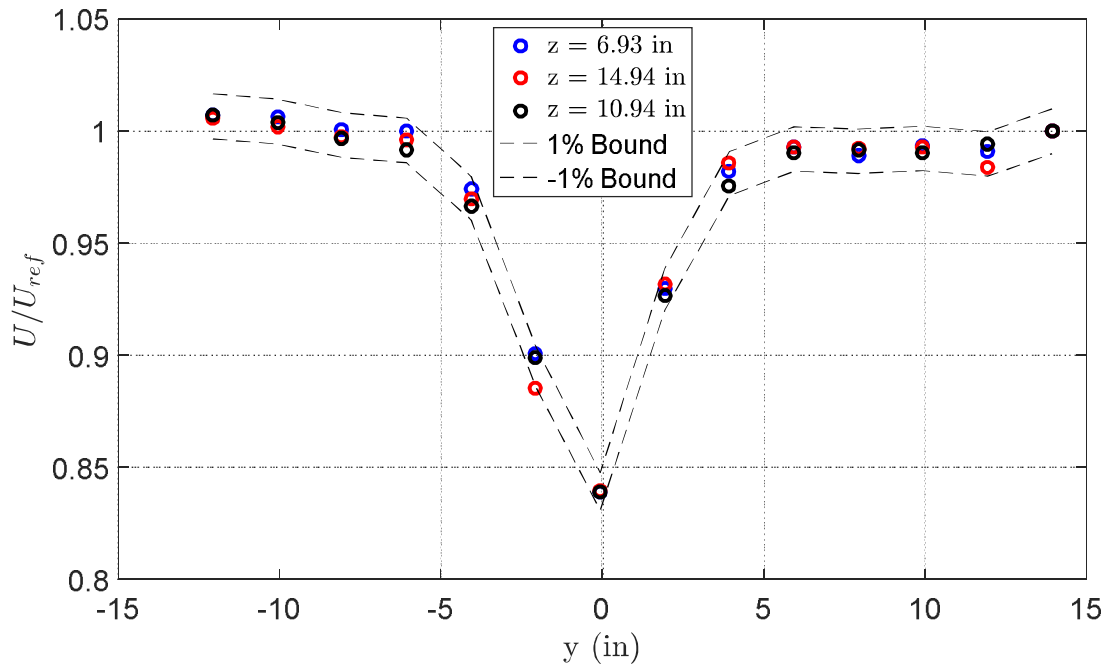


Figure 3.19. Comparison of pressure profiles from the cylinder wake cross section measurement.

3.2.2 Comparing the Stability Wind Tunnel and Open Circuit Wind Tunnel Wakes

After the two-dimensionality of the cylinder wake in the Open Circuit facility was documented, single point quad-hotwire measurements were made to confirm that the wakes measured in the SWT and the OCWT were similar. To determine the half wake width in the Open Circuit facility a Pitot-static profile was measured twenty diameters downstream of the cylinder center at the cylinder's midspan. In the Open Circuit facility the cylinder wake had a maximum deficit velocity normalized on the freestream of 0.21 and a half wake width normalized on the cylinder diameter 1.4. The scales computed in the cylinder wake in the OCWT are compared with the scales measured in the SWT in Figure 3.7. Figure 3.20 compares the streamwise velocity profiles from the measurements performed in the cylinder wakes from the two facilities. In the Stability Wind Tunnel the velocity profile was measured using a quad-hotwire probe while the profile measured in the Open Circuit Wind Tunnel was measured using the straight Pitot-static probe. Each velocity profile has been subtracted from the freestream and normalized on the deficit velocity. The comparison shows that the mean velocities for each wake are nearly equivalent when normalized on their respective length and velocity scales. After this mean flow comparison, a coarse quad-hotwire measurement was performed. Figure 3.21 through Figure 3.24 where the $\overline{u^2}$, $\overline{v^2}$, $\overline{w^2}$ and \overline{uv} stresses are compared for each wake respectively. The $\overline{u^2}$ stress profiles between measurements match the best, and are less than 1% apart. The $\overline{v^2}$ and $\overline{w^2}$ profiles are 1% and 2.5% different respectively. The Reynolds shear stress profile shows the largest discrepancy in the each wake's profile. This is due to the fact that the profile measured in the Open Circuit Wind Tunnel is slightly asymmetric. This asymmetry appears to be a profile specific anomaly since the overall trend for the Reynolds shear stress from each measurement shown in Figure 3.32 is more reasonably symmetric. Methods for accounting this discrepancy will be discussed in later sections. Based on the mean flow and Reynolds stress profile comparisons presented here the wakes measured in each facility found to be acceptably similar. With the wakes measured in each facility judged to be similar, the two-point measurement could commence.

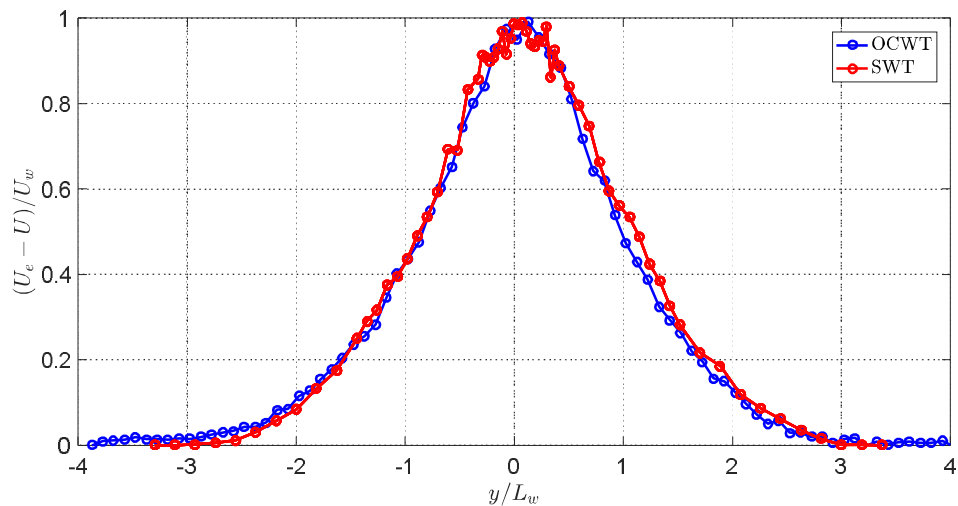


Figure 3.20. Mean flow comparison of the cylinder wakes measured in each facility.

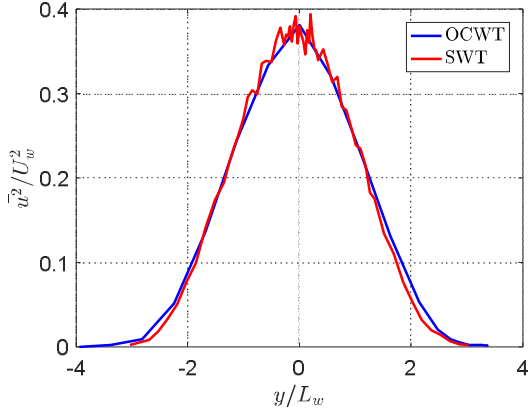


Figure 3.21. $\overline{u^2}$ stress comparisons

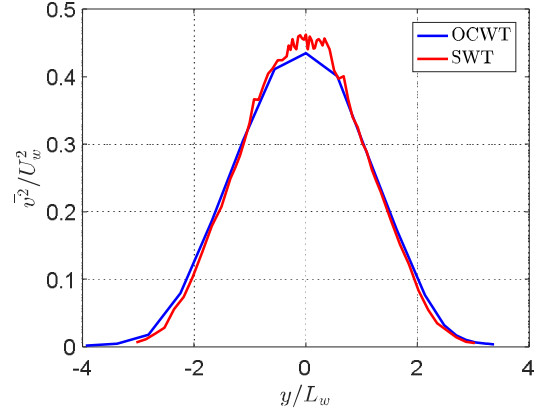


Figure 3.22. $\overline{v^2}$ stress comparisons

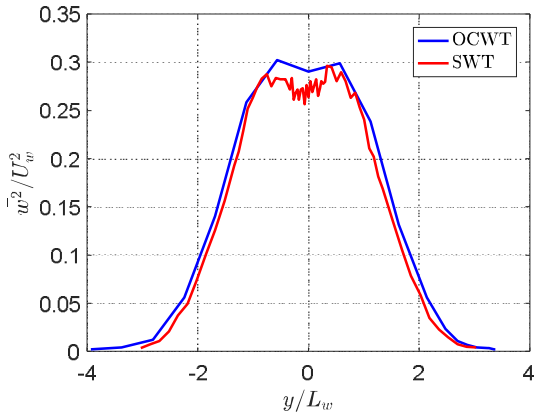


Figure 3.23. $\overline{w^2}$ stress comparisons

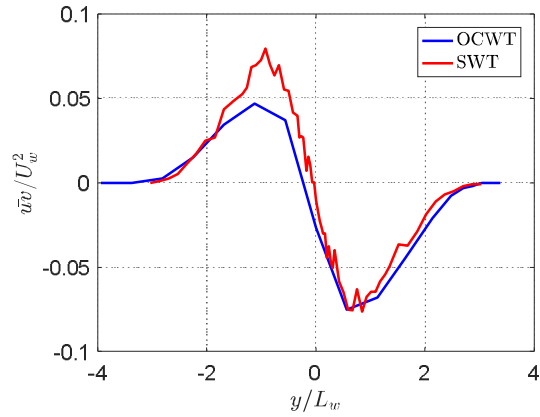


Figure 3.24. \overline{uv} stress comparisons

3.2.3 Description of the Two Point Time Delay Correlation

Before the two-point measurement can be discussed any further, the form of two point correlation must be introduced in the context of the present study. The two-point time delay correlation between velocities is, in general, a seven dimensional function. Each of the two points in the flow has three spatial dimensions associated with it. The seventh dimension is the time delay between points. The correlation tensor is defined as the expected value of the product of two velocity fluctuations as shown in Equation 3.1.

$$R_{ij}(\mathbf{r}, \mathbf{r}', \tau) = \overline{u_i(\mathbf{r}, t)u_j(\mathbf{r}', t')} \quad \text{Equation 3.1}$$

The indices i and j range from 1 to 3 and denote the streamwise, wake-normal and spanwise directions respectively. The position vectors of the two points for which the two-point correlation is desired are given by \mathbf{r} and \mathbf{r}' while the times are given by t and t' . The time delay, τ , is defined as $t - t'$. At zero time delay and zero separation the correlation function tensor is the Reynolds stress tensor given by Equation 3.2,

$$R_{ij}(\mathbf{r}, \mathbf{r}', 0) = \overline{u_i(\mathbf{r}, t)u_j(\mathbf{r}, t)} \quad \text{Equation 3.2}$$

The correlation tensor is also symmetric in the time delay indicated by Equation 3.3.

$$R_{ij}(\mathbf{r}, \mathbf{r}', \tau) = R_{ji}(\mathbf{r}, \mathbf{r}', -\tau) \quad \text{Equation 3.3}$$

In the present study the time delay correlation has been reduced to a four dimensional function by restricting the correlation to the cross sectional plane of the wake and by using the homogeneity of the flow in the spanwise direction. The form of the two-point correlation used by the present study depends on three spatial components and a single temporal one. The two-dimensional moving probe positions are defined by y' and z' while the fixed probe position only changes in a single direction and is defined by y . The z direction is in the $i = j = 3$ direction of the correlation while y and y' are both in the $i = j = 2$ direction. The fixed probe was not positioned at different locations in z due to the homogeneity of the flow in this direction. The z position of the moving probe was defined as the separation between the two probes given by, $\Delta z = z' - z$. The time delay between the signals measured by the two probes is given by τ . The four-dimensional time delay correlation is given by Equation 3.4.

$$R_{ij}(y, y', \Delta z, \tau) = \overline{u_i(y, z, t)u_j(y', z + \Delta z, t + \tau)} \quad \text{Equation 3.4}$$

In practice the two-point velocity correlation function is obtained by computing the inverse Fourier transform of the dual probe cross spectrum computed using a single velocity fluctuation from each probe. This calculation was repeated for each of the nine possible combinations of velocity components between the three velocity fluctuations measured by each probe. Equation 3.5 defines the correlation function R_{ij} in terms of the two-point cross spectral matrix G_{ij} .

$$R_{ij}(y, y', \Delta z, \tau) = \int_0^{\infty} G_{ij}(y, y', \Delta z, \tau, f) e^{2\pi i f \tau} df \quad \text{Equation 3.5}$$

In the case of the NACA 0012 and the present cylinder wake measurements quad-hotwire probes were used to resolve the velocity fluctuations in the three component directions. The airfoil and cylinder two-point measurements were processed identically. The spectral data was stored in 12th octave bands to reduce the size of the data set. The spectra contained data at 114 unequally spaced frequencies from 0 to 25 kHz. The Inverse Fast Fourier Transform was computed using the cross-spectral data between probes at each grid point to determine the time delay correlation between the velocity fluctuation components of the two hotwire probes as shown in Equation 3.5.

3.2.4 Quad-wire Two-Point Grids

After the two-dimensionality of the cylinder wake was documented and the normalized wakes measured in the SWT and OCWT were judged to be similar, the two point measurement began. Before the results from the two-point measurement can be discussed, the measurement approach must be introduced. First, recall the functional form of the two-point time delay correlation given by Equation 3.5. The correlation depends on three spatial coordinates, the y position of the two points and the separation in z between points and the time delay. In the case of the present study and the study performed by Devenport *et al.* (2001) quad-hotwire probes were used to measure the three components of velocity in each flow. For use in acoustic prediction methods, the two-point

time delay correlation must be defined for a full cross section of the flow. To perform this measurement, one hotwire probe was designated the fixed probe while the second probe was designated the moving probe. In the context of the cylinder wake, the fixed probe was positioned at some y location in the wake and at the cylinder spanwise center where $z = 0$. The moving probe was then positioned at many points of y' and z' around the fixed probe. To achieve a minimum distance between the two hotwire probes of 6.35 mm (0.25 in) the fixed and moving probes had to be pitched and yawed so that the probe mounts would not collide with each other during a measurement. The fixed probe was pitched 5.09 degrees up and the moving probe was yawed 11.35 degrees toward the port side of the test section. Miranda (1996) showed that the probe mounts had little effect on the flow.

The full measurement campaign consisted of 19 independent measurements, where each measurement had a unique fixed probe position. The fixed probe was positioned at 19 evenly spaced locations inside the interval, $-3.4 \leq y \leq 3.4$. The moving probe was then traversed in a predefined grid around the fixed probe for positive y' and Δz positions. The moving probe grids were carefully designed for each of the 19 measurements to be as efficient as possible. The correlation data measured in the wake of the NACA 0012 airfoil measured by Devenport *et al.* (2001) was used to determine the moving probe grid locations for the present study. Figure 3.25 shows the R_{22} and R_{23} correlation components in the airfoil wake with the grid points to be used in the present study overlaid on the correlation. The figure shows that the nature of the two-point correlation. The correlation between signals is high when the probes are near each other and the correlation is weak at larger probe separations. This relationship between correlation strength and probe separation allows for the moving probe grid to be unevenly spaced. The grid resolution for small probe separations in y and z (less than 1 half wake width) was dense and became progressively coarser as the separation increased. The figure plots the unevenly spaced moving probe grid for a fixed located at $y = 0$ as blue circles. The figure shows that the region with fine grid spacing is located when the gradient in the correlation is high for separations less than 1 half wake width.

Due to the limitations of the measurement technique used by Devenport *et al.* (2001) to measure the two-point correlation function, correlations were only able to be interpolated to y/L_w and z/L_w positions of 3. In the R_{23} correlation shown it is evident that the measurement range was not quite sufficient. For the present study the measurement range was extended to $3.5 y/L_w$ in the spanwise direction and $4 y/L_w$ in the wake normal direction. In the 19 grid measurements completed in the present study, each measurement required a unique grid. As shown in Figure 3.25, the region of maximum correlation is located near the fixed probe, and thus will be in a different location for each measurement grid with a different fixed probe position. The two-point correlations computed in the airfoil wake were used to verify that grid resolution in each of the 19 grids used in the present study would be adequate.

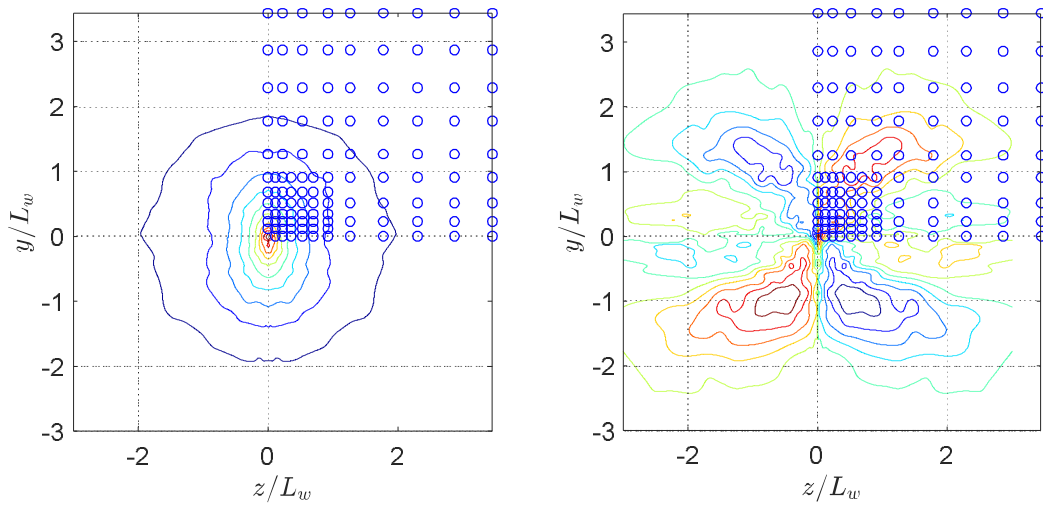


Figure 3.25. R_{22} and R_{23} two-point correlation data in the airfoil wake measured by Devenport *et al.* (2001).

3.2.5 Measurement Consolidation and Symmetry in the Two-Point Correlation

In the full two-point measurement set, the moving probe was only positioned at positive y' and Δz locations, but the fixed probe was positioned on the positive and negative sides of the wake. This required two grids to be combined, to form a single consolidated measurement grid that spanned the full measurement region. Figure 3.26 and Figure 3.27 below show examples of non-uniform grids used for fixed probe positions of 1.53 and -1.53 y/L_w respectively. To consolidate the two measurement grids, the wake flow and the correlation structure were assumed to be symmetric about the line $y = 0$. Using this assumption allowed the measurement grids for negative fixed probe positions to be reflected about the fixed probe. Figure 3.28 shows the consolidated measurement grid using the positive and negative fixed probe grids shown in Figure 3.26 and Figure 3.27. When performing this reflection to effectively define the negative fixed probe grid the sign of the flow variable perpendicular to the wake, v , must be reversed in the stresses and in the correlations since the velocity profile is anti-symmetric. After consolidation the z separations were defined for $0 \leq z/L_w < 3.4$ and the y separations were defined over the range $-4 \leq y/L_w \leq 4$. This consolidation approach was completed for 10 pairs of positive and negative fixed probe grids from the full measurement set. In each case the consolidated correlation data was always associated with the positive fixed probe location. During the consolidation process the two-point correlation was determined by computing the inverse fast Fourier Transform of the cross-spectral matrix between probes at each point in the consolidated grid. After consolidation the two-point correlation was interpolated onto a uniform grid in y , y' , Δz and in time delay for easier manipulation, where y and y' describe the positions of each probe and Δz is the separation between the two probes.

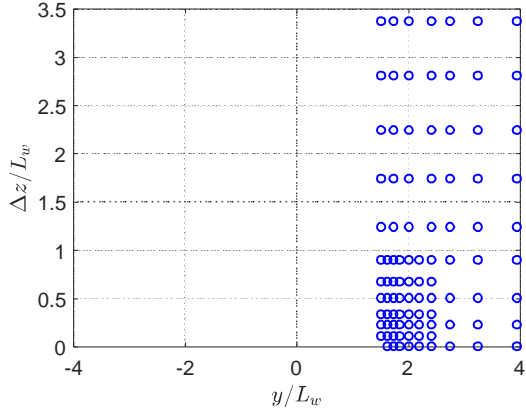


Figure 3.26. The positive fixed probe grid.

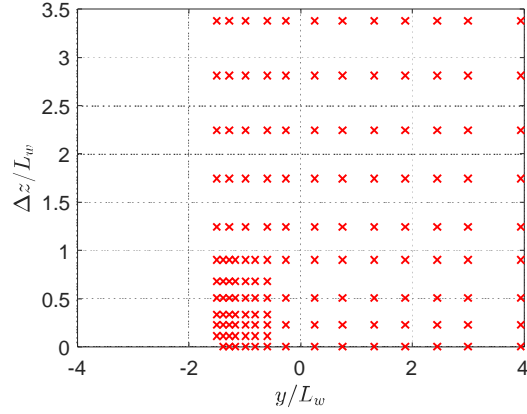


Figure 3.27. The negative fixed probe grid.

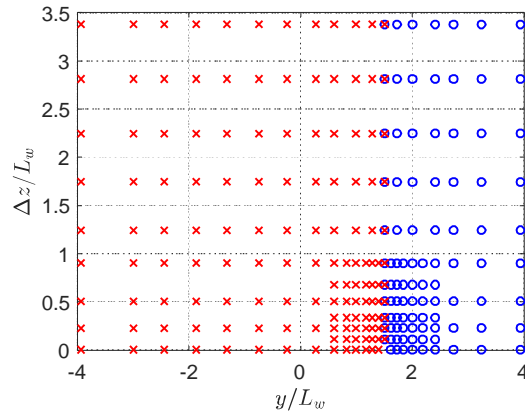


Figure 3.28. The consolidated grid.

After the measurement consolidation was complete, further reduction was required. The full two-point correlation must be defined for positive and negative fixed probe positions between -3.4 and 3.4 . Due to the assumptions made during consolidation, only correlations for positive fixed probe positions were defined. By assuming that the wake is symmetric about the wake centerline, along the line $y = 0$, correlations for negative fixed probe positions can also be determined using a single relationship between the correlations anchored at a positive or negative y location. Since the v velocity is anti-symmetric, this relation must be applied to the R_{12}, R_{21}, R_{23} and R_{32} correlation components. The relation between the correlation components where $i \neq j$ and $i = 2$ or $j = 2$ and y is negative is given by Equation 3. 6 as,

$$R_{ij}(-y, y', \Delta z, \tau) = -R_{ij}(y, y', \Delta z, \tau) \quad \text{Equation 3. 6}$$

A similar condition is enforced for defining the two-point correlation for positive and negative moving probe separations in z . Although only positive separations were measured, by assuming the correlation structure is symmetric about the line $z = 0$ the correlation at negative z separations can be defined. This assumption requires the sign of the correlation to be reversed for the R_{13}, R_{23}, R_{32} and R_{31} correlation components. The symmetry condition where $i \neq j$ and $i = 3$ or $j = 3$ and Δz is negative is given by Equation 3. 7 as,

$$R_{ij}(y, y', -\Delta z, \tau) = -R_{ij}(y, y', \Delta z, \tau) \quad \text{Equation 3.7}$$

The fully reduced four dimensional two-point correlation function is symmetric in z and τ shown in Equation 3.8.

$$R_{ij}(y, y', \Delta z, \tau) = R_{ji}(y', y, -\Delta z, -\tau) \quad \text{Equation 3.8}$$

3.2.6 Initial Two-Point Measurement Results

After each individual grid measurement was complete the Reynolds stress profiles were compared to check the consistency of each measurement. The $\overline{u^2}$, $\overline{v^2}$, $\overline{w^2}$ and \overline{uv} Reynolds stress profiles normalized on the freestream velocity are shown below in Figure 3.29 through Figure 3.32 respectively. Each time the moving probe was positioned at a different Δz separation, a new profile in the y direction was measured by the moving probe. The colors and symbols in the plots below each represent one of the 19 grids measured. In each of the figures there is a noticeable dislocation on the negative half of the profiles. This non-repeatability or shift seen in the wake profiles only effected the last five measurement grids. This error is likely due to an inconsistency in the test section setup where a wall panel or a corner fillet in the test section changed before the last five measurements were completed. This could have caused the wake to shift inside the test section. A second possibility is that a physical misalignment was introduced into the traverse system where each position was then offset by some amount. These two factors are responsible for the apparent misalignment in some of the measurement grids. In the $\overline{v^2}$ and $\overline{w^2}$ Reynolds stresses the negative side of the wake fails to reach zero as it should.

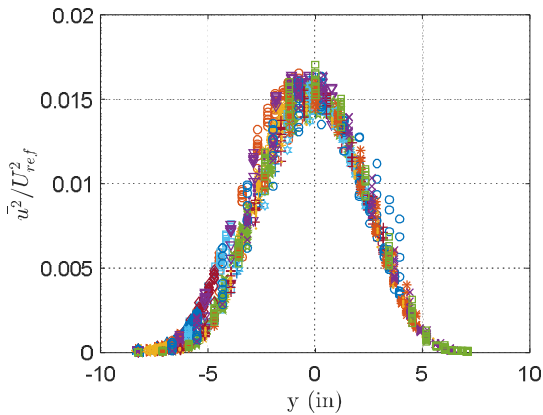


Figure 3.29. Extracted CJWT $\overline{u^2}$ wake profiles.

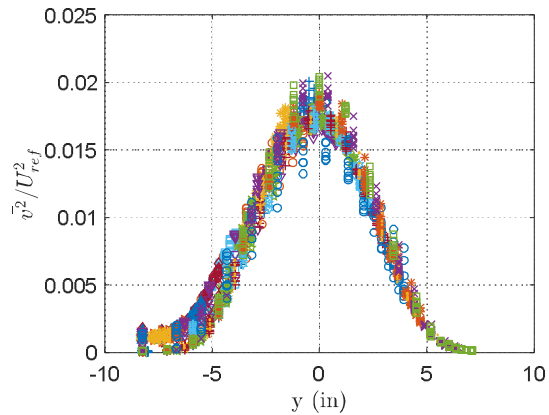


Figure 3.30. Extracted CJWT $\overline{v^2}$ wake profiles.

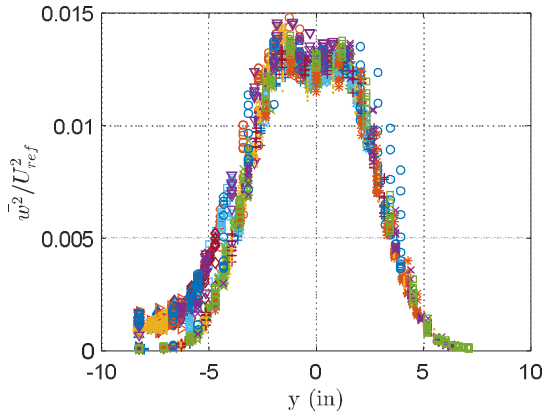


Figure 3.31. Extracted CJWT $\overline{w^2}$ wake profiles

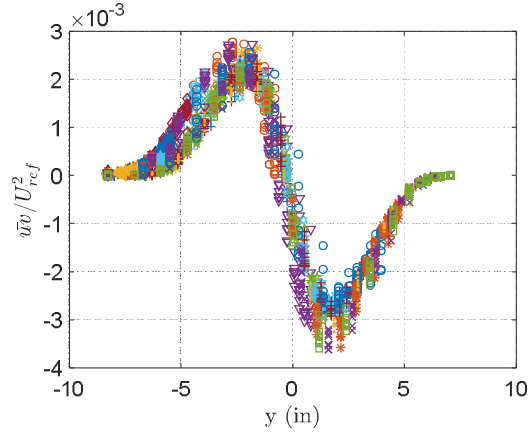


Figure 3.32. Extracted CJWT \overline{uv} wake profiles

3.2.7 Shifting the Measurement Grid Data

Recall Figure 3.20 through Figure 3.24 where the velocity and Reynolds stress profiles measured in both facilities were similar. The agreement seen between the normalized Reynolds stress profiles measured in the Open Circuit and Stability Wind Tunnel gave confidence that the data measured in the full test campaign could be corrected for the inconsistencies seen. Applying a shift to the measurement data from the affected grids measured Open Circuit facility in y would adequately correct for the offsets seen in the full data set. To perform this shift, Gaussian curves were fit the $\overline{u^2}$ Reynolds stress profiles. Each of the affected grid measurements had a single shift associated with it. The shifts were computed by aligning the point where the profiles passed through half of their maximum value. Figure 3.33 through Figure 3.36 below show the shifted $\overline{u^2}$, $\overline{v^2}$, $\overline{w^2}$ and \overline{uv} Reynolds stress profiles respectively. After the profiles were shifted the data was interpolated back onto the original grid points such that the spatial resolution of the data was unaffected. The figures show that the wake shifting does help with the dislocations previously seen on the port side of the wake in each of the Reynolds stresses. Unfortunately the failure of the y and z to reach zero on the port side of the wake is not resolved after the shifting method was applied. The shifting and interpolation process also somewhat helps the variation seen in each of individual profiles. In addition to the Reynolds stresses the cross-correlation profiles, cross-spectral matrices of the moving and fixed probes and the cross-spectral matrix computed between the moving and fixed probes were also shifted and interpolated back to the original grid locations.

To investigate the behavior certain wake profiles where the $\overline{v^2}$ and $\overline{w^2}$ Reynolds stress values fail to reach zero on the negative side of the wake, the RMS voltage of each of the four sensors on the moving probe was computed. Figure 3.37 plots the RMS voltages computed at each grid point in a single grid measurement where the moving probe was traversed over nearly half of the wake. The important feature to note in this figure is that none of the four sensor voltages reach to zero at the negative edge of the wake. Even without the velocity calibration applied, the voltages should reach zero when the moving probe is outside of the wake. Figure 3.38 shows the RMS voltages for each sensor on the moving probe for the 19th measurement grid where the moving probe measured nearly the entire wake. In this measurement grid the RMS voltages near the negative side of the wake are closer to zero than for RMS voltages shown Figure 3.37. This behavior also

suggests that there was some inconsistency in test setup between measurement grids. The cause for this behavior in the $\overline{w^2}$ and $\overline{v^2}$ Reynolds stresses is likely due to the fact that the alignment of the test section wall panel on the port side of the slightly changed or the corner fillets inside the test section changed for the last five measurement grids.

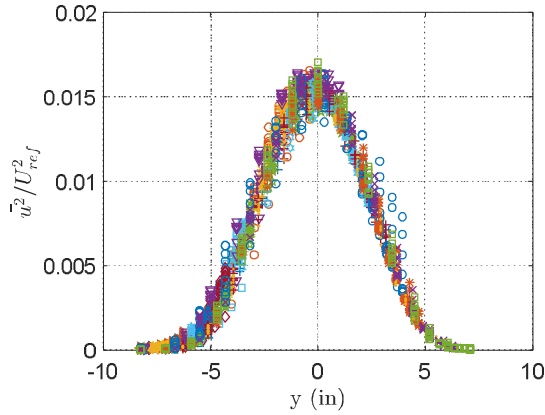


Figure 3.33. Shifted CJWT u^2 wake profiles.

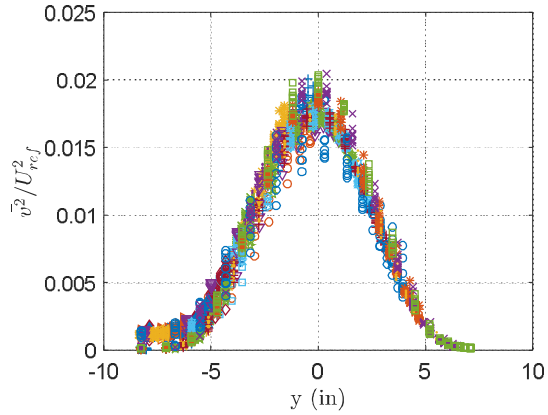


Figure 3.34. Extracted CJWT v^2 wake profiles.

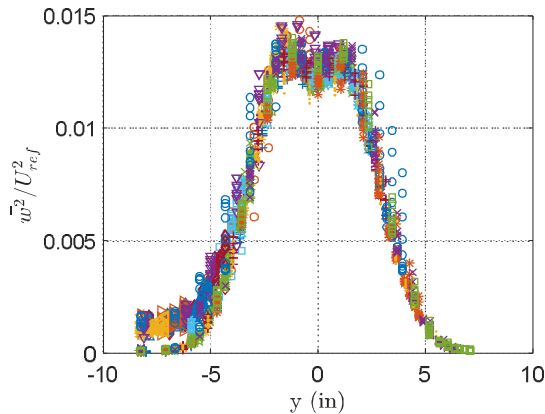


Figure 3.35. Extracted CJWT w^2 wake profiles.

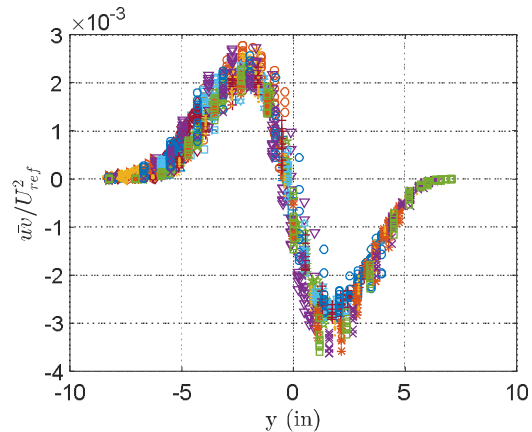


Figure 3.36. Extracted CJWT uv wake profiles.

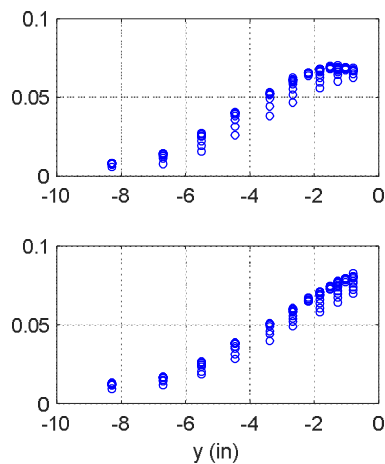
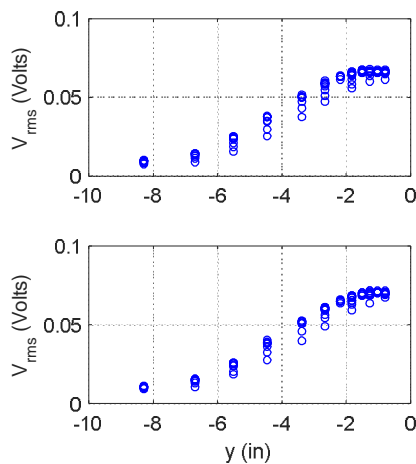


Figure 3.37. Grid 2 RMS voltages.

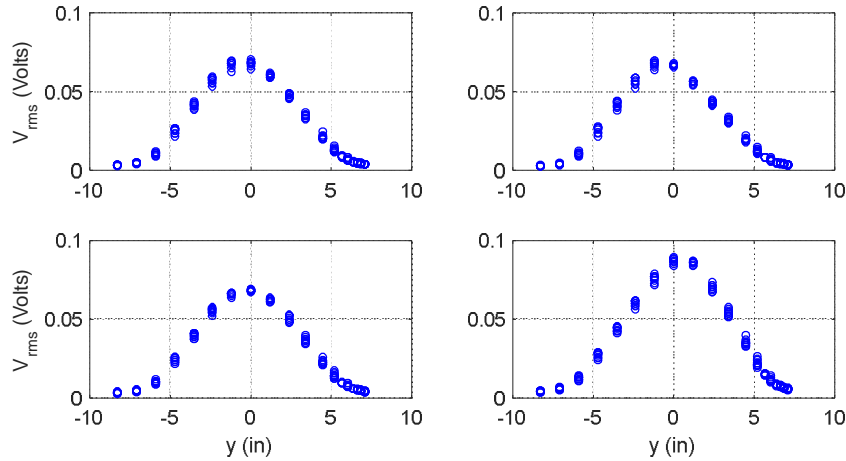


Figure 3.38. Grid 19 RMS voltages.

3.2.8 Correction for the Angle Sensitivity of the Hotwire Probes

The probe positioning required to achieve the desired minimum probe separation in the y' and Δz variables introduced extra error into the velocities measured during the two-point measurement. The fixed probe was pitched 5.09 degrees up and the moving probe was yawed 11.35 toward the port side of the test section. This extra error arises when determining the correction needed to resolve the true flow velocities using the angle calibration. As discussed in Section 2.3.3, the angle calibration defines the error in the measured velocity components for any probe pitch and yaw angle within ± 45 degrees. Figure 3.39 shows the error in the quad-hotwire measured v velocity as a percentage of the freestream velocity during calibration for pitch and yaw angles ranging from -45 to 45 degrees. The structure of the error contour is such that at zero probe pitch and yaw, the error in the v velocity is very near zero. As the probe pitch or yaw angle changes, the error in v velocity begins to change rapidly. The angle calibration is ultimately computed by fitting a surface to the velocity errors shown in Figure 3.39. Since the cylinder wake flow is unidirectional, only a single point on the calibration surface is used to correct the measured velocity at a single measurement point. When the probe pitch and yaw is large, the measurement is located at a point on the calibration surface where the gradient of the error is steep. In areas with a steep gradient in the velocity errors, the uncertainty in the surface fit is greater than for points that do not lie on such a steep gradient. This added uncertainty in the surface fit causes the velocity components corrected using the angle calibration to resolve the velocity components with some added error. This error due to the measurement location on the angle calibration surface does not affect the measured mean flow, but does influence the Reynolds stresses.

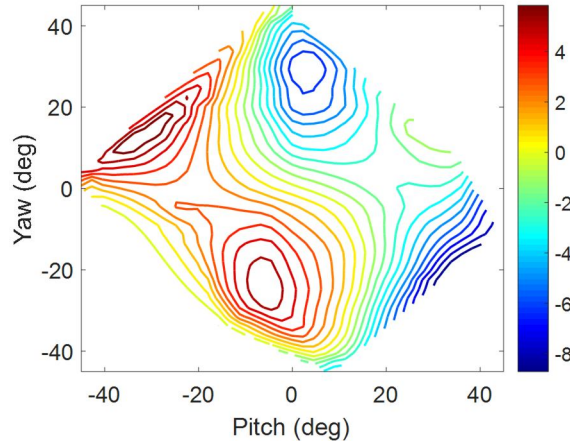


Figure 3.39. The error in the quad-hotwire measured v velocity.

In the Stability Wind Tunnel wake measurements the hotwire probes used were never misaligned with the flow due to the nature of the single point wake profile measurements. This error due to the probe positioning in the Open Circuit facility could therefore be reduced by using the wake data measured when the probes were aligned in the Stability Wind Tunnel to correct for the error in the angle calibration surface fit. The cylinder wake mean streamwise velocities scaled on the deficit velocity and half wake width measured in the two facilities match closely shown above in Figure 3.20. The Reynolds stress profiles also nearly matched as shown in Figure 3.21 through Figure 3.24. This agreement in the profiles measured in each facility makes it reasonable to use the profiles measured when the probes were aligned with the freestream to correct the profiles measured when the probes angled in the two-point measurement. A linear correction matrix was computed using the Reynolds stress profiles measured when the hotwire probes were aligned and misaligned with the freestream. This correction matrix was computed for each individual grid by minimizing the error between the stress profiles using the method previously developed by Borgoltz (2007). Equation 3.9 below relates the transformed fluctuating components of velocity to the measured fluctuating components through the correction matrix T .

$$\begin{Bmatrix} u'_T \\ v'_T \\ w'_T \end{Bmatrix} = \begin{bmatrix} T_{11} & T_{12} & T_{13} \\ T_{21} & T_{22} & T_{23} \\ T_{31} & T_{32} & T_{33} \end{bmatrix} \begin{Bmatrix} u' \\ v' \\ w' \end{Bmatrix} \quad \text{Equation 3.9}$$

Equation 3.10 below shows a typical transformation matrix corresponding to the grid anchored at $y/L_w = -3.44$. For this grid the moving probe was traversed nearly the entire width of the wake. The correction is within a few percent of identity, indicating that the errors between the slopes on the calibration surface of the probe was not largely different in both measurements.

$$\begin{Bmatrix} u'_T \\ v'_T \\ w'_T \end{Bmatrix} = \begin{bmatrix} 1.0308 & 0.0026 & 0.0242 \\ -0.0036 & 0.9853 & 0.0264 \\ 0.0298 & 0.0561 & 1.0292 \end{bmatrix} \begin{Bmatrix} u' \\ v' \\ w' \end{Bmatrix} \quad \text{Equation 3.10}$$

The figures that show the profiles before and after transformation are shown in Appendix A. Figure and Figure show the normal and cross Reynolds stresses from the moving probe before transformation respectively while Figure and Figure show the transformed stress profiles. In each figure the solid black lines represents the Stability Wind Tunnel wake profiles normalized on the half wake width and maximum deficit velocity. After transformation the profiles show stronger agreement. Fixed probe profiles can also be generated since the probe was positioned throughout the entire wake. Figure and Figure show the fixed probe normal and shear Reynolds stress profiles respectively before transformation. Figure and Figure show the transformed fixed probe Reynolds stress profiles. There is again stronger agreement after transformation.

Now that shifting and transformation methods have been developed and applied to each measurement grid, the turbulence data from the Open Circuit Wind Tunnel measurements can be expressed in its final form. Figure 3.40 through Figure 3.43 show the $\overline{u^2}$, $\overline{v^2}$, $\overline{w^2}$ and \overline{uv} Reynolds stress profiles respectively after the shifting and transformation corrections have been applied. In each figure each grid point from each of the nineteen measurement grids are plotted. The variation in profiles is further reduced after the transformation is applied. The same correction has been applied to the cross spectral matrices computed using the moving and fixed probes and the cross-spectral matrix computed between probes. Since the two-point correlation is computed using the cross-spectral matrix, the correlation will also be corrected for the errors due to probe alignment. The Reynolds stress profiles measured at the cylinder midspan were also corrected to ensure that there was still good agreement between the profiles measured in each facility. In Figure 3.44 through Figure 3.47 the transformed profiles are compared with the profiles measured in the Stability Wind Tunnel. These comparisons show that there is still good agreement between profiles and that the correction process did not drastically alter the Reynolds stress profiles.

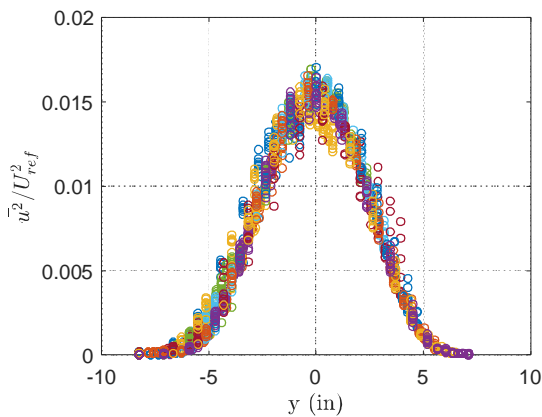


Figure 3.40. Transformed $\overline{u^2}$ Reynolds stress

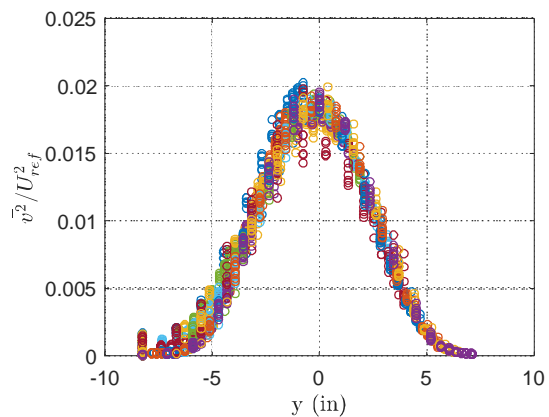


Figure 3.41. Transformed $\overline{v^2}$ Reynolds stress profiles

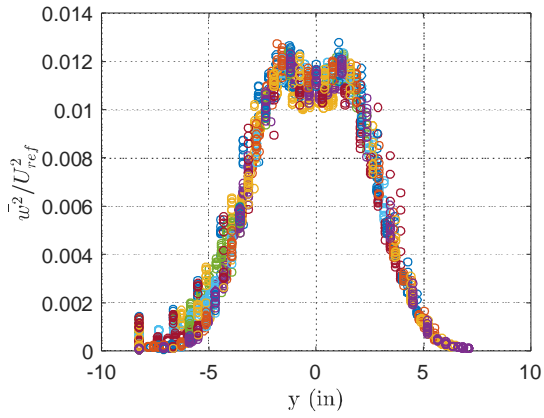


Figure 3.42. Transformed \bar{w}^2 Reynolds stress profiles

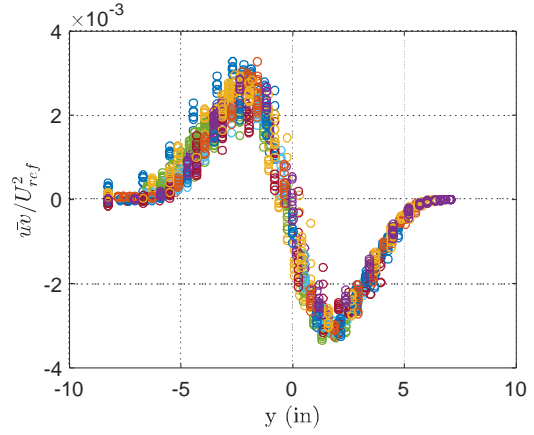


Figure 3.43. Transformed \bar{uv} , \bar{vw} and \bar{uw} Reynolds stress

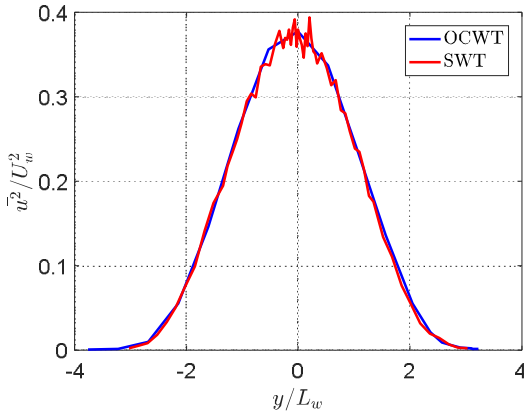


Figure 3.44. Transformed \bar{u}^2 Reynolds stress profile comparison.

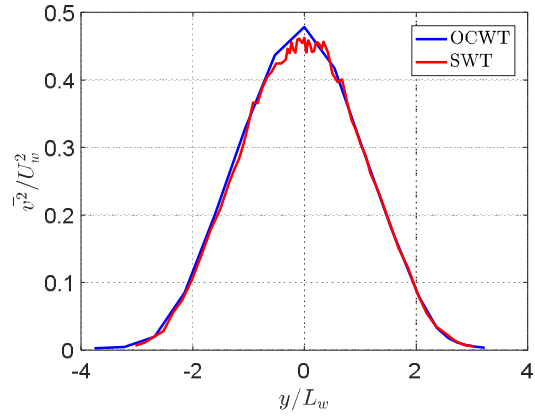


Figure 3.45. Transformed \bar{v}^2 Reynolds stress profile comparison.

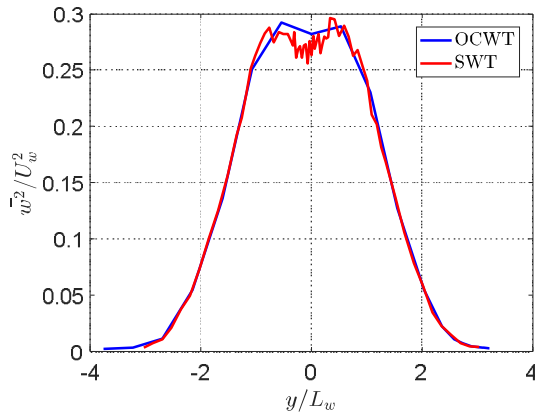


Figure 3.46. Transformed \bar{w}^2 Reynolds stress profile comparison.

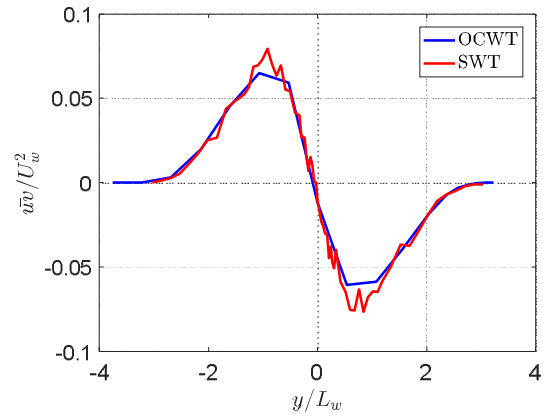


Figure 3.47. Transformed \bar{uv} Reynolds stress profile comparison.

3.2.9 Hotwire Probe Coherence

Before computing the two-point correlation the coherence spectra was computed at several points across separate measurement grids to ensure that strong correlation between probe signals was present when expected. To examine the coherence two individual points in the measurement grid for a fixed probe located at $1.5 y/L_w$ were chosen. Figure 3.48 shows the measurement point chosen to compute the coherence. The moving probe is 0.25 inches in z from the fixed probe and at zero separation in y . With such close spacing between probes the coherence between signals should be high and the energy in the spectra should be nearly identical, especially at low frequencies. In this study the spectra have been binned into 12th octave bands to limit the size of the data in the reduction process. Figure 3.49 compares the autospectra from the fixed and moving probes for each component of fluctuating velocity at the probe locations shown in Figure 3.48. These spectra were computed up to 20 kHz where the high frequency content begins to be aliased. The spectra are nearly identical until high frequencies where the responses of the two systems begin to differ slightly. Figure 3.50 shows the coherence computed between probes for each fluctuating velocity component. There is high coherence is seen at low frequencies. The cylinder shedding frequency of 136.5 Hz is marked with a dotted line, where there is a peak in the coherence spectra. Figure 3.51 shows a second fixed-moving probe location pair where the moving probe is now displaced 1.5 inches in z from the fixed probe. Figure 3.52 compares the autospectra at this new spacing where strong agreement is seen again. Figure 3.53 shows the coherence spectra for the wider separation of 1.5 inches. There are again clear peaks in the coherence spectra located at the cylinder shedding frequency that are more defined than in the previous case since the overall coherence is lower due to the larger probe separation. This shedding frequency implies a Strouhal number of 0.196 which is within 3% of the Strouhal number observed in the SWT measurements.

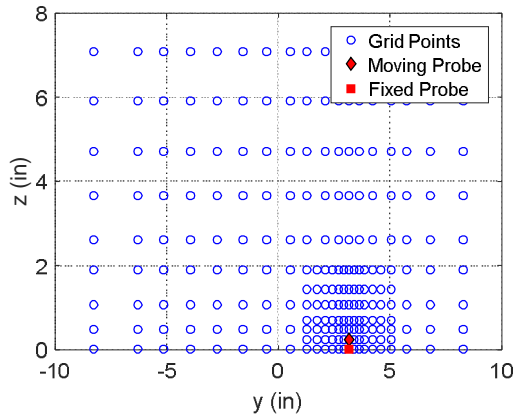


Figure 3.48. Fixed and moving probe locations.

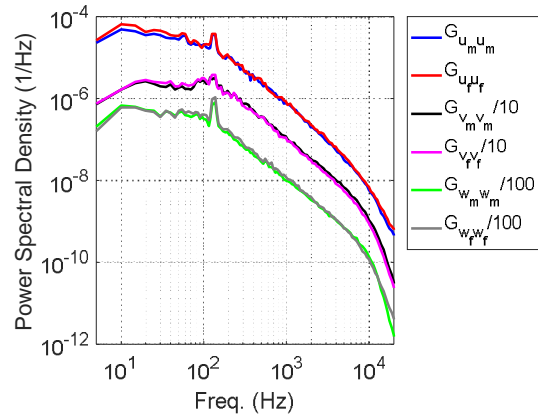


Figure 3.49. Fixed and moving probe autospectra at the probe locations shown in Figure 3.48

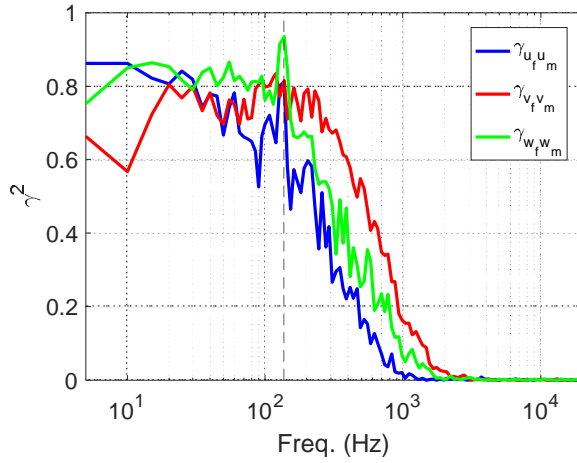


Figure 3.50. Coherence spectra at the probe locations shown in Figure 3.48

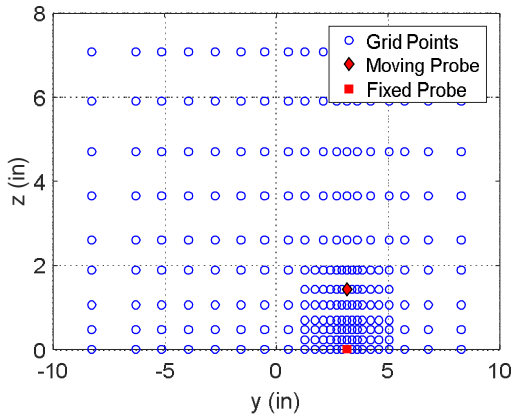


Figure 3.51. Fixed and moving probe locations

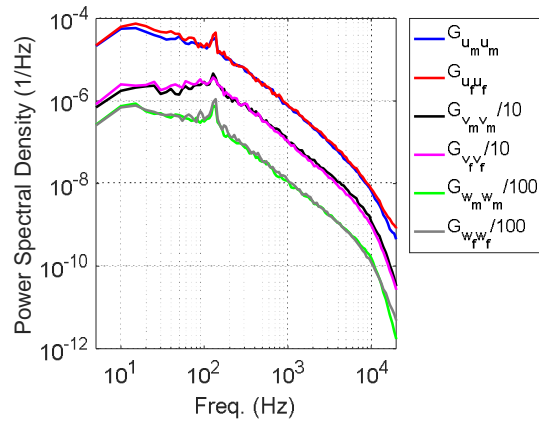


Figure 3.52. Fixed and moving probe autospectra at the probe locations shown in Figure 3.51

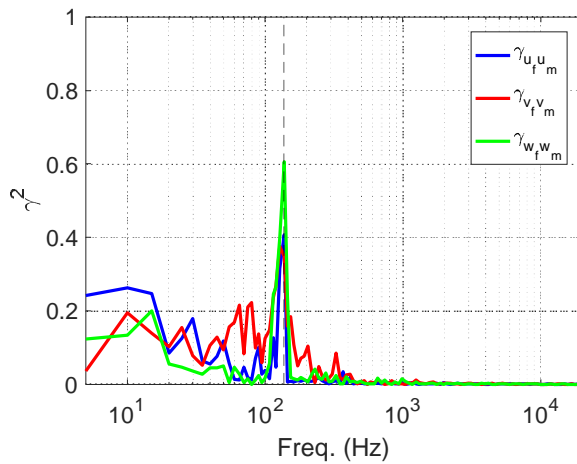


Figure 3.53. Coherence spectra at the probe locations shown in Figure 3.51.

3.2.10 The Cylinder Wake Two-Point Correlation

After the measurement consolidation procedure discussed in Section 3.2.5 was complete, the two-point correlation function was organized into a single Matlab data file. In Appendix A the format of this data file and the Matlab code use to access the two-point correlation data in the cylinder wake is presented and described. As shown in Section 3.2.4 the measurement grids were all independently generated, and irregularly spaced. The ultimate goal is to have the correlation function be used as the boundary condition in the larger study investigating the turbulence ingestion problem. In order to be effectively used the data must be easily plotted for a range of conditions. The nature of the measurement grids made the manipulation of data slow and cumbersome. The measurement grids were first consolidated according to the procedure outlined in Section 3.2.4 and then interpolated onto an even grid in y and z with a resolution of $0.018 y/L_w$. During the consolidation and interpolation process the data was constantly checked to ensure that the interpolated data set was not altered from the original set. After the full interpolation and reduction methods were complete, the data could be plotted for any fixed probe located in the range $-3.4 < y/L_w < 3.4$ and time delay in the range $-8 < \tau U_e/L_w < 8$.

With the correlation function in its final form and easily accessed in a Matlab function, a calculation was performed to verify that the two-point correlation satisfied conservation of mass. Each of the nine components of the correlation tensor were differentiated in the x , y and z directions. Equation 3.11 shows that for mass to be conserved in the correlation function the partial derivatives of R_{ij} in each component direction must sum to zero.

$$\frac{\partial R_{ij}}{\partial x'} + \frac{\partial R_{ij}}{\partial y'} + \frac{\partial R_{ij}}{\partial z'} = 0 \quad \text{Equation 3.11}$$

The derivatives in the y and z directions were well defined by the measurement technique. The derivative in the x direction however required an additional relationship since the correlation was function was only physically measured in the cross sectional plane. Taylor's hypothesis states that considering the derivative a greater positive time delay in the flow is equivalent to considering the derivative of a greater negative separation in x between two points in the time delay correlation. The partial derivative in the x direction is therefore equivalent to the negative of the partial derivative with respect to time delay as shown in Equation 3.12.

$$\frac{\partial R_{ij}}{\partial x'} = -\frac{\partial R_{ij}}{\partial \tau} \frac{1}{U_{ref}} \quad \text{Equation 3.12}$$

The criteria used to judge that mass was conserved in the correlation function is shown in Equation 3.13. The sum of the partial derivatives was normalized by the sum of the squares of the derivatives. This criteria was computed for each point in the measurement cross section. This criteria was checked for several fixed probe locations, and in each case the criteria was near zero and was less than 1%. This is significant because it serves to validate the entire measurement and data reduction process.

$$\left(\frac{\partial R_{ij}}{\partial x'} + \frac{\partial R_{ij}}{\partial y'} + \frac{\partial R_{ij}}{\partial z'} \right) / \left(\frac{\partial R_{ij}}{\partial x'}^2 + \frac{\partial R_{ij}}{\partial y'}^2 + \frac{\partial R_{ij}}{\partial z'}^2 \right)^{1/2} = 0 \quad \text{Equation 3.13}$$

With correlation function reduction process verified, the two point correlations can be plotted for any condition. Figure 3.54 and Figure 3.55 present the wake correlation tensor for a fixed probe located at $y/L_w = 1$ for the normal and cross correlations respectively. These cross sections and those that follow have all been measured twenty diameters downstream of the cylinder. This position was chosen due to the significance of the half wake width in the classic wake normalizations. In these figures the wake is presented horizontally with the wake-normal coordinate plotted on the y axis. The contour levels correspond to the two-point correlation value and have been normalized on the deficit velocity squared.

The normal correlations in each velocity component show a peak of high correlation when the probe separations are less than 0.25 in the normalized coordinates. After this range the correlation begins to decrease in magnitude until the probe separation is large enough where the correlation between probes is zero. The correlation between the v velocity components shows that the correlation is skewed to the negative side of the wake. This is due to the fact that the moving probe is traversed over a large portion of the wake where large structures are being shed by the cylinder. The cross correlations show a similar trend in the correlation between the u and v components of velocity. The R_{12} and R_{21} correlations show a negative correlation with a maximum value when the probes are near each other and decreases in magnitude until the correlations reaches zero. The remaining correlation components each show antisymmetric distributions about the wake centerline and cylinder mid-span. This character is due to the shedding nature of the cylinder wake, where the cylinder wake sheds vortices with alternating signs as defined as the von Karman vortex street. More analysis on the structure of the two-point correlation is presented in Section 3.3.3 where the correlations are compared with the correlations in the airfoil wake.

The reduced data set in its compact form only contains the correlation data for positive fixed probe positions. By assuming that the wake is symmetric correlations for negative fixed probe locations can also be plotted as described in Section 3.2.5. Figure 3.56 shows the R_{23} two point correlation component for fixed probe locations at $y/L_w = \pm 1$. The enforcement of the symmetry condition is seen here where the correlation for the negative fixed probe position is the inverted form of the correlation for the positive fixed probe correlation. Since the anchor point for the correlation is now on the port side of the wake the sign of the correlation must be reversed since the wake-normal velocity component is anti-symmetric about the wake centerline.

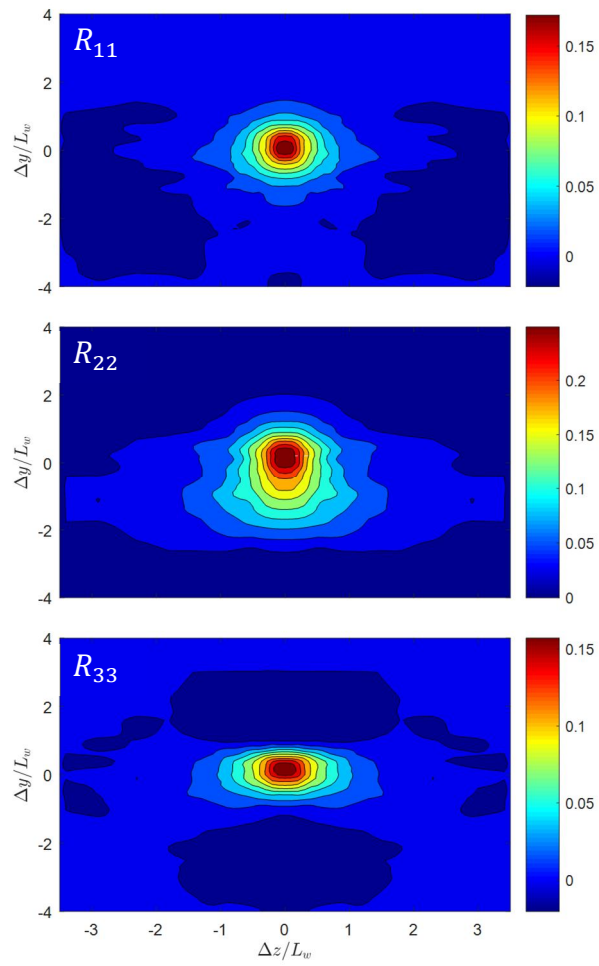


Figure 3.54. Cylinder wake correlation for a fixed probe location of $y/L_w = 1$

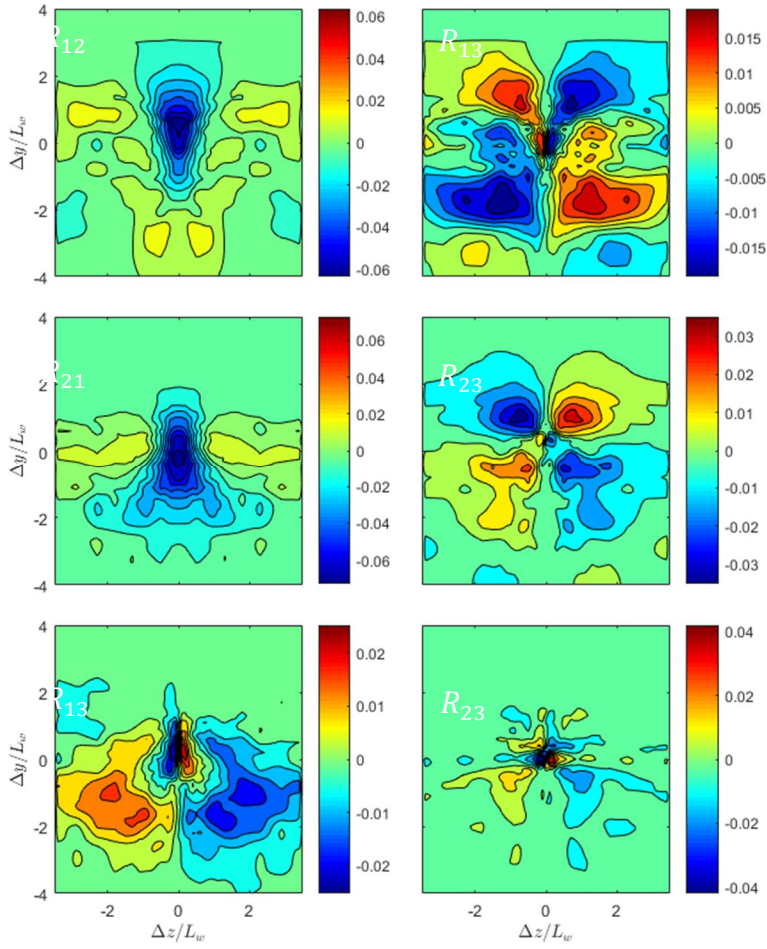


Figure 3.55. Cylinder wake correlation for a fixed probe location of $y/L_w = 1$

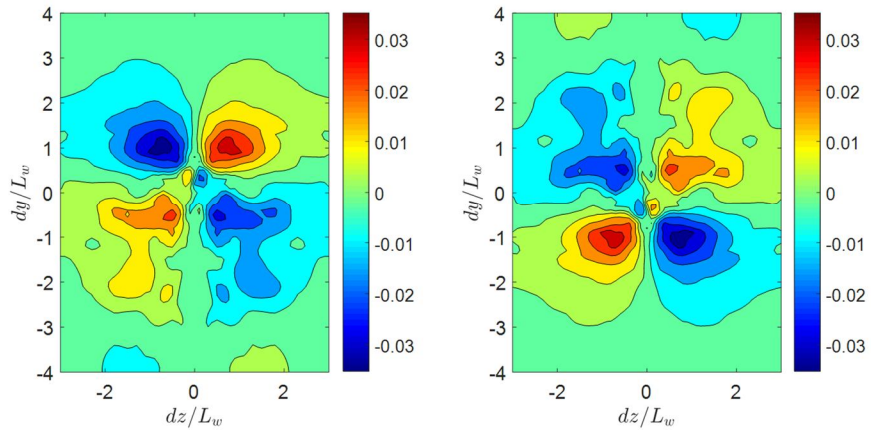


Figure 3.56. Correlation figures for the R_{23} correlation component for a fixed probe location of $y/L_w = 1$ (left) and $y/L_w = -1$ (right).

3.2.11 Cylinder Wake Proper Orthogonal Decomposition

The formulation used to compute the proper orthogonal modes for the airfoil wake and cylinder wake correlation data was introduced in Section 1.3.2. POD serves as the method for characterizing the organization of coherent structures based on the modes computed using the two-point correlation tensor. This characterization of turbulent structures is not possible by only examining the two-point velocity correlations. Both one-component and three-component POD analyses were completed using the two-point time delay correlation for zero separation in z .

3.2.11.1 Cylinder Wake One Component Proper Orthogonal Decomposition

A one dimensional decomposition calculation is easily carried out. The orthogonal modes and eigenvalues corresponding to the energy in each mode are the eigenvectors and eigenvalues respectively computed using the zero time delay and zero-separation two-point correlation in a single direction, that is R_{11} , R_{22} or R_{33} , which was measured twenty diameters downstream of the cylinder. The correlation between the i and j velocity components for the fixed and moving probes respectively is defined as, $R_{ij}(y, y', 0, 0) = \overline{u_i(y, 0, 0)u_j(y', 0, 0)}$ for a correlation computed using the streamwise velocities from each probe. This formulation is related to Equation 1.5, however in the case of zero time delay and zero separation in the z direction the formulation is defined by Equation 3.14.

$$\int R_{ij}(y, y', 0, 0)\phi_j(y')dy' = \lambda\phi_i(y) \quad \text{Equation 3.14}$$

Figure 3.57 plots the eigenvalues and relative energy of the first 20 modes using the R_{11} , R_{22} and R_{33} zero-separation correlation components respectively. In the u and v directions the first mode accounts for about 50% of the total energy while in the w direction the first mode accounts for only 21% of the total energy. The modal profiles for the first four modes are shown in Figure 3.58 through Figure 3.61. The velocity profiles are plotted against the wake-normal variable normalized on the half wake width. These profiles represent the optimum modal velocity profiles for each component. For the first four modes the profiles in each direction are similar for each velocity component, and no one component appears to dominate. In the first two modes the velocity profiles show symmetric and antisymmetric profiles which associate them with the generation of the Reynolds stresses. The third and fourth modal profiles appear to show more complex profile shapes.

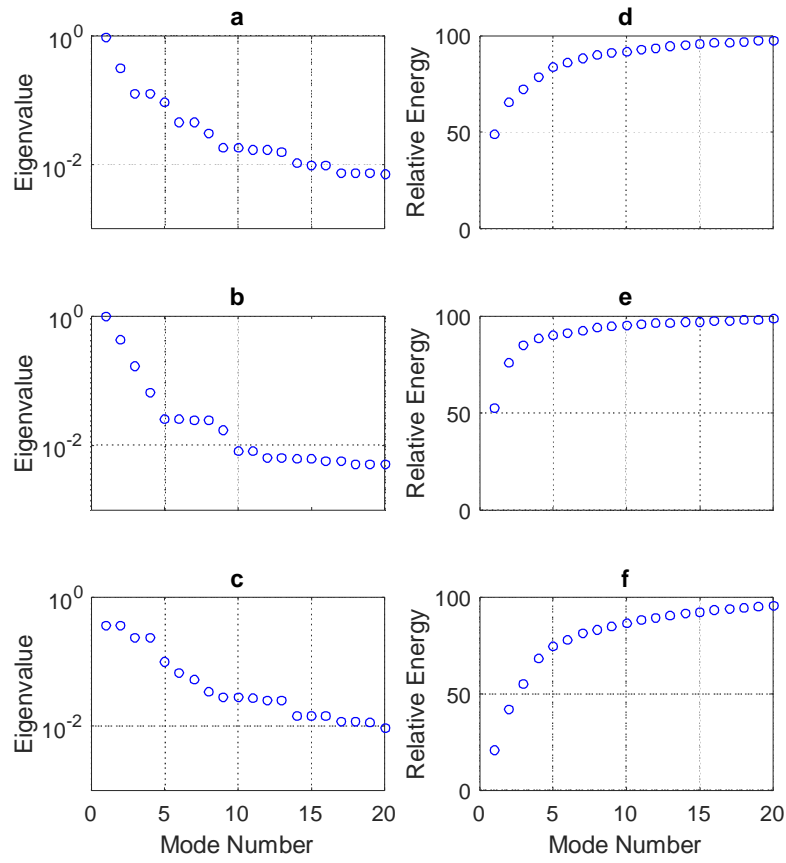


Figure 3.57. Modal profiles and relative energy for the first twenty modes in the streamwise (a)(d), wake normal (b)(e) and spanwise (c)(f) directions.

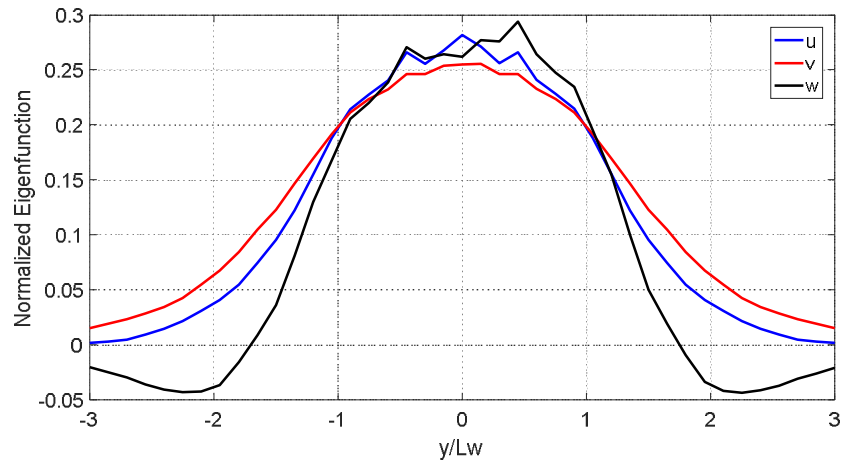


Figure 3.58. Modal velocity profiles for the first mode.

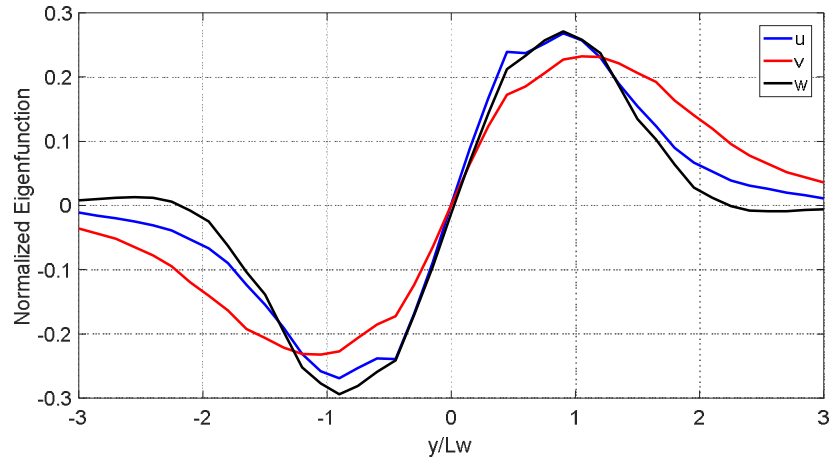


Figure 3.59. Modal velocity profiles for the second mode.

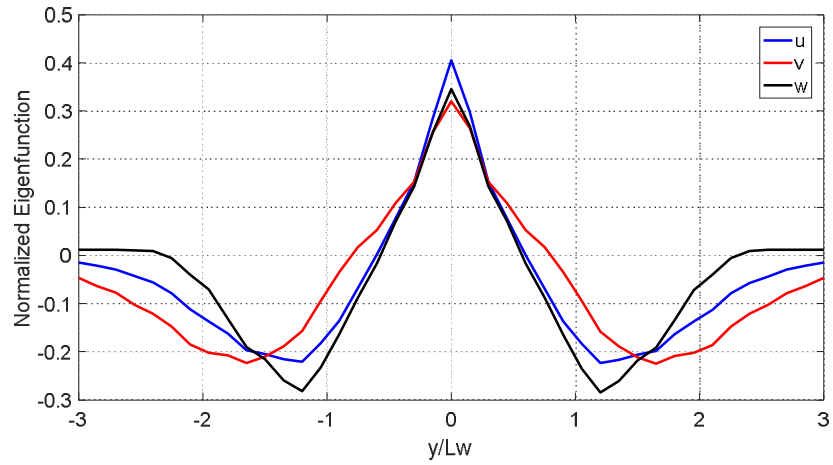


Figure 3.60. Modal velocity profiles for the third mode.

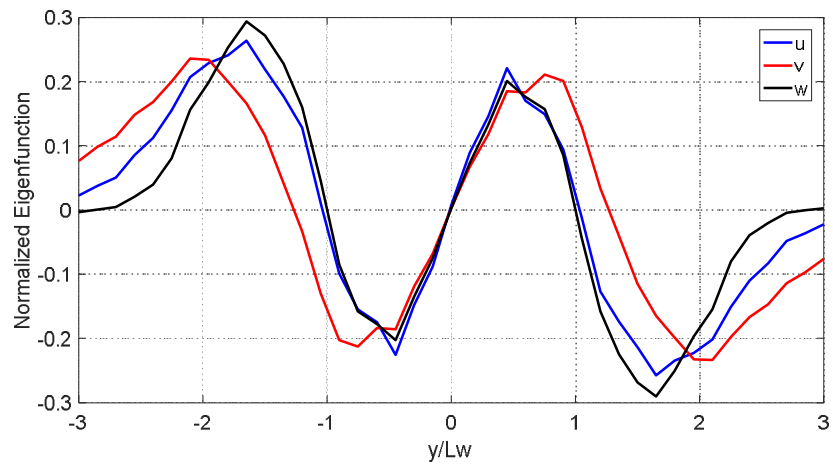


Figure 3.61. Modal velocity profiles for the fourth mode.

3.2.11.2 Cylinder Wake Three Component Proper Orthogonal Decomposition

The three component proper orthogonal decomposition is more complicated since the three correlation components in a single coordinate direction must be considered. For example, a three component analysis in the v velocity direction requires the eigenvectors and eigenvalues to be computed using the R_{21} , R_{22} and R_{23} correlation components. To compute the orthogonal modes the zero separation time delay correlation must be computed for all nine two-point correlation tensor components. The correlation is a function of y , y' , z and τ as shown in Equation 3.15. In the case of zero separation the moving and fixed probes are located at the same position in z where $z' = z$. In the case of the present study, the fixed probe was always located at $z = 0$.

$$R_{ij}(y, y', 0, \tau) = \overline{u_i(y, 0, t)u_j(y', 0, t + \tau)} \quad \text{Equation 3.15}$$

Figure 3.62 plots this correlation at zero z probe separation. The correlations were computed for y and y' normalized separations from -3 to 3 . The correlations were organized into a matrix such that the proper orthogonal modes could be computed in the three velocity component directions. Since the three correlation components in a single coordinate direction are considered in determining the mode, there is inherently more information in the resulting profiles than in the one-dimensional analysis. Figure 3.62 shows that the only dominating cross correlation is the R_{12} and R_{21} components. This is due to the Reynolds shear stress term, which is the dominant shear stress in the wake of a cylinder. Figure 3.63 plots the eigenvalue spectrum for the first twenty modes, in the wake-normal direction. As seen before, the first mode dominates and contains 53.8% of the total energy. The first 10 modes contain 97.1% of the total energy of the 41 modes computed. Figure 3.64 plots the modal profiles for the first six modes computed for the cylinder wake. Unlike the one-dimensional case the velocity profiles for the first six modes are different in each velocity component direction. They are however closely related since they are all part of the same modal profile. The modes appear to be associated with the generation of Reynolds stress since they combine symmetric and antisymmetric u and v modes. Note that there is no contribution from the w velocity component in the first three modes. In the fourth mode there is a symmetric w profile while the u and v profiles are near zero. The fact that large amplitude w profiles don't appear alongside large amplitude u and v profiles reflects the fact that the R_{32} and R_{31} are almost zero.

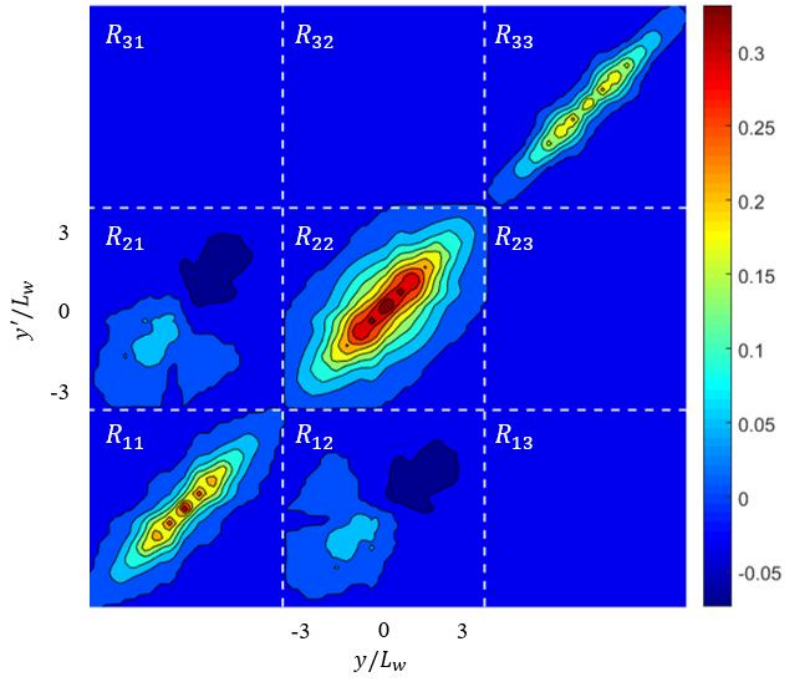


Figure 3.62. Zero separation correlation at zero time delay.

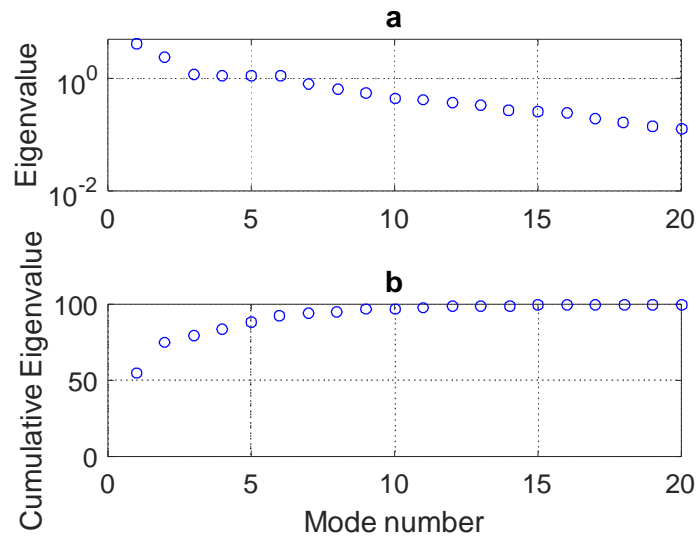


Figure 3.63. Cumulative eigenvalue spectrum for the first 20 modes in the wake normal direction.

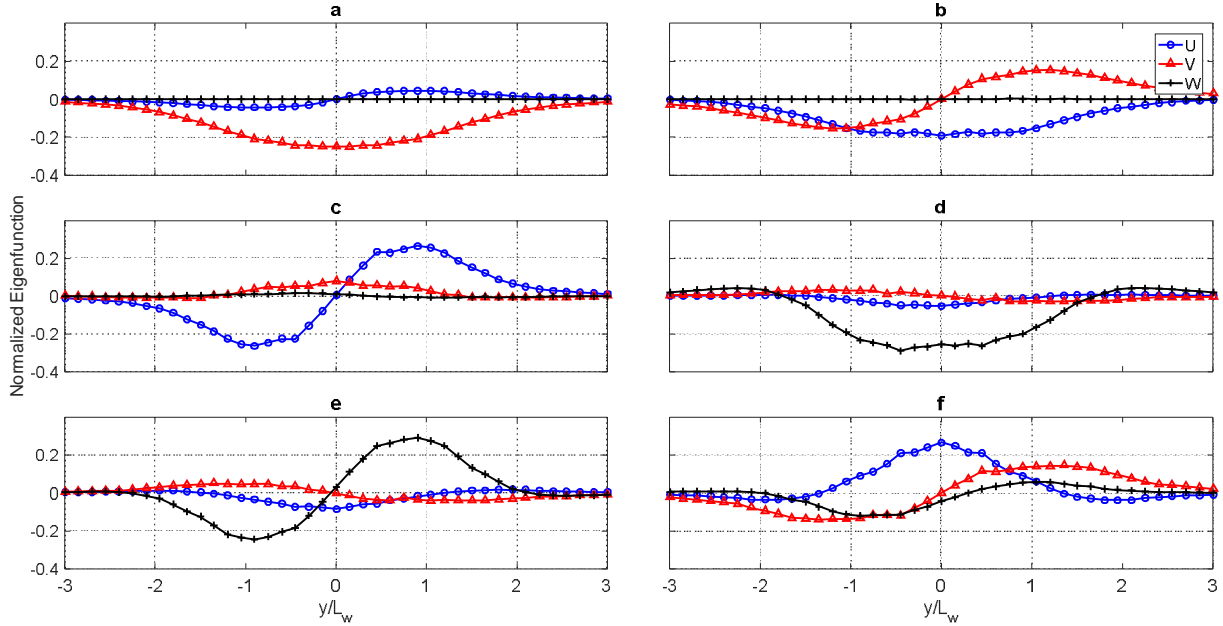


Figure 3.64. Modal profiles for the first six modes in the cylinder wake. Figures (a)-(f) correspond to modes 1-6 respectively.

3.2.12 Cylinder Wake Compact Eddy Structure

The POD analysis performed on the cylinder wake correlation can be continued further by using the three component modal profiles to produce vector plots of the modes in the $y - \tau$ plane. These vector plots represent the dominant eddy structures present in the cylinder wake. The formulation used to compute the compact eddy structures is similar to Equation 1.7, but for zero separation in z the formulation is defined by Equation 3.16.

$$u_j^{(n)}(y', 0, \tau) \Big|_{CES} = \frac{1}{\lambda^{(n)}} \int \phi_i^{(n)}(y) R_{ij}(y, y', 0, \tau) dy \quad \text{Equation 3.16}$$

Figure 3.65 through Figure 3.68 plot the compact eddy structures for the first four modes respectively. In the first mode, shown in Figure 3.65, it is clear that there is a coherent street of alternating sign vortices near the wake centerline. At zero time delay there is a large down sweep before continuing the recirculation pattern. These features suggest that there are large single roller type eddies in the flow. Figure 3.66 shows the characteristic eddy for the second mode. In this mode there is a convergence of the flow toward the wake centerline, without any coherent vortices present. In the eddy structure computed using the third mode shown in Figure 3.67 there is again a street of vortices near the wake centerline where there are three counter rotating vortices. The fourth mode shown in Figure 3.68 again shows a pair of counter rotating vortices. The features present in these characteristic eddy structures are further discussed in Section 3.3.5 when they are compared with the structures seen in the airfoil wake.

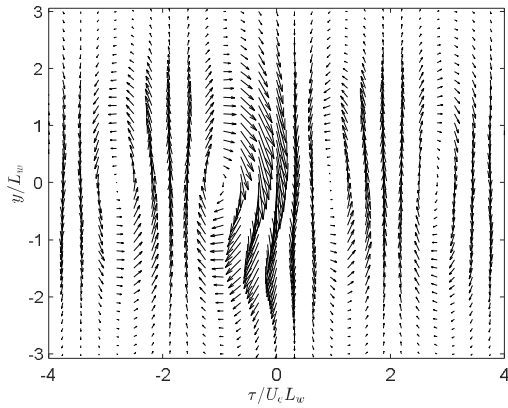


Figure 3.65. Compact eddy structure for the first mode.

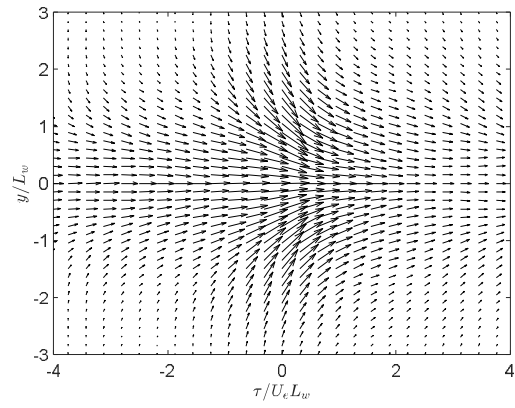


Figure 3.66. Compact eddy structure for the second mode.

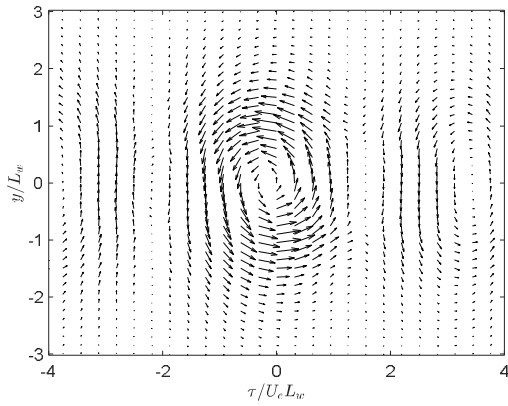


Figure 3.67. Compact eddy structure for the third mode.

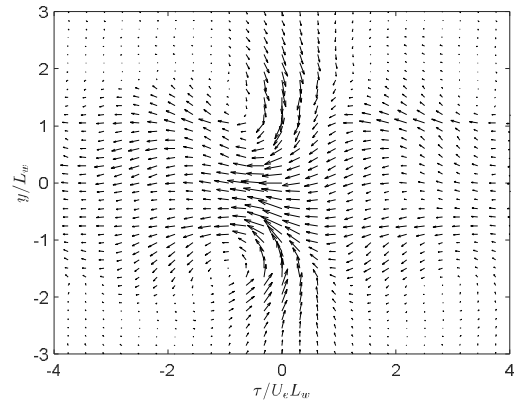


Figure 3.68. Compact eddy structure for the fourth mode.

3.3 Comparison with Airfoil Wake Data

In this section the cylinder wake results will be compared with the analogous results produced for the airfoil wake measured by Devenport (2001). The single point stress profiles are first compared for both the cylinder wakes and the airfoil wake. The cylinder wake measured in the Open Circuit Wind Tunnel is presented at a streamwise station of 20 diameters downstream while the cylinder wake measured in the Stability Wind Tunnel is presented at 20, 15 and 10 diameters downstream. The airfoil wake is presented for positions at three streamwise stations. Comparisons of the two-point correlations for each wake will then be presented. The section will conclude with a comparison of the proper orthogonal decomposition results and characteristic eddy structures in each wake.

3.3.1 Comparison of Normalized Single Point Profiles

The cylinder wake profiles measured in the Stability Wind Tunnel and the Open Circuit Wind Tunnel were compared with the airfoil wake profiles measured by Devenport *et al.* (2001) at several streamwise locations. The cylinder wake profile are presented at 20 diameters downstream of the cylinder center measured in both facilities. In the Stability Wind Tunnel profiles measured

10 and 15 diameters downstream of the cylinder center. The airfoil wake profiles are presented at three streamwise locations normalized on the airfoil chord of 1.67, 5.34 and 11.57. For reference, these normalized positions in the airfoil wake were measured 13.2, 42.3 and 91.6 inches downstream of the trailing edge of the airfoil at a freestream velocity of 27.5 m/s. The cylinder wake profiles measured in the Stability Wind Tunnel in present study were at a streamwise station 40, 30 and 20 inches downstream of the 2 inch diameter cylinder at 20 m/s. In the Open Circuit Facility the wake profiles were measured 30 inches downstream of the 1.5 inch diameter cylinder.

Cadel (2016) performed a study where PIV measurements were made in the same Open Circuit facility and in the wake of the same 1.5 inch diameter cylinder as in the present study. Wake cross sections were measured 9.43 diameters downstream of the cylinder at a freestream velocity and cylinder diameter Reynolds number of 60 000. The data from this study are also included in the wake profile comparisons that follow. Due to the field of view of the measurement technique, data was available for $-1.2 < y/L_W < 1.2$.

Figure 3.69 compares the mean streamwise velocity between the cylinder and airfoil wakes. The difference between the freestream velocity and the velocity profile has been normalized on the deficit velocity, while the y profile coordinates in each profile have been normalized on the half wake width. This figures shows that the mean flow profiles of the cylinder and airfoil wakes are remarkably similar when normalized in this manner. Figure 3.70 through Figure 3.73 compare the Reynolds stress profiles for the streamwise, wake-normal and spanwise normal stresses and the Reynolds shear stress respectively for the cylinder and airfoil wake profiles included in this comparison. Each profile has been normalized on the deficit velocity and the half wake width of each wake. The comparisons in each component of the Reynolds stress profiles show that the stresses in the cylinder wakes measured in the present study and in the study performed by Cadel (2016) are significantly more turbulent than the airfoil wake. The $\overline{u^2}$ Reynolds stress profile measured 10 diameters downstream of the cylinder is nearly 5 times greater in magnitude than the profiles measured in the airfoil wake while the magnitudes of the $\overline{v^2}$ Reynolds stress measured at the same streamwise station in the cylinder wake is nearly 10 time greater in magnitude than the airfoil wake. In the data available from Cadel (2016) it was only possible to extract the Reynolds stress in the v direction and the mean flow in the streamwise direction. The wake measured by Cadel (2016) 9.4 diameters downstream of the cylinder is more turbulent that the wake measured in the Stability Wind Tunnel 10 diameters downstream of the cylinder.

To confirm that the turbulence levels in the wake profiles measured in the present study were not outside of the scope of other plane wakes, data for several cylinder wakes were gathered from the literature. The streamwise Reynolds stresses were compared with each wake to ensure that the turbulence levels seen in the cylinder wakes of the present study aligned with the profiles seen in the literature. Each $\overline{u^2}$ stress profile wake was normalized on the wake half width and the deficit velocity squared. The Reynolds number descriptions of the measured or simulated wakes were each based on the diameter or chord and the freestream velocity. Ong & Wallace (1996) provided a cylinder wake profiles at $x/d = 6$ and a Reynolds number of 3900, and Marasli *et al.* (1993) at a location $x/d = 30$ and Reynolds number of 2000. Wygnanski *et al.* (1986) measured the wakes of an airfoil, solid strip and solid screen in the far wake where the wakes were self-preserving over a

range of Reynolds numbers from 1360 to 6500. Figure 3.74 shows the comparison between the normal streamwise Reynolds stress profiles for the wakes found in the references described above, the Stability Wind Tunnel and Open Circuit cylinder wakes and the wakes measured by Devenport *et al.* (2001) at a Reynolds number of 3.3×10^5 . Cylinder wake LES simulations at a Reynolds number of 60 000 were conducted to replicate the conditions seen in the Stability Wind Tunnel cylinder measurements and were provided by Wang *et al.* (2016). The LES wake data was added to Figure 3.74 from a profile extracted at a streamwise location of $x/d = 10$. Figure 3.74 shows that the wake profile taken from Wang (2016) compares well with the wake measured at the same location in the Stability Wind Tunnel. The cylinder wakes measured in the present study in each facility are framed by the wakes measured by Wygnanski (1986), Marasli (1993) and Ong *et al.* (1996). This figure confirms the findings by previous authors that in some flows the Reynolds stress profiles, in this case $\overline{u^2}$, should not be considered universal. The turbulence structure of the wake is highly dependent on the model geometry used to generate the wake, especially in the near wake. The results shown here gives confidence that the measured cylinder wakes fall within a reasonable range of the wakes found in the literature, although they are several times more turbulent than the airfoil wake measured by Devenport *et al.* (2001).

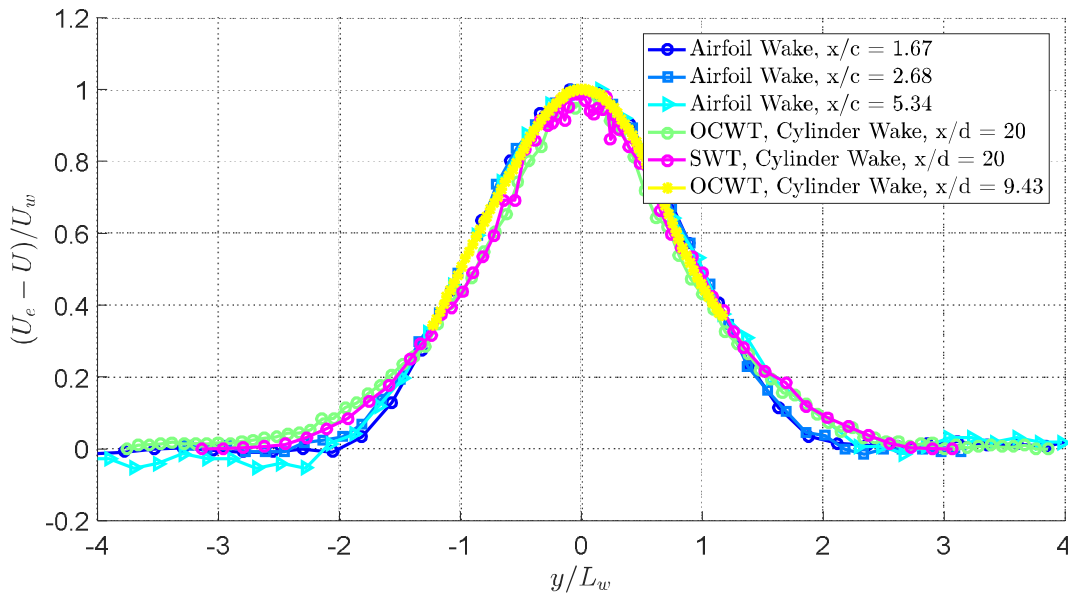


Figure 3.69. Comparison of the mean flow velocity.

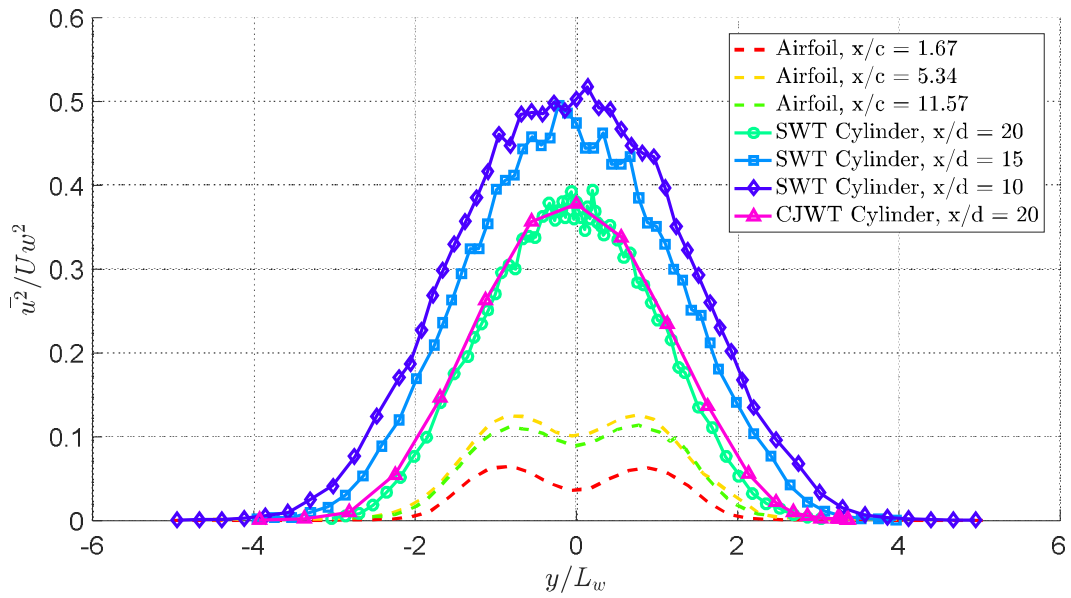


Figure 3.70. Comparison of the $\overline{u^2}$ Reynolds stress profiles between the cylinder and airfoil wakes.

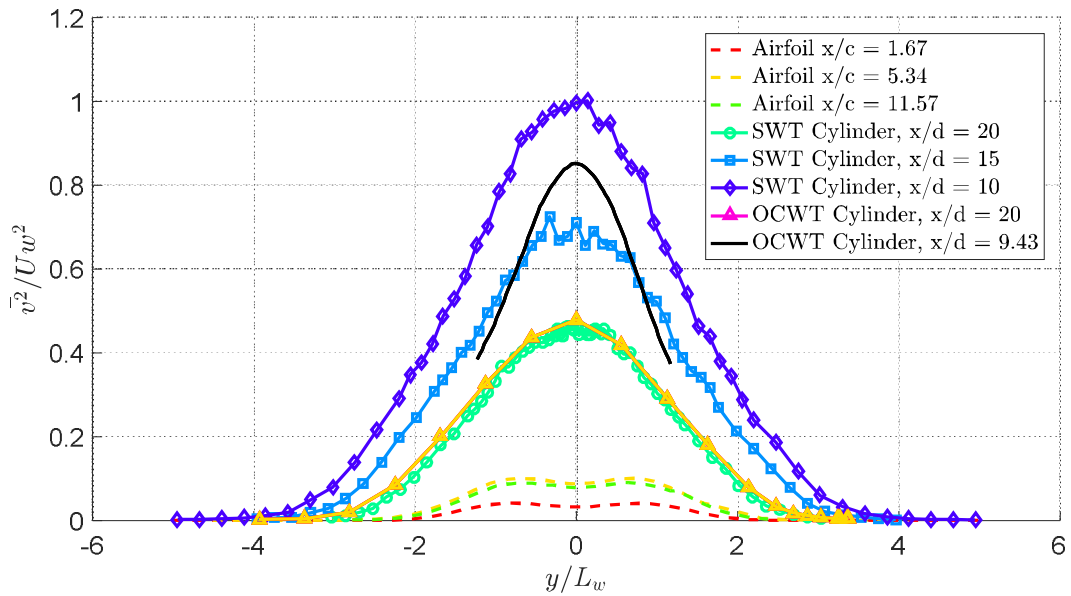


Figure 3.71. Comparison of the $\overline{v^2}$ Reynolds stress profiles between the cylinder and airfoil wakes.

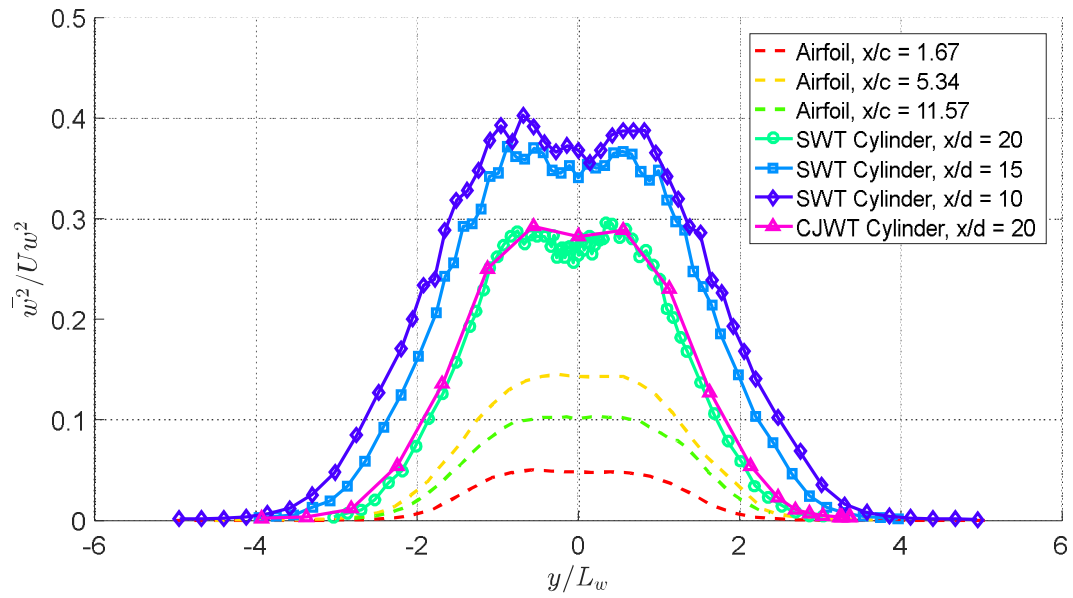


Figure 3.72. Comparison of the $\overline{w^2}$ Reynolds stress profiles between the cylinder and airfoil wakes.

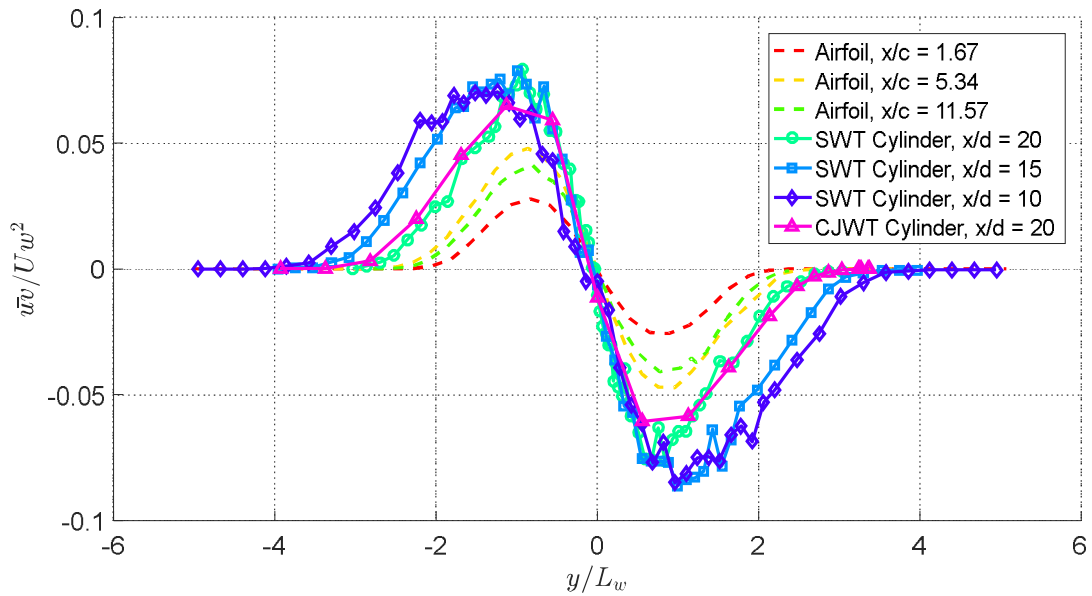


Figure 3.73. Comparison of the \overline{uv} stress profiles between the cylinder and airfoil wakes.

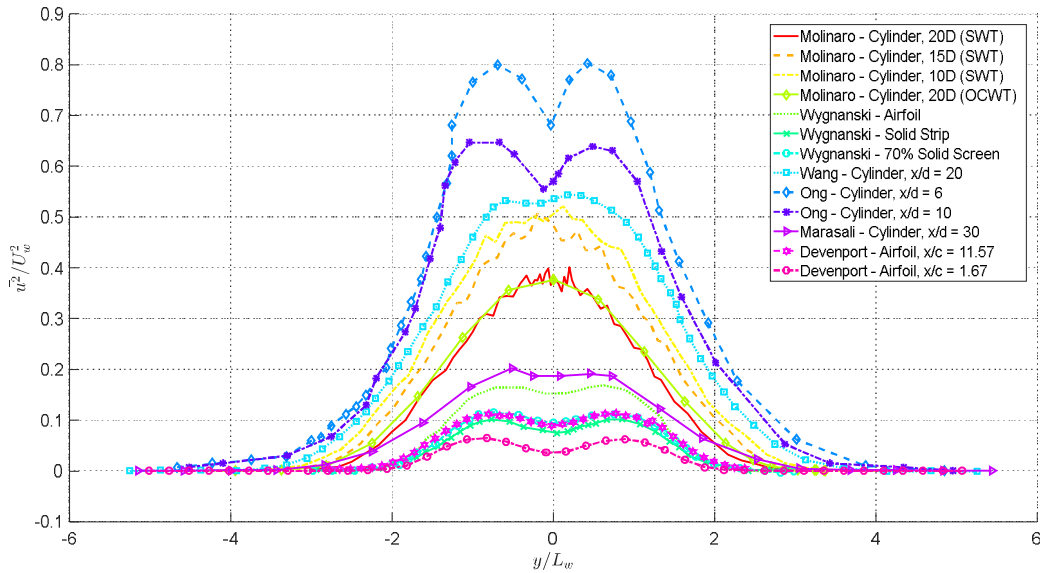


Figure 3.74. Comparison between the $\overline{u^2}$ stress profiles for different wakes from literature

3.3.2 Zero Separation Time Delay Correlation Coefficients in the Wake Center

Before the two-point correlation cross sections are compared, the two-point time delay correlation coefficient at zero separation are presented in the wake center for the cylinder and airfoil wakes. The airfoil wake correlation was measured at a streamwise station of $x/c = 8.33$ measured from the trailing edge while the cylinder wake correlation was measured at a location twenty diameters downstream of the cylinder center. The time delay correlation for zero probe separation was extracted from the two-point correlation function of each wake and plotted as coefficients in Figure 3.75 for the cylinder wake and Figure 3.76 for the airfoil wake. The correlation coefficients are plotted for normalized time delays between -20 and 20 in the cylinder wake and for time delays between -8 and 8 in the airfoil wake at the wake center where $y = 0$. It is clear that the cylinder wake is correlated to greater time delays in the u and v velocity components. In the airfoil wake the correlation coefficient in the u component of velocity component decays rapidly toward zero. In the cylinder wake the ρ_{11} correlation also decays toward zero, however the correlation is sustained at greater time delays. In the correlation coefficient in the v component of velocity there is strong oscillation in the cylinder wake due to the vortex shedding in the cylinder wake. In the airfoil wake there is some oscillation, however the motion is quickly damped. This shows that there is stronger and more coherent shedding in the cylinder wake since the oscillation in the correlation coefficient is sustained to a significantly greater normalized time delay of ± 20 . The period of the oscillation in the ρ_{22} correlation coefficient implies a Strouhal number of 0.2 . This agrees with the Strouhal number computed using the shedding frequency of the cylinder extracted from the coherence figures presented in Section 3.2.9. In both the airfoil and cylinder wakes the correlation coefficient computed using the w velocity shows a similar distribution where the correlation rapidly approaches zero.

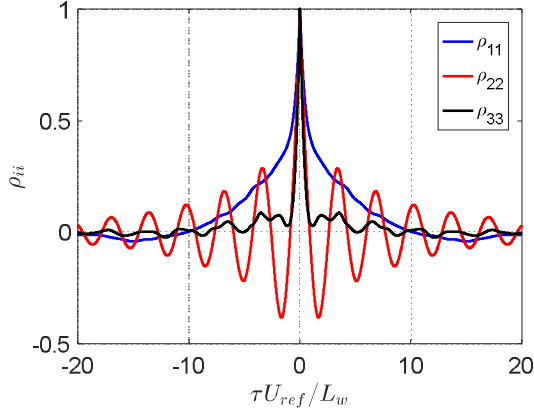


Figure 3.75. Time delay correlation coefficient in the cylinder wake.

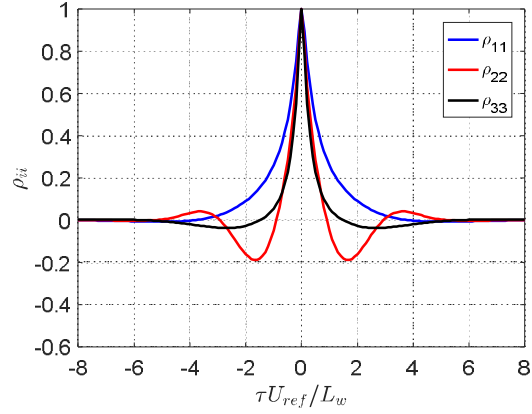


Figure 3.76. Time delay correlation coefficient in the airfoil wake.

3.3.3 Cylinder and Airfoil Wake Two Point Zero Time Delay Correlation Comparison for $y/L_w = 1$

The structure of the two-point correlation in the cylinder and airfoil wakes are compared for a correlation anchor point of $y/L_w = 1$ and a time delay of zero. In the following correlation figures the wake is always presented with the spanwise direction, z , on the horizontal axis and the normal-to-wake direction, y , on the vertical axis. The wake normal coordinate is expressed as a separation from the fixed probe for each correlation component. In each figure the correlations computed using the cylinder and airfoil wakes are plotted side by side on equivalent axes limits from -3 to 3 in the y and Δz directions, but on different color scales. In each figure, the correlations are plotted with 10 contour levels. In the naming convention, R_{ij} , i corresponds to the fixed probe velocity component while j corresponds to the moving probe velocity component. In both the cylinder and airfoil wakes the two point correlation has been normalized on U_w^2 . In the following comparisons significant correlation at large separations was defined as a correlation value larger than 1% of the maximum correlation seen in a specific component.

Figure 3.77 through Figure 3.79 show the two point correlations for zero time delay for the streamwise, wake-normal and spanwise velocity components respectively. Both the cylinder wake and airfoil wake correlation components show similar structures. In each correlation component there is a region where the correlation is maximum near zero y and z separation. The correlation value then decreases toward zero as the separation in either direction is increased. In each of the normal correlation components the region where the cylinder wake has significant positive correlation extends past that seen in the airfoil wake. This is likely due to the stronger and more coherent vortices shed by the cylinder. This also implies that the length scales are longer in the cylinder wake. In the R_{11} and R_{22} directions the center of the correlation structure appears to be offset towards the positive Δy direction. This offset is toward the fixed probe and is observed in both wakes. In the correlations for both wake flows, the R_{11} and R_{22} are correlated at larger separations in the negative Δy direction. In the wake normal direction the correlation spans larger y and z separations in the cylinder wake, about 5 half wake widths. In both wakes the R_{33} correlation spans the shortest range of y and z separations and is stretched along the cylinder span.

Figure 3.80 through Figure 3.85 compare the two point correlations computed using other velocity component combinations between the fixed and moving probes. These correlations are the off diagonal terms in the two-point correlation tensor. In each of these figures the magnitude of the maxima of the correlation in the cylinder wake are closer to the maxima of the correlations in the airfoil wake than previously seen in the normal correlation component directions. For each cross correlation the maximum correlation value between both wakes are within about 50% of each other where in the normal correlations the maximum correlation seen in the cylinder wake is 2-4 times greater than in the airfoil wake. This is also observed in Figure 3.73 above where the Reynolds shear stress profiles in the cylinder and airfoil wakes were closer in magnitude than the normal stresses. The Reynolds shear stress level seen in the cylinder wake is about 2 times greater than in the airfoil wake while the normal stress levels in the cylinder wake are 2-4 times greater in the cases of $\overline{u^2}$ and $\overline{w^2}$ while $\overline{v^2}$ is about 10 times greater than the levels of the stress profiles in the airfoil wake.

Figure 3.80 compares the correlation computed using the streamwise velocity component from the fixed probe and the wake-normal velocity component from the moving probe, R_{12} . In the y direction the cylinder wake is correlated over a larger distance, about 4.6 half wake widths, while the airfoil wake is only correlated over about 3.9 half wake widths. In the spanwise direction the correlations extend the same distance, about 1.6 half wake widths, at the wake center. The center of the correlation structure where the correlation is highest is slightly skewed in the cylinder wake where the center is about 0.5 half wake widths from zero y and z separation. In the airfoil wake the correlation structure is centered near zero y and z separation. The cylinder wake also shows more skew toward the positive y separation side of the wake whereas the in the airfoil wake the correlation is reasonably symmetric. The signs of the correlation are equivalent in each wake.

Figure 3.81 compares the correlation component R_{13} . In this case the cylinder wake is correlated over the entire spatial range considered for comparison. The signs of the correlations are again equivalent, however the cylinder wake features larger correlation lobes when the probe separation in the y direction is negative. In the cylinder wake correlation the lobes centered in the positive Δy side of the wake appear to extend into the side of the wake where the y separation is negative. In the airfoil wake correlation there is a clear separation of the lobes for positive and negative y probe separations. The centers of the lobes seen in the cylinder wake are located at noticeably larger separations than seen in the airfoil wake. In the cylinder wake the lobes on the positive y separation of the wake are located at 1.2 half wake widths in y and ± 0.7 half wake widths in z while the center of the lobes in the airfoil wake occur at 0.35 half wake widths in y and ± 0.4 half wake widths in Δz . The same is true in the negative y separation side of the wakes where the center of the lobes in the cylinder wake are located at $\Delta y/L_w = -1.7$ and $\Delta z/L_w = \pm 1.2$ while in the airfoil wake the centers occur at $\Delta y/L_w = -0.55$ and $\Delta z/L_w = \pm 0.7$. The alternating signs of the lobes occur due to the alternate vortex shedding nature of the cylinder. This comparison of the location of the alternating lobes suggest that the structures shed by the cylinder remain coherent at larger y and z separations.

Figure 3.82 compares the R_{21} correlation component between wakes. In this component both wakes show a skew in the negative Δy direction in the wake. The cylinder wake shows

significantly larger correlation region and a heavier skew toward the negative Δy direction. In this component the maximum of each correlation is located at zero y and z separations. The cylinder wake is correlated at larger y and z separations in the negative Δy region of the wake. On the positive Δy side of the wake the correlations in each wake are correlated to equal distances in Δz . The cylinder wake is correlated at larger y separations to about $\Delta y/L_w = 1.8$ while the airfoil wake is only correlated to $\Delta y/L_w = 1$.

Figure 3.83 compares the R_{23} correlation component. The same alternating sign behavior of the R_{13} correlation component is seen in the R_{23} correlation component. In this comparison the center of the cylinder and airfoil wake correlation structures appear to be centered near zero y and z separations. The cylinder wake correlation is again better correlated over greater separations. The correlation in the airfoil wake is biased in the negative Δy direction where as the cylinder wake correlation seems to be evenly distributed between the positive and negative Δy directions. In the port half of the wake the center of the lobes in both wakes appear to both occur at y/L_w and z/L_w separations of 0.5. In the starboard half of the wake the lobes in the cylinder wake appear to be centered at the point $y/L_w = z/L_w = 1$ while in the airfoil wake the lobes in the starboard side of the wake appear to be centered at the location $y/L_w = z/L_w = 0.5$.

Figure 3.84 compares the R_{31} correlation component. Both correlation structures show lobes that surround smaller pockets of correlation regions of opposite sign. The central structure in the cylinder wake appear smaller than in the airfoil wake. In airfoil wake correlation there are two dislocated regions on the positive and negative Δy separations sides of the wakes with signs opposite the central lobes. In the cylinder wake correlation it appears that these regions are connected to form a single correlation region surrounding the lobes located at the wake center. In the z direction significant correlation exists in the cylinder wake at greater z separations. On the negative Δy side of the wake the cylinder wake is correlated for z separations up to $\pm 3 z/L_w$. The comparison in the R_{31} correlation component again shows that the cylinder wake is better correlated in the y and z directions.

Figure 3.85 compares R_{32} for each wake. The cylinder wake correlation shows correlated regions that alternate in sign throughout the wake. In the airfoil wake correlation there are only two main lobes that extend into the negative y separation side of the wake. In this component of the correlation function the cylinder wake is correlated on both sides of the wake, over the range $-2 < \Delta y/L_w < 1.5$, while the airfoil wake is best correlated on the negative Δy side of the wake over the range, $0 < \Delta y/L_w < -3$. In this section only comparisons for the single fixed probe location of $y/L_w = 1$ have been discussed. In Appendix C there are correlation comparisons for $0 < y/L_w < 2.5$ with an introductory description of the comparison figures.

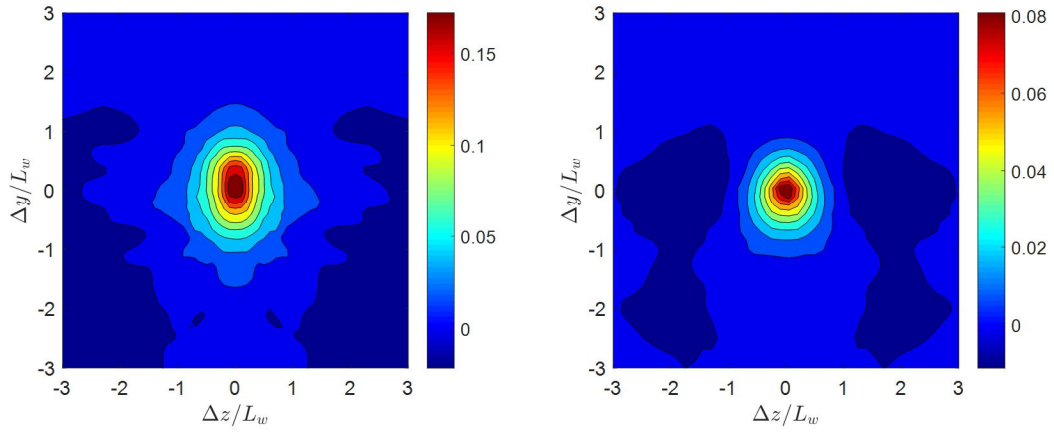


Figure 3.77. Comparison between the cylinder (left) and airfoil (right) R_{11} correlations at $y/L_w = 1$

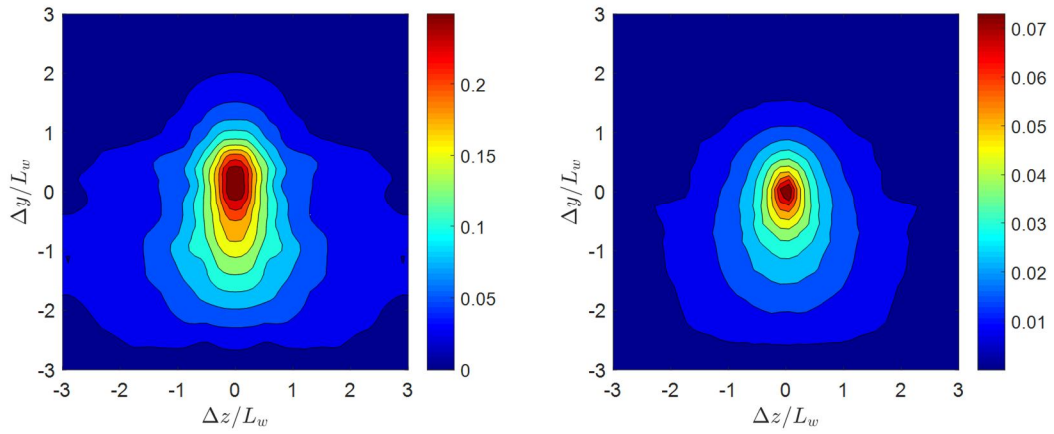


Figure 3.78. Comparison between the cylinder (left) and airfoil (right) R_{22} correlations at $y/L_w = 1$

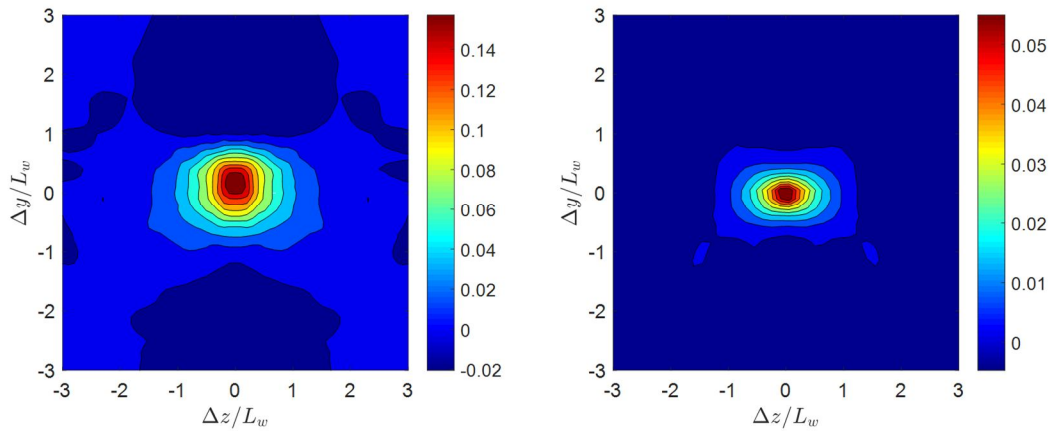


Figure 3.79. Comparison between the cylinder (left) and airfoil (right) R_{33} correlations at $y/L_w = 1$

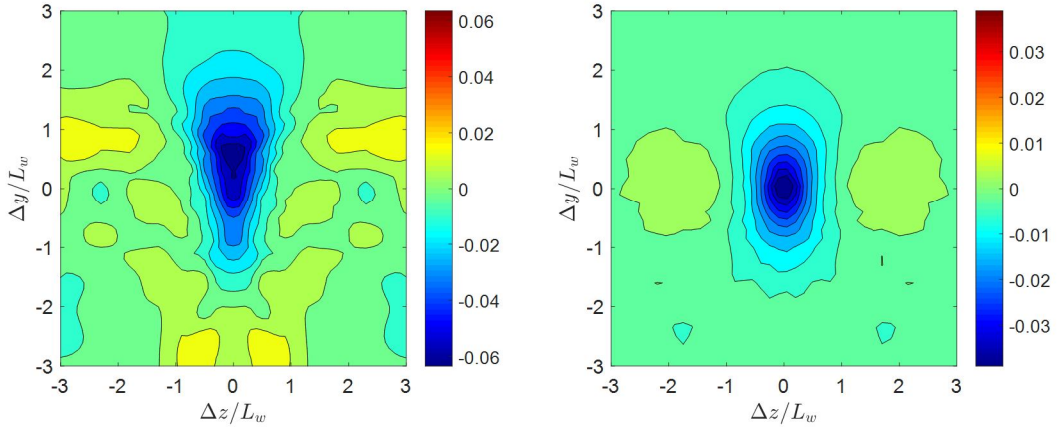


Figure 3.80. Comparison between the cylinder (left) and airfoil (right) R_{12} correlations at $y/L_w = 1$

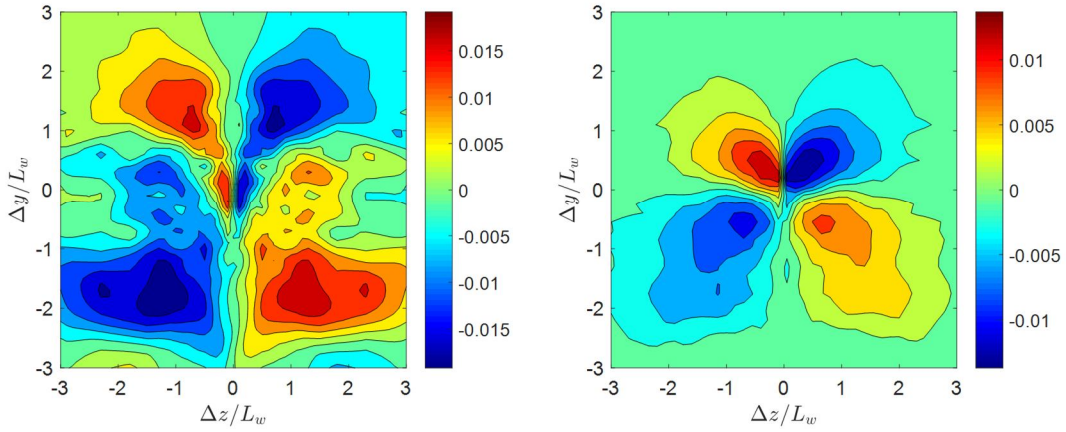


Figure 3.81. Comparison between the cylinder (left) and airfoil (right) R_{13} correlations at $y/L_w = 1$

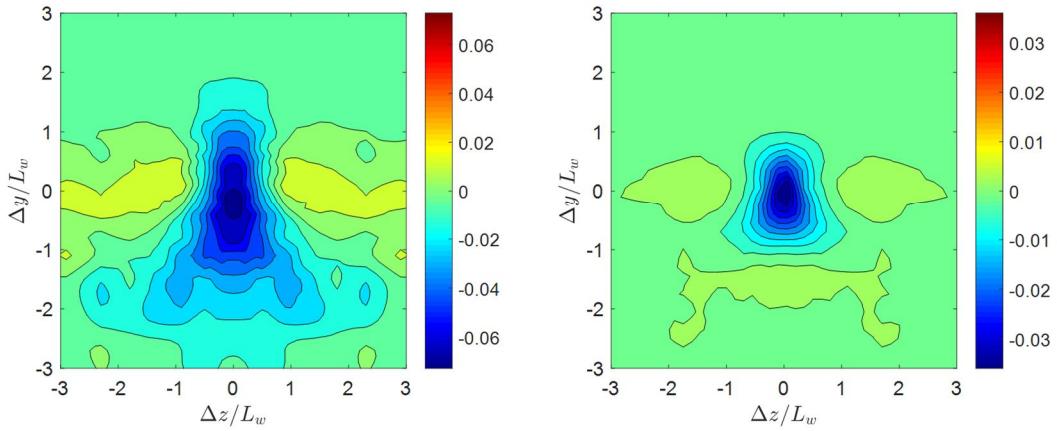


Figure 3.82. Comparison between the cylinder (left) and airfoil (right) R_{21} correlations at $y/L_w = 1$

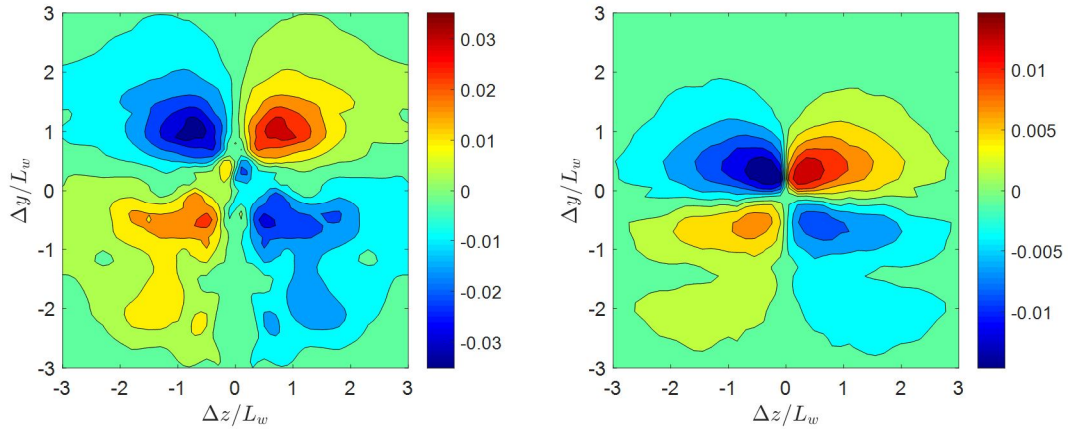


Figure 3.83. Comparison between the cylinder (left) and airfoil (right) R_{23} correlations at $y/L_w = 1$

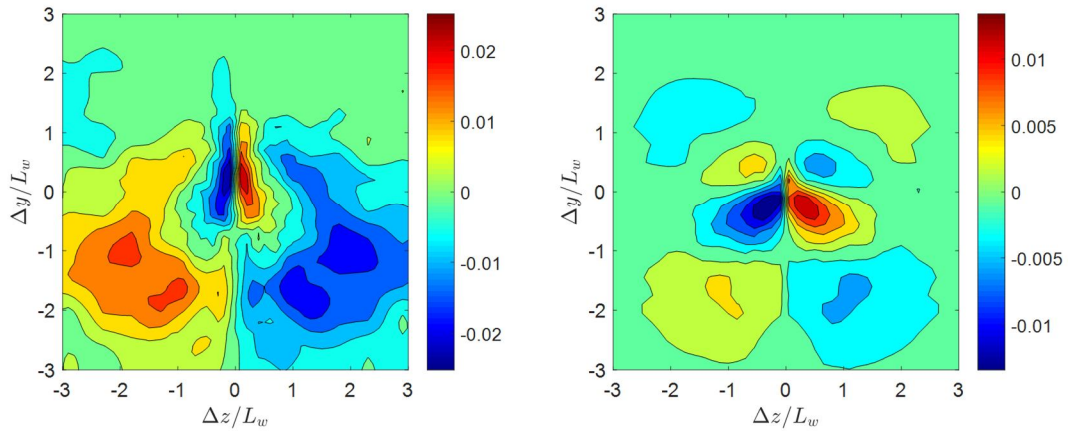


Figure 3.84. Comparison between the cylinder (left) and airfoil (right) R_{31} correlations at $y/L_w = 1$

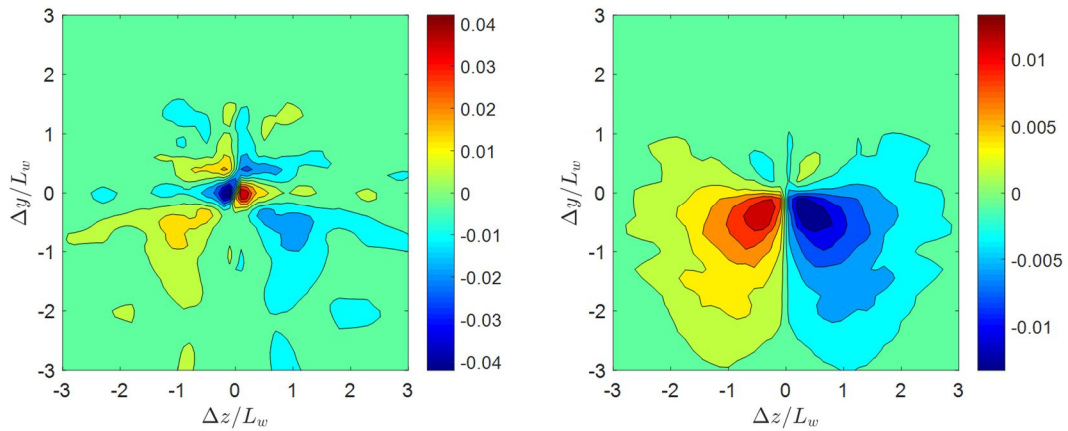


Figure 3.85. Comparison between the cylinder (left) and airfoil (right) R_{32} correlations at $y/L_w = 1$

3.3.4 Modal Velocity Profile Comparisons

The proper orthogonal modes in the airfoil and cylinder wakes were computed using the formulations defined in Sections 1.3 and 3.2.11. The zero z separation time delay correlation was used in both wakes to compute the eigenvalue spectrum and modal velocity profiles. The correlation is shown at zero time delay in Figure 3.89 below for the cylinder and airfoil wakes. Figure 3.88 compares the eigenvalue spectrum, normalized on the deficit velocity, computed using the correlation in the cylinder and airfoil wakes. The figure shows that the magnitude of the eigenvalues in the cylinder wake are greater than in the airfoil wake. The figure also shows that the first few modes in the cylinder wake dominate and contain a significant portion of the total energy of all the modes. The first mode contains about 53% of the total kinetic energy. In the airfoil wake the first mode accounts for 48% of the total energy of all of the modes. This uneven distribution of energy in the modes in the cylinder wake is due to the strong coherent vortex shedding in the cylinder wake. Based on the energy in the modes of the airfoil wake, there is a more varied mixture of turbulence scales.

Figure 3.86 and Figure 3.87 compare the modal profiles computed using the cylinder and airfoil wake correlations respectively. When comparing the modal profiles, note that the sign of the profile is arbitrary due to the manner in which they were computed. The first two modes between the airfoil and cylinder show similar profile shapes. The u and v profiles both show the same trends in both wakes, where one component is symmetric and the other is anti-symmetric. The profiles for the third mode are similar for both wakes although for the cylinder wake the u velocity profile dominates while in the airfoil wake shows strong contributions from the v and u velocity components. Note that the w velocity component does not appear in the first three modes for either wake. In the fourth mode the w velocity modal profile is the dominant profile in the cylinder wake while the airfoil wake has no profile in the w component of velocity. The airfoil wake does show complex profile shapes in the u and v velocities. In the fifth and sixth modes the airfoil wake only shows nonzero profiles in the w velocity component while the cylinder wake shows nonzero profiles for all three velocity components. It is important to recall that the modal profiles are ordered only by eigenvalue. Figure 3.88 shows that the eigenvalues for modes three to six are relatively similar in the cylinder wake flow. With this in mind there is a rough equivalence between modes four, five and six in the cylinder wake and modes five, six and four in the airfoil wake respectively.

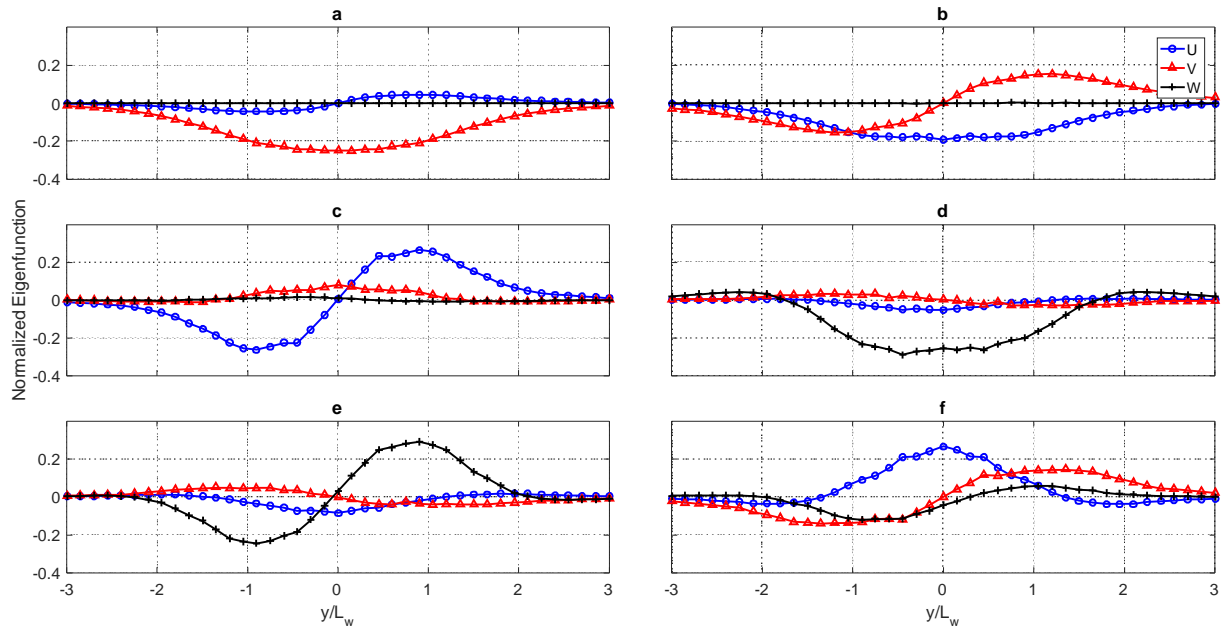


Figure 3.86. Modal profiles for the first six modes in the cylinder wake. Figures a-f correspond to modes 1-6 respectively

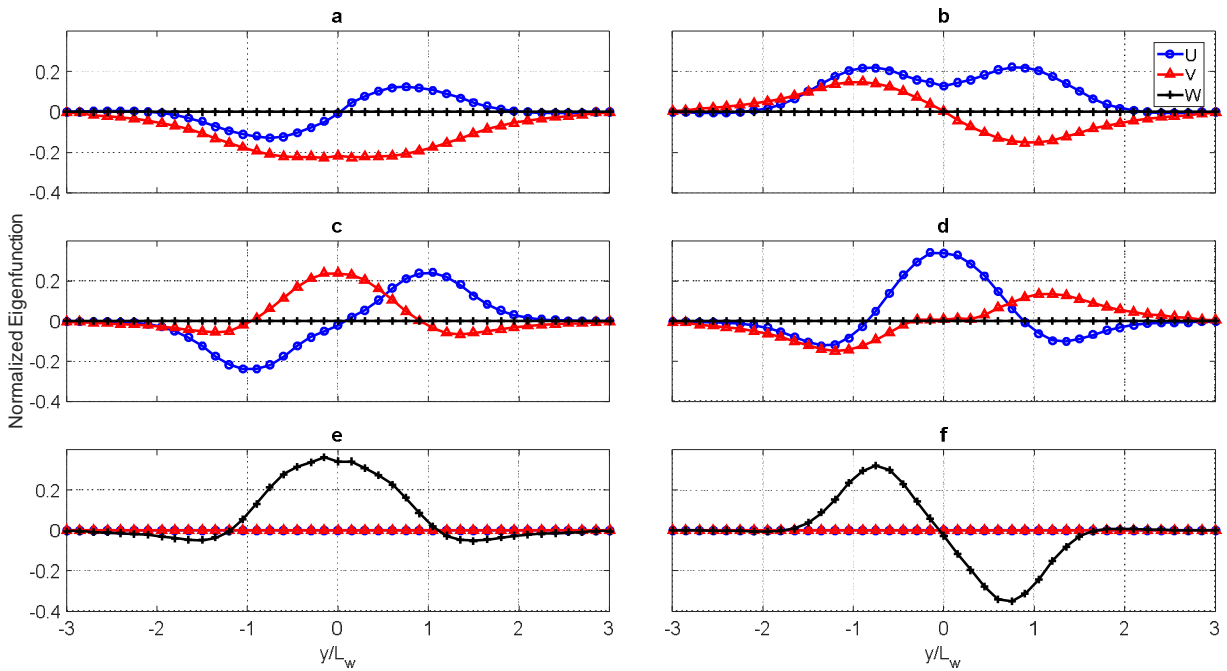


Figure 3.87. Modal profiles for the first six modes in the airfoil wake. Figures a-f correspond to modes 1-6 respectively

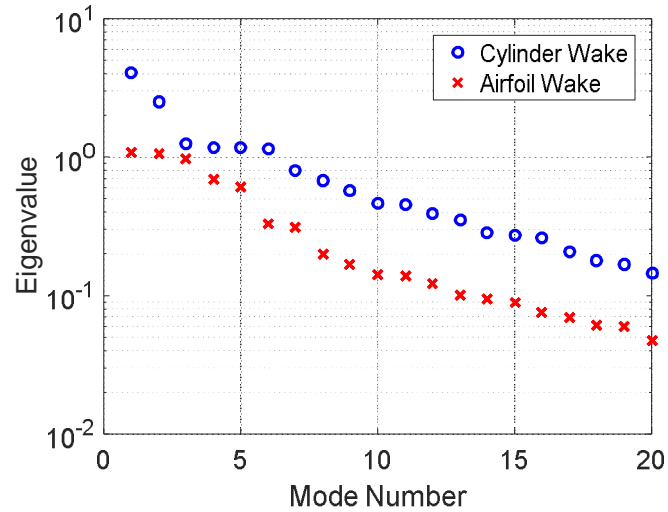


Figure 3.88. Comparison of the eigenvalue spectrum in the cylinder and airfoil wakes.

3.3.5 Compact Eddy Structure Comparison

The formulations described in Sections 1.3 and 3.2.12 were used to determine the compact eddy structures in the airfoil wake so that they could be compared to those computed in the cylinder wake. To compute these structures the time delay correlation for zero z separation is needed. Figure 3.89 shows the zero separation correlations for the cylinder and airfoil wakes. The cylinder wake correlation is shown at a streamwise station 20 diameters downstream while the airfoil wake is presented at a location normalized on the chord of 8.33. Both correlations were computed over the range of ± 3 in y/L_w and in y'/L_w . In each wake the correlation is expressed as a coefficient to plot the correlations on equivalent scales. The correlation plots show similar features in each component of the correlation. The R_{22} correlation is largest in each wake, although in the cylinder wake the correlation extends a greater distance in y and y' . At first glance it appears that the airfoil wake maintains a maximum correlation over a greater distance than the cylinder wake, indicated by the constant color level on the center diagonal of the normal correlations. However, the ridge of maximum correlation in the cylinder wake normal correlations is maintained over an equal distance in each normal direction. Figure 3.89 shows that cylinder wake is correlated at greater y and y' locations indicated by correlation coefficient values greater than 0.1 in the cylinder wake correlation at greater probe separations.

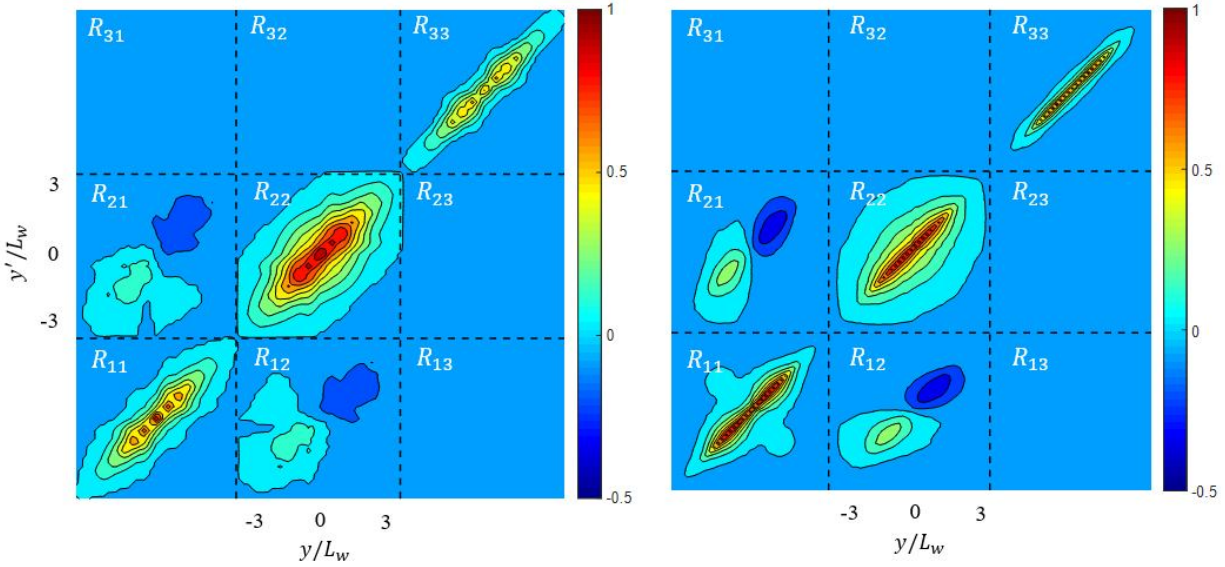


Figure 3.89. Comparison of the zero separation correlations for the cylinder (left) and airfoil (right) wakes.

The characteristic eddy structures are shown for the cylinder wake at a station 20 diameters downstream and the airfoil wake is presented at a location normalized on the chord of 8.33. The eddy structures for the first four orthogonal modes were computed over the range ± 3 in y/L_w and ± 4 in $\tau U_{ref}/L_w$ for $\Delta z = 0$. The eddy structures presented evolve in the $y - \tau$ plane. The characteristic eddy structures computed for the cylinder and airfoil wakes for the first four modes are compared in Figure 3.90 through Figure 3.93. Figure 3.90 shows that there is strong similarity in the eddy structure first mode, which contains the most energy for both wakes. The dominant feature the velocity field of each wake is a strong down wash at zero time delay. The analysis shows that cylinder wake has only counter-rotating vortices that appear singularly at positive and negative time delays while the airfoil wake sees additional counter rotating paired vortices at positive time delays. The cylinder wake also shows eddies with larger diameters. In Figure 3.91 the second mode is compared for both wakes. Again, there are some similarities in the eddy structures. In both wakes the eddies appear to converge on the wake center at zero time and have a column of flow moving along the wake center for all time delays in the domain considered. The structure of the airfoil wake shows vortices near the edges of the wake while the cylinder wake does not. In the eddy structures of the third mode, shown in Figure 3.92, the airfoil wake shows only a single vortex at the wake centerline near a time delay of one. In this mode the cylinder wake shows a strong rotating structure in the wake center near zero time delay and also contains two additional large counter rotating structures at normalized time delays of -4 and 3 . The eddy structures for the fourth modes are shown in Figure 3.93. There is again some similarity between the velocity fields of each wake in this mode. In both wakes there are vortices located near the half wake width on both sides of the wake. In the center of the counter rotating vortices there is a column of flow moving right to left in time delay. In the airfoil wake this column extends between normalized time delays of ± 2 while the in cylinder wake this flow feature remains coherent over a greater time delay range of ± 4 .

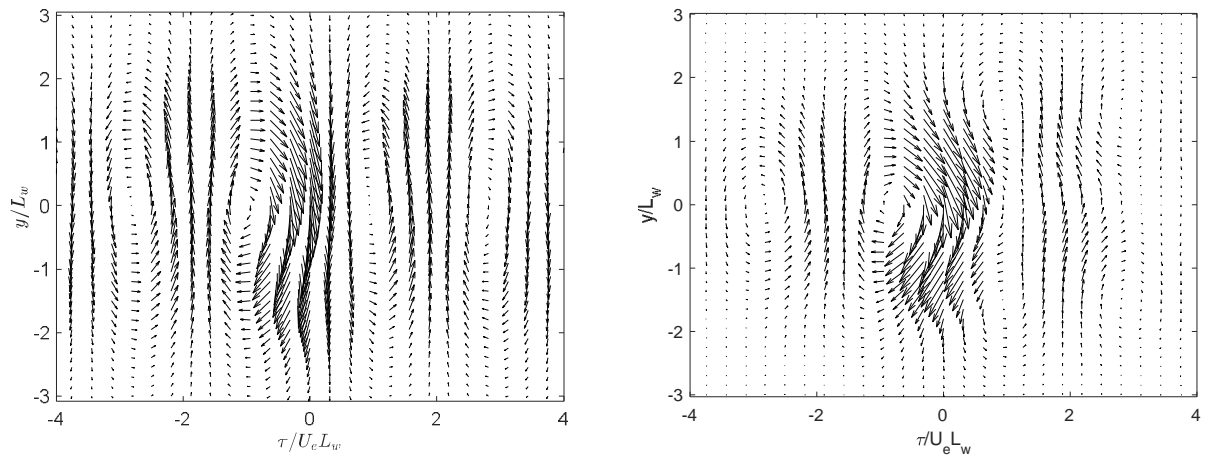


Figure 3.90. Comparison of the eddy structures for the first mode in the cylinder (left) and airfoil (right) wakes.

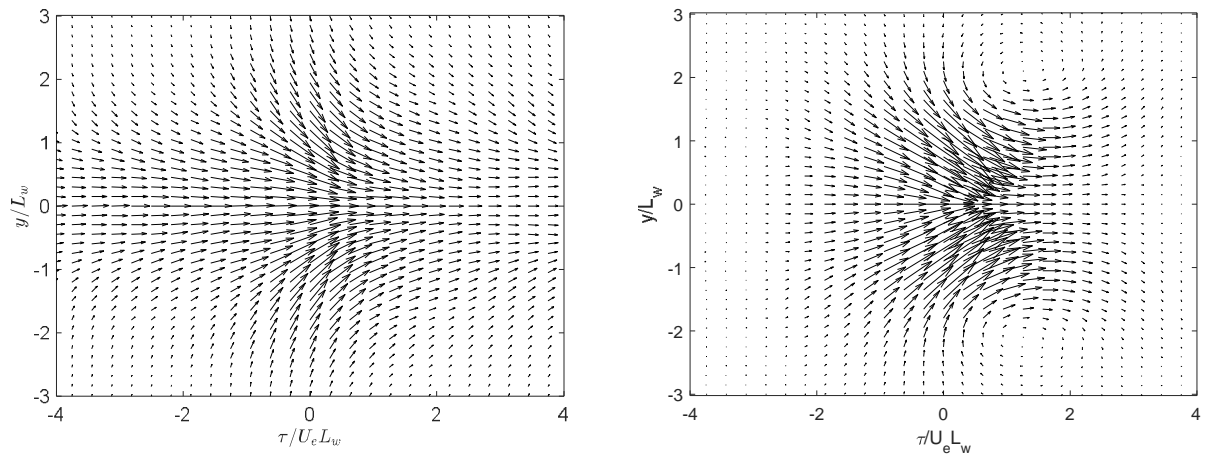


Figure 3.91. Comparison of the eddy structures for the second mode in the cylinder (left) and airfoil (right) wakes.

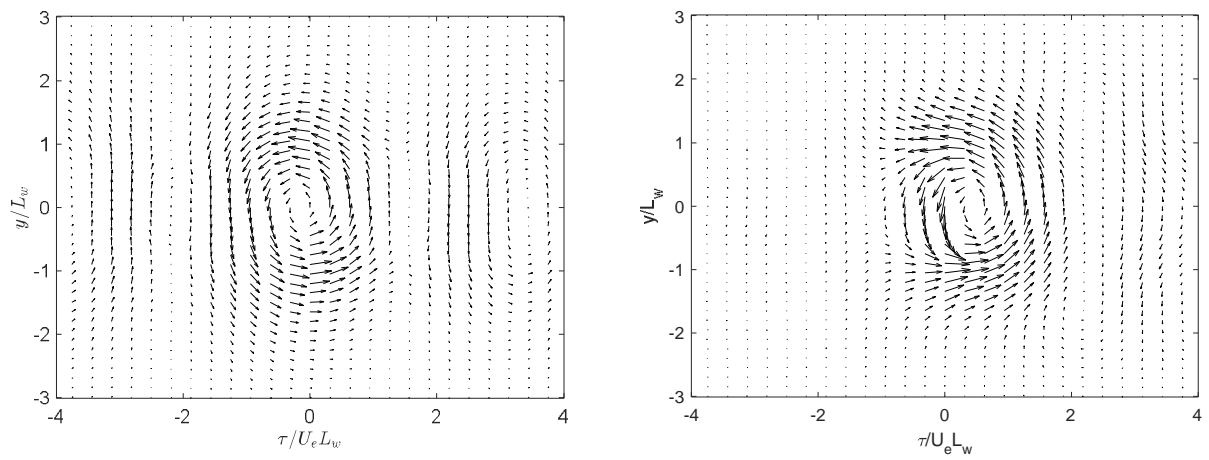


Figure 3.92. Comparison of the eddy structures for the third mode in the cylinder (left) and airfoil (right) wakes.

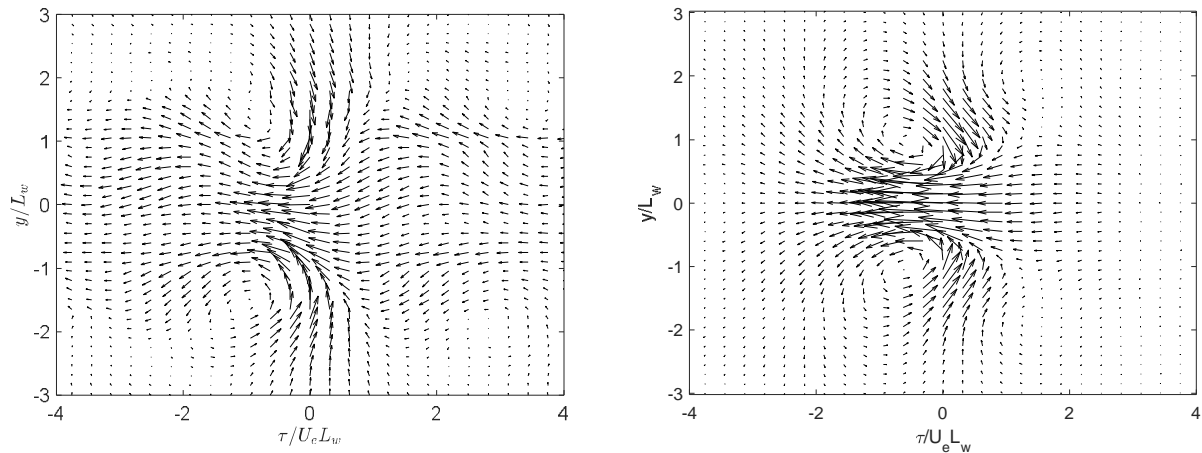


Figure 3.93. Comparison of the eddy structures for the fourth mode in the cylinder (left) and airfoil (right) wakes.

3.4 Discussion

The cylinder wake and airfoil wake flows have been compared in Chapter 3 using the Reynolds stress profiles, two-point correlations and proper orthogonal decomposition. Each of the comparisons analyzed are relevant to larger study that is focused on developing a deeper understanding in the turbulence ingestion noise problem. The Reynolds stress profile comparisons showed that the cylinder wake flow was substantially more turbulent than the airfoil wake flow, while supporting a very similar mean flow. The two-point correlations showed that the structures in the cylinder wake remain coherent to longer time delays and probe separations than those present in the airfoil wake. The comparison of the modal profiles that describe the eddy structures in the cylinder and airfoil wakes is the culmination of the comparison between the cylinder and airfoil wake flows. These comparisons again show that the structures in the cylinder wake remain coherent at greater time delays and greater probe separations.

The results from all of the comparisons made between the structure of the two flows show that although the mean flows of both plane wakes are similar, the turbulence structures are quite different. This suggests that an open rotor ingesting the cylinder wake will produce a very different sound profile than a rotor ingesting an airfoil wake. For example, the larger and more turbulent coherent structures in the cylinder wake will cause higher blade-to-blade coherence and lead to a louder far field sound produced by the rotor. More analysis into predicting the sound field radiated from an open rotor ingesting a cylinder or airfoil wake is needed to complete this comparison of wake inflow conditions. The larger study can then conclude exactly how the differences in the turbulence structures seen in both wakes will influence to the predicted sound field.

Chapter 4: Conclusions

This thesis has described an experimental study of the two-point correlation structure of a cylinder wake. Single and two point measurements were performed on an untripped cylinder at a Reynolds number based on the cylinder diameter and freestream velocity of 60 000. The majority of the wake measurements took place at a location in the mid-wake region 20 diameters downstream of the cylinder center. The ultimate goal of the present study is to document the four dimensional space-time correlation in the cylinder wake for use in a larger study where the sound radiated by an open rotor due to the ingestion of the wake was studied. The two-point correlation serves as the complete boundary condition for this problem.

Single point measurements were performed in the Stability Wind Tunnel. A second set of measurements were performed in the Virginia Tech Open Circuit Wind Tunnel to document the full two-point correlation tensor of the cylinder wake to provide the complete boundary condition for the larger study. Since the cylinder wakes were measured in two different facilities, great care was taken to ensure that the mean velocity, Reynolds stress profiles and the two-point correlation would accurately represent the correlation function in the wake present for the measurement in the larger study. The correlation function in the cylinder wake was further processed using proper orthogonal decomposition to give insight into the eddy structure of the cylinder wake. The correlation function of the cylinder has been reduced to a form that can be used as the input condition for existing acoustic prediction methods.

The single point measurements measured as part of the larger study and the single and two-point measurements performed in the secondary facility were compared with identical measurements obtained in a previous measurements in the wake of a NACA 0012 airfoil completed by Devenport (2001). The comparisons between Reynolds stress profiles measured in both cylinder wakes and the airfoil wake show that the cylinder wake is substantially more turbulent than the airfoil wake. Several wakes were found in the literature and confirmed that the turbulence levels seen in the cylinder wake are not out of the scope of the work completed by other authors.

The two-point correlation components were compared for the cylinder and airfoil wakes. The correlations in the cylinder wake show that the cylinder wake has substantially higher correlation values than seen in the airfoil wake at identical positions. The cylinder wake is also correlated to larger y and z separations than the airfoil wake. This suggests that there are stronger, and more coherent eddy structures in the cylinder wake.

The zero separation time delay correlation coefficients showed a strong oscillation in the wake-normal component of velocity due to the nature of the shedding of the cylinder. The proper orthogonal decomposition analysis gave insight into the turbulent structures in the cylinder and airfoil wakes. The POD modes computed using the three components of the correlation function in a single coordinate direction showed similar shapes. The airfoil had no contribution of the w velocity component in the first four modes while the cylinder wake did have a nonzero w velocity profile in the fourth mode. The eddy structures computed using POD for the cylinder and airfoil wakes show strong similarities for the first four modes. Especially in the first and third modes it is

clear that the cylinder wake is better correlated at greater separations and time delays since there are more vortices present at greater time delays.

Overall, the correlation structure, dominant POD modal profiles and eddy structures for the airfoil and cylinder wakes are similar in some instances but also remarkably different in others. The cylinder is significantly more turbulent and is better correlated at larger separations and time delays. This suggests that the ingestion of the cylinder wake will be more complex since there are presumably larger, stronger and more organized eddies present in the flow. Longer length scales in the cylinder wake means that a single eddy will be cut more times by successive blades when pulled into a rotor, generating more sound. The cylinder wake correlation data has been organized into a single Matlab data file such that it can easily be used in the larger study where acoustic prediction methods for a rotor ingesting turbulence can be computed. The work completed here shows that the cylinder and airfoil wake flows show some significant differences in the flow structure. Further investigation is needed to assess how these differences in the flow structures will influence the predicted sound profiles computed using the cylinder and airfoil two-point correlation functions.

References

- Agelinchaab, M., Paul, S., & Tachie, M. (2009). The Structure of Near Wake of Finite Circular and Square Cylinders. *Manufacturing Engineering*, (June), 1–11. <https://doi.org/10.2514/6.2009-3564>
- Alexander, W. N., Molinaro, N., Hickling, C., Murray, H., Devenport, W., Glegg, S. A. L. (2016). Phased Array Measurements of a Rotor Ingesting a Turbulent Shear Flow. *22nd AIAA/CEAS Aeroacoustics Conference*, (AIAA 2016-2994). <https://doi.org/10.2514/6.2016-2994>
- Berkooz, G., Holmes, P., & Lumley, J. (1993). The Proper Orthogonal Decomposition in the Analysis of Turbulent Flows. *Ann. Rev. Fluid Mech.*, 25(1971), 539–575.
- Borgoltz, A. (2007). Modifications of Coherent Structures in Fan Blade Wakes for Broadband Noise Reduction. *Aerospace Engineering, Doctor of*.
- Braza, M., Perrin, R., & Hoarau, Y. (2006). Turbulence properties in the cylinder wake at high Reynolds numbers. *Journal of Fluids and Structures*, 22(6–7), 757–771. <https://doi.org/10.1016/j.jfluidstructs.2006.04.021>
- Cadel, D. R. (2016). Advanced instrumentation and measurement techniques for near surface flows.
- Cantwell, B. J. (1981). Organised Motion in Turbulent Flow. *Annual Review of Fluid Mechanics*, 13(1), 457–515. <https://doi.org/10.1146/annurev.fl.13.010181.002325>
- Devenport, W. J., Burdisso, R. A., Borgoltz, A., Ravetta, P. A., Barone, M. F., Brown, K. A., & Morton, M. A. (2013). The Kevlar-walled anechoic wind tunnel. *Journal of Sound and Vibration*, 332(17), 3971–3991. <https://doi.org/10.1016/j.jsv.2013.02.043>
- Devenport, W. J., & Glegg, S. A. L. (1999). Measurement and Modeling of the Two-Point Correlation Tensor in a Plane Wake for Broadband Noise Prediction, (May).
- Devenport, W. J., Muthanna, C., & Ma, R. (2001). Two-Point Descriptions of Wake Turbulence with Application to Noise Prediction Introduction, 39(12).
- George, W. K. (1989). The self-preservation of turbulent flows and its relation to initial conditions and coherent structures. *Advances in Turbulence*.
- George, W. K. (2012). Asymptotic Effect of Initial and Upstream Conditions on Turbulence. *Journal of Fluids Engineering*, 134(6), 61203. <https://doi.org/10.1115/1.4006561>
- Gerrard, J. H. (1966). The three-dimensional structure of the wake of a circular cylinder. *Journal of Fluid Mechanics*, 25(1), 143. <https://doi.org/10.1017/S0022112066000090>
- Glauser, M. N., Leib, S. J., & George, W. K. (1987). Coherent Structures in the Axisymmetric Jet Mixing Layer. *Turbulent Shear Flows 5*. <https://doi.org/10.1007/978-3-642-71435-1>
- Glegg, S. A. L., Devenport, W., & Alexander, N. (2015). Broadband rotor noise predictions using a time domain approach. *Journal of Sound and Vibration*, 335, 115–124.

<https://doi.org/10.1016/j.jsv.2014.09.007>

- Glegg, S., & Devenport, W. (2000). Compact eddy structures and their application to aeroacoustics. *6th Aeroacoustics Conference and Exhibit*. <https://doi.org/10.2514/6.2000-1995>
- Glegg, S., & Devenport, W. (2001). Proper Orthogonal Decomposition of Turbulent Flows for Aeroacoustic and Hydroacoustic Applications. *Journal of Sound and Vibration*, 239(4), 767–784. <https://doi.org/10.1006/jsvi.2000.3128>
- Johansson, P. S., & Andersson, H. I. (2004). Generation of inflow data for inhomogeneous turbulence. *Theoretical and Computational Fluid Dynamics*, 18(5), 371–389. <https://doi.org/10.1007/s00162-004-0147-z>
- Kirby, M., Boris, J., & Sirovich, L. (1990). An eigenfunction analysis of axisymmetric jet flow. *Journal of Computational Physics*, 90(1), 98–122. [https://doi.org/10.1016/0021-9991\(90\)90198-A](https://doi.org/10.1016/0021-9991(90)90198-A)
- Kline, S. J., Reynolds, W. C., Schraub, F. A., & Rundstatler, P. W. (1967). The structure of turbulent boundary layers. *Journal of Fluid Mechanics*, 30, 741–773. <https://doi.org/10.1017/S0022112067001740>
- Liu, J. T. C. (1986). Contributions to the Understanding of Large-Scale Coherent Structures in Developing Free Turbulent Shear Flows.
- Loeve, M. M. (1955). Probability Theory. Princeton, NJ: VanNostrand.
- Lumley, J. L. (1967). The structure of inhomogeneous turbulent flows.
- Lumley, J. L. (1989). The State of Turbulence Research. *Advances in Turbulence*.
- Marasli, B., Nguyen, P., & Wallace, J. M. (1993). A calibration technique for multiple-sensor hot-wire probes and its application to vorticity measurements in the wake of a circular cylinder. *Experiments in Fluids*, 15(3), 209–218. <https://doi.org/10.1007/BF00189888>
- Matsuzaki, K., Shingai, M., Haramoto, Y., Munekata, M., & Ohba, H. (2004). Visualization of Three-Dimensional Flow Structures in the Wake of an Inclined Circular Cylinder 2. Experimental and Numerical Method, 7(4), 309–316.
- Miranda, J. (1996). The Structure of a Trailing Vortex Wake.
- Moser, R. D., Rogers, M. M., & Ewing, D. W. (1998). Self-similarity of time-evolving plane wakes. *Journal of Fluid Mechanics*, 367, 255–289. <https://doi.org/10.1017/S0022112098001426>
- Neumann, M., Shirai, K., Büttner, L., & Czarske, J. (2009). Two-point correlation estimation of turbulent shear flows using a novel laser Doppler velocity profile sensor. *Flow Measurement and Instrumentation*, 20(6), 252–263. <https://doi.org/10.1016/j.flowmeasinst.2009.09.001>
- Ong, L., & Wallace, J. M. (1996). The velocity field of the turbulent very near wake of a circular cylinder. *Experiments in Fluids*, 20(6), 441–453. <https://doi.org/10.1007/BF00189383>
- Payne, F. R., & Lumley, J. L. (1967). Large Eddy Structure of the Turbulent Wake behind a

- Circular Cylinder. *Physics of Fluids*, 10(9), S194. <https://doi.org/10.1063/1.1762445>
- Roshko, A. (1954). On the development of turbulent wakes from vortex streets. *Development*.
- Roshko, A. (1977). Structure of Turbulent Shear Flows: A New Look. *AIAA Journal*, 15(5), 0768c–0768c. <https://doi.org/10.2514/3.60704>
- Stanislav, G. (2006). POD, LSE, and Wavelet decomposition: Literature Review, (2), 2–5. <https://doi.org/10.1002/pssb.201300062>
- Tang, S. L., Antonia, R. A., Djenidi, L., & Zhou, Y. (2016). Complete self-preservation along the axis of a circular cylinder far wake. *Journal of Fluid Mechanics*, 786(November), 253–274. <https://doi.org/10.1017/jfm.2015.663>
- Townsend, A. A. (1979). Flow Patterns of Large Eddies in a Wake and in a Boundary Layer. *Journal of Fluid Mechanics*, 95(1979).
- Waclawczyk, M., & Pozorski, J. (2002). Two point velocity statistics and the POD analysis of the near-wall region in a turbulent channel flow. *Journal of Theoretical and Applied Mechanics*.
- Wang, H. F., Cao, H. L., & Zhou, Y. (2014). POD analysis of a finite-length cylinder near wake. *Experiments in Fluids*, 55(8). <https://doi.org/10.1007/s00348-014-1790-9>
- Wang, J., Wang, K., & Wang, M. (2016). Computation of the Noise of Rotor Interaction with a Turbulent Wake. *22nd AIAA/CEAS Aeroacoustics Conference*, 1–13. <https://doi.org/10.2514/6.2016-2998>
- Wittmer, K., Devenport, W. J., & Zsoldos, J. S. (1998). A four-sensor hot-wire probe system for three-component velocity measurement. *Experiments in Fluids*, 24(5–6), 416–423. <https://doi.org/10.1007/s003480050191>
- Wynagnanski, I., Champagne, F., & Marasli, B. (1986). On the large-scale structures in two-dimensional, small-deficit, turbulent wakes. *Journal of Fluid Mechanics*, 168, 31–71. <https://doi.org/10.1017/S0022112086000289>

Appendix A: Accessing the Two-Point Correlation Function

A large part of the data reduction effort was to express the two-point correlation in a compact form for use in acoustic prediction methods. The two-point time delay correlation has been reduced to a single Matlab variable for easy access. The correlation is of the form, $R_{ij}(i, j, \tau, \Delta z, y, \Delta y)$. The variables i and j define the index of velocity components of the the fixed and moving probes respectively for which the correlation is desired. The variable τ is the time delay and y is the fixed probe position, also defined as the anchor point for the correlation. The variable Δz is the separation between the fixed and moving probes and is defined as, $\Delta z = z' - z$ where the primed variable denotes the moving probe position. The Δy variable defines the separation position between the fixed and moving probes and is defined as, $\Delta y = y' - y$. A Matlab function was created to interpolate the correlation for any combination of variables. The inputs are normalized on the wake variables U_{ref} and L_w . The positions are each input normalized on L_w while τ is normalized as, $\tau U_{ref}/L_w$. For efficient interpolation, the Matlab code converts each input array into indices. The function is included below.

```

function a = cylinder_corr(ruij, ii, jj, y, dy, dz, dt)
% Interpolates the two point correlation tensor at points specified in terms
% of normalized wake variables
% ruij [3 3 65 43 10 85], Correlation tensor; indices represent respectively
%           index of velocity component at y, 0
%           index of velocity component at y+dy, dz
%           transformed integer time delay alpha, alpha=33 for zero time delay
%           transformed integer spanwise separation gamma, gamma=1 for zero dz
%           integer spanwise position delta, delta=1 for zero y
%           transformed integer normal separation beta, beta=21 for zero dy

% i, scalar index of velocity component at y, 0
% j, scalar index of velocity component at y+dy, dz
% y, array of normal positions (in wake half thicknesses Lw) for which correlations are desired
%     -3.44<y/Lw<3.44 Out of range values return NaN.
% dy, array of normal separations (in wake half thicknesses Lw) at which correlations are desired
%     -4.0135<dy/Lw<4.0135. Out of range values return NaN.
% dz, array of spanwise separations (in wake half thicknesses Lw) at which correlations are
%     desired
%     -3.5<dz/Lw<3.5. Out of range values return NaN.
% dt, array of time delays (in Lw/Uinf) at which correlations are desired
%     -8<dtUinf/Lw<8. Out of range values return NaN.

% Determine the sign of the anchor point, y
ysign = sign(y);

% Time delay index
alpha=sign(dt). *sqrt(abs(dt. /8)). *32+33;

% dy index, reverse sign of index if y is positive
beta=sign(dy. *ysign). *(abs(dy. /4. 0135)). *42+43;

% dz index, ignores sign of dz
gamma=sign(dz). *(abs(dz. /3. 4401)). *21+22;

% y index, ignores sign of y
delta=abs(y)/0. 3822+1;

temp = squeeze(ruij(ii, jj, :, :, :, :));
a = interpn(temp, alpha, gamma, delta, beta);
a(isnan(a)) = 0;

% If i or j is 2 (as in uv, vw, vu, wv) and y is negative, reverse sign of correlation
if (ii==2 || jj==2) && ~(jj==2 && ii==2)
    a=a. *ysign;
end

% Output the correlation
a = squeeze(a);

```


Appendix B: The Correction of the Open Circuit Wind Tunnel Reynolds Stress Profiles

In this appendix, the results of the correction for the angle sensitivity of the two quad-hotwire probes used in the two-point measurement are presented. The method and justification for correcting the data measured with the two probes is included in Section 3.2.8. Figure and Figure show the Reynolds stress profiles for each grid point in a single measurement grid. The data measured in the OCWT facility is plotted as colored circles while the profiles measured in the SWT facility when the probes were not misaligned with the freestream are plotted as solid black lines. Figure and Figure show the data measured in the OCWT facility with the correction for the probe angle sensitivity applied. Figure and Figure show the data measured using the fixed probe again with the profiles measured in the SWT as solid black lines before any corrections have been applied. The stress profiles for the fixed probe were created by averaging the data measured at each fixed probe location in the wake. Figure and Figure show the fixed probe profiles after the correction has been applied.

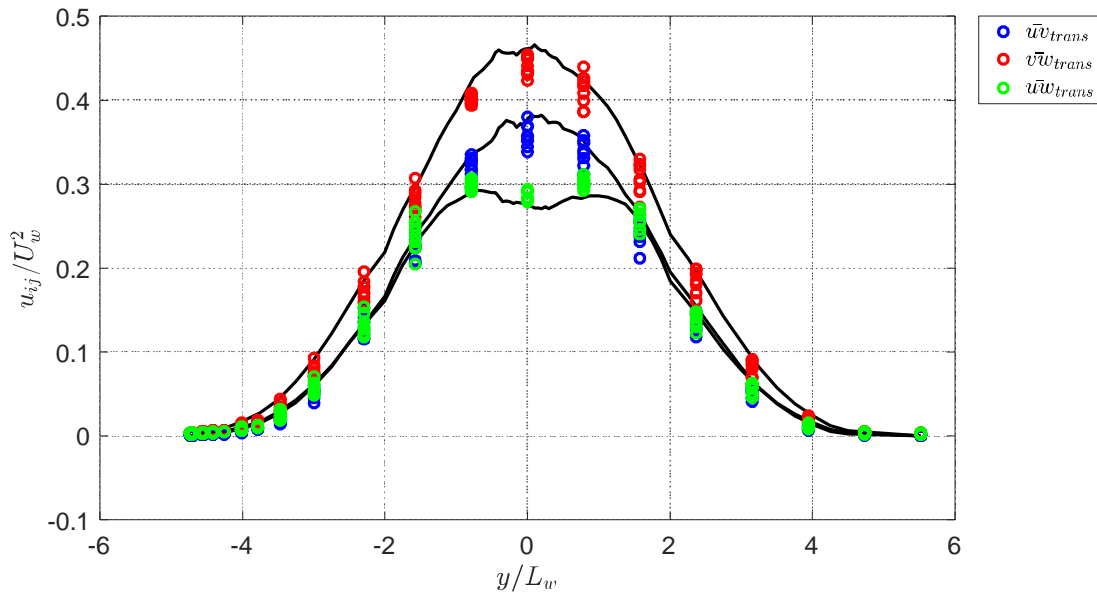


Figure B.1. Comparison between scaled OCWT and SWT normal Reynolds stress profiles.

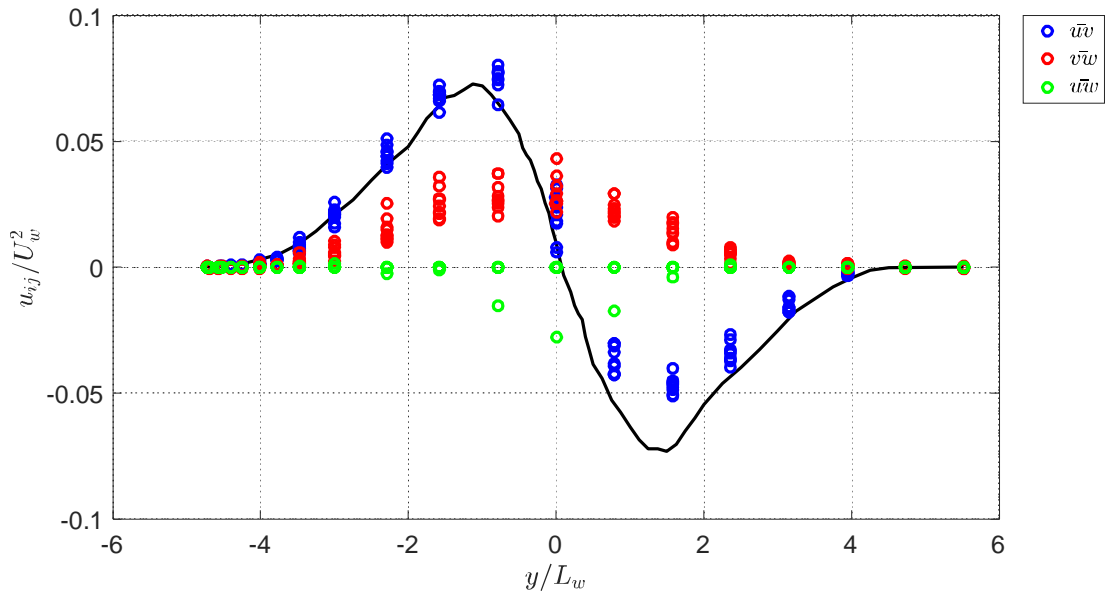


Figure B.2. Comparison between scaled OCWT and SWT cross stress profiles.

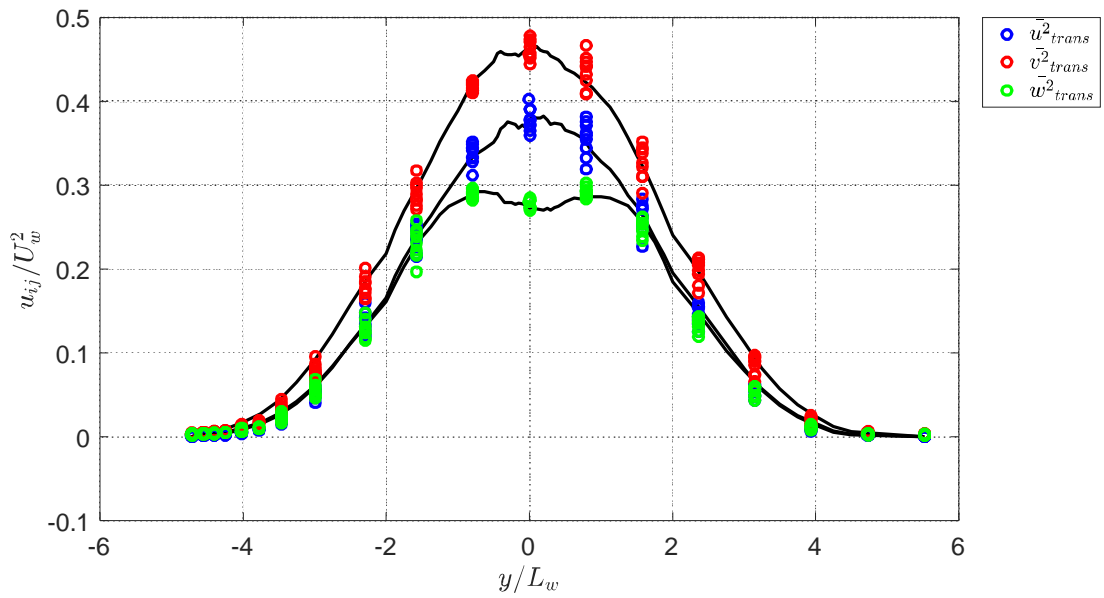


Figure B.3. Transformed OCWT normal stress profiles.

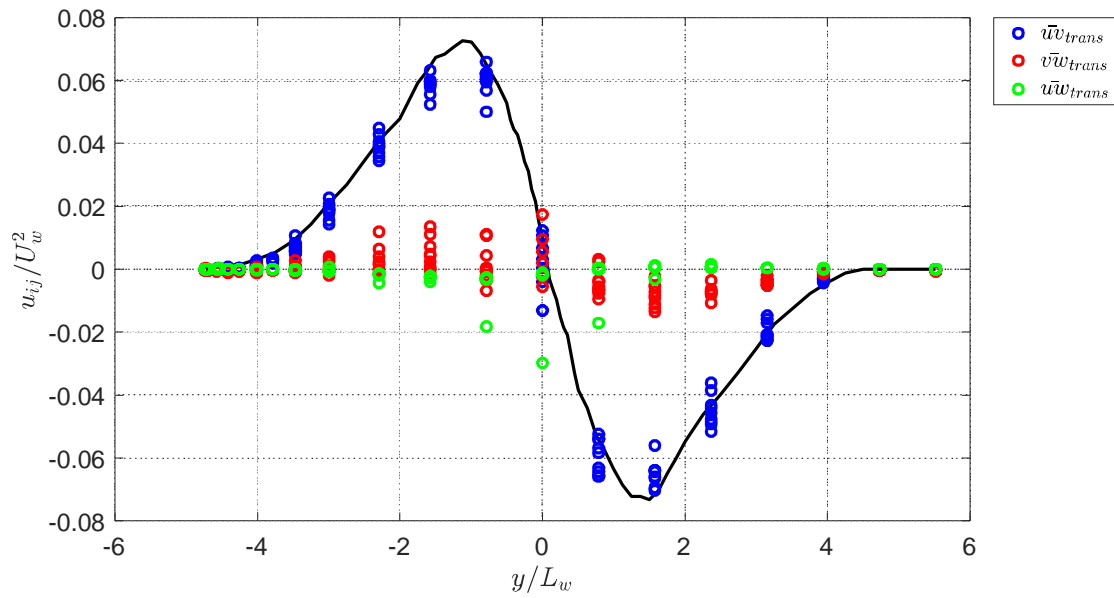


Figure B.4. Transformed OCWT cross stress profiles.

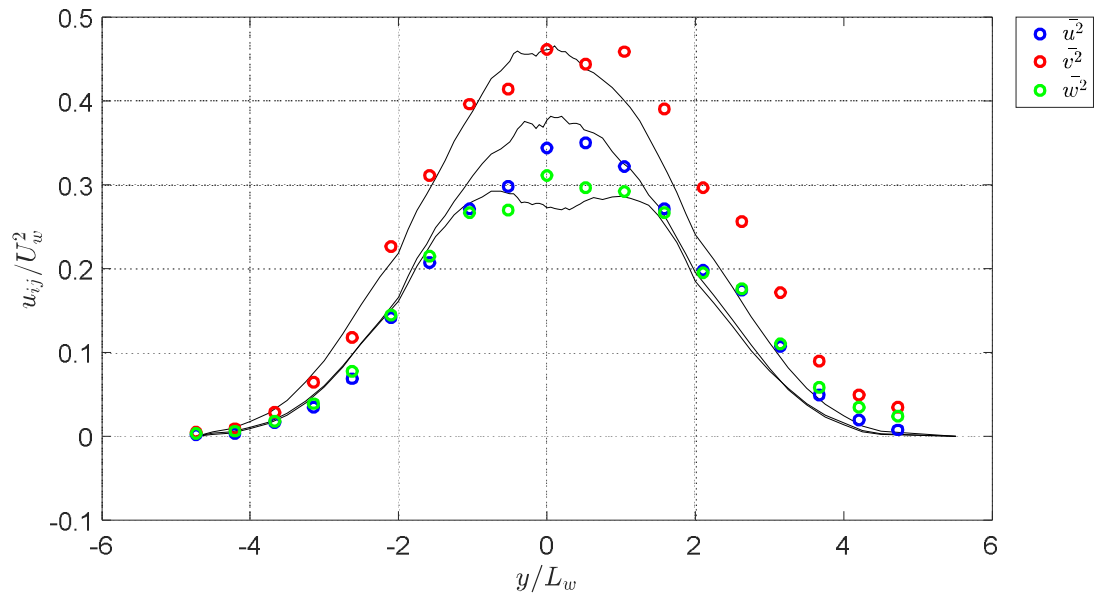


Figure B.5. Comparison between scale OCWT and SWT normal Reynolds stress profiles for the fixed probe.

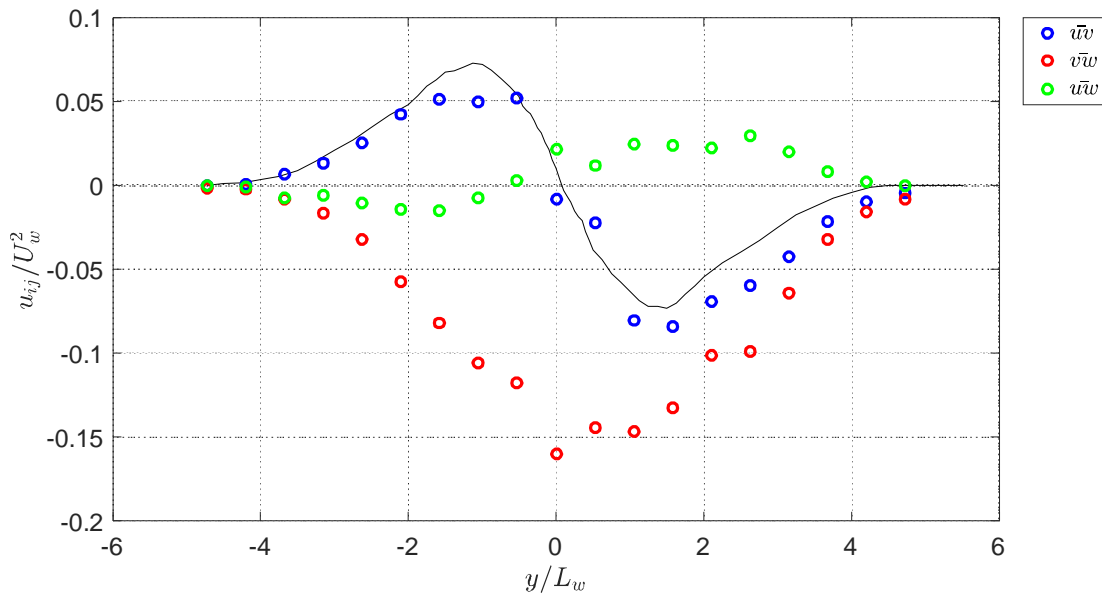


Figure B.6. Comparison between scale OCWT and SWT cross stress profiles for the fixed probe.

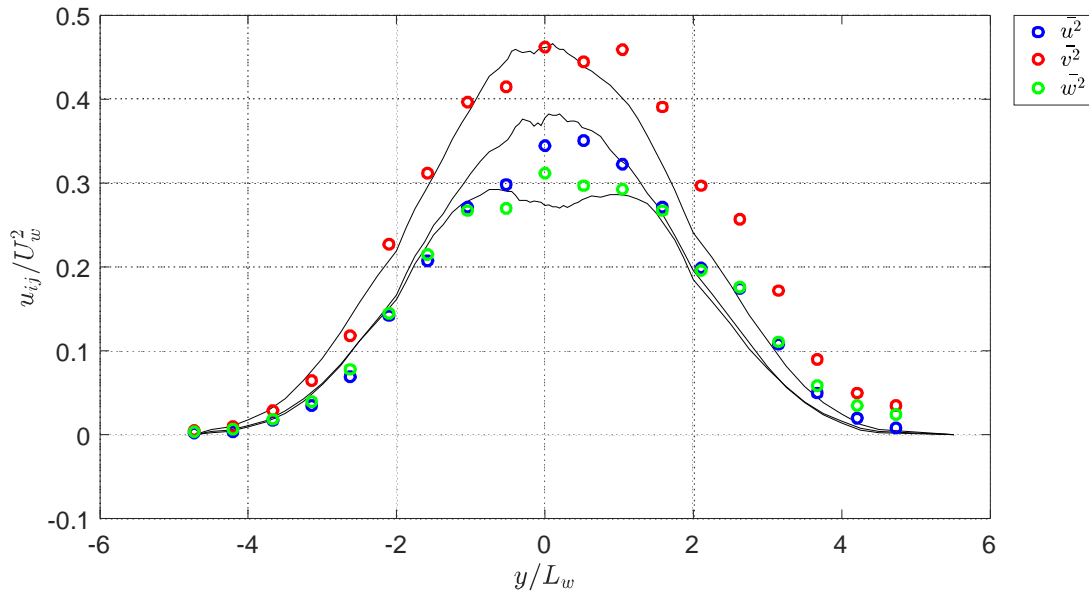


Figure B.7. Transformed OCWT normal Reynolds stresses for the fixed probe.

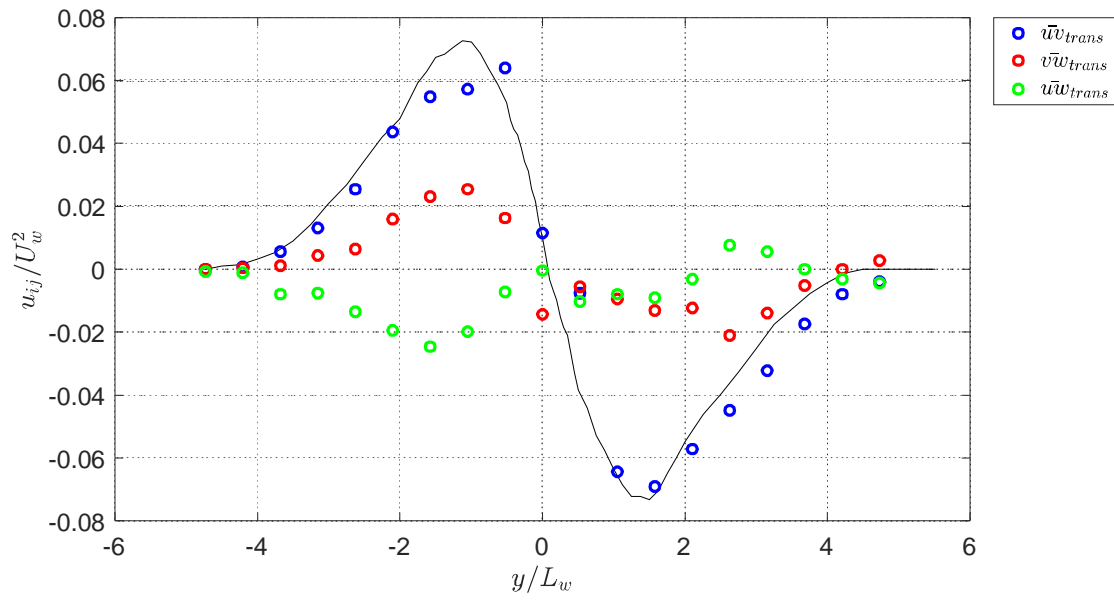


Figure B.8. Transformed OCWT cross stresses for the fixed probe.

Appendix C: Complete Set of Cylinder and Airfoil Two-Point Correlation Comparisons

After the complete reduction of the two-point correlation function in both the cylinder and airfoil wakes, an infinite combination of correlations can be plotted for different combinations of time delay and anchor point. In this appendix, comparisons in the two-point correlation between the two wakes are presented for fixed probe positions from 0 to $2.5 y/L_w$ in increments of $0.5 y/L_w$ at zero time delay. The discussion in Section 3.3.3 also applies to the comparisons plotted in this Appendix. The structure of the correlation function components is similar for both wakes. For each of the comparisons the magnitude of the correlations in the cylinder wake are always significantly larger than those in the airfoil wake. There is also significant correlation between probes at greater y and z separations in the cylinder wake than seen in the airfoil wake. In both wakes the two point correlation has been normalized on the deficit velocity squared and the positions have been normalized on the half wake width.

There is significant difference in the correlation structures of the two wakes for a fixed probe located at $y/L_w = 2.5$. These comparisons are shown in Section C.6. The differences seen here are attributed to the fact that the width of airfoil wake is less than that of the cylinder wake. At this fixed probe location in the cylinder wake the fixed probe is located at a position in the wake with significant, nonzero, Reynolds stresses where in the airfoil wake the Reynolds stresses are near zero. In the airfoil wake at this location the fixed probe is effectively outside of the edge of the wake. This causes there to be higher correlation values in the cylinder wake where then airfoil wake is weakly correlated. The comparisons also show that the correlation structure in the airfoil wake is noticeably different from the structure of the cylinder wake in some of the correlation components.

C.1 Zero Time Delay Correlation Comparison for an Anchor Point of $y/L_w = 0$

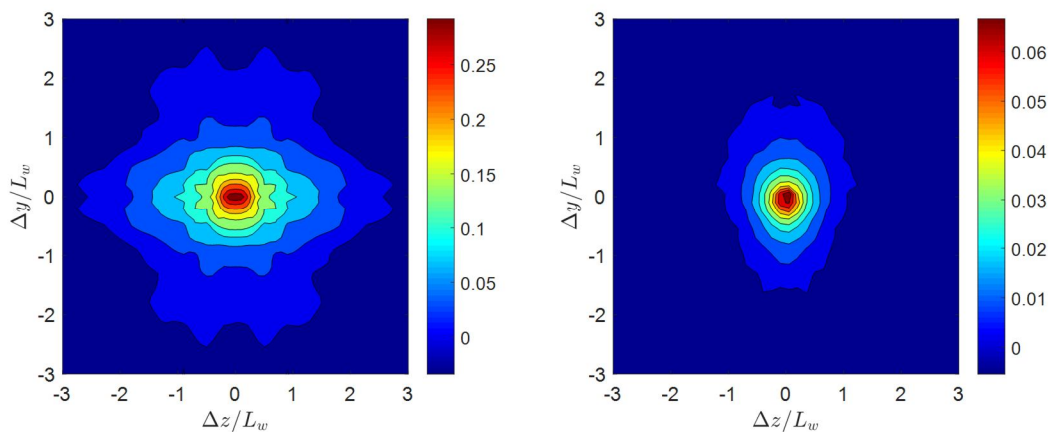


Figure C.1. R_{11} correlation comparison between the cylinder (left) and airfoil (right) wakes.

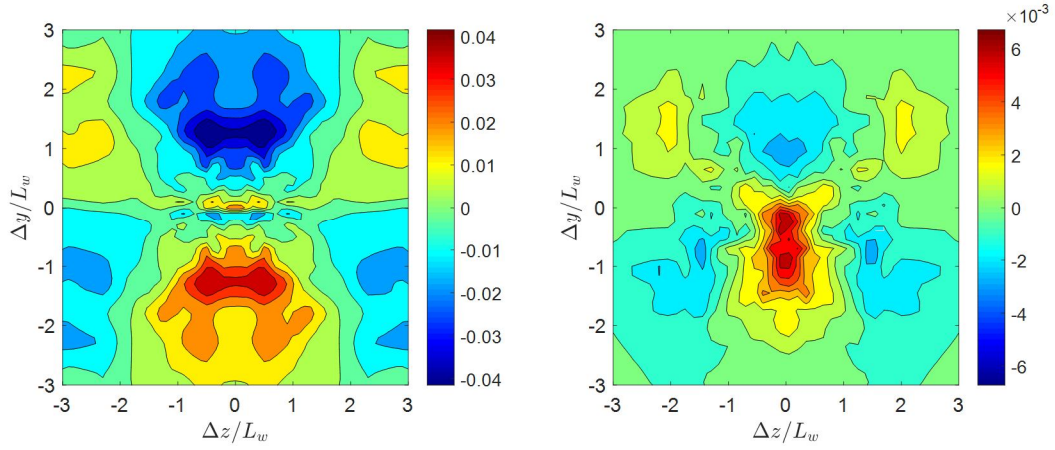


Figure C.2. R_{12} correlation comparison between the cylinder (left) and airfoil (right) wakes.

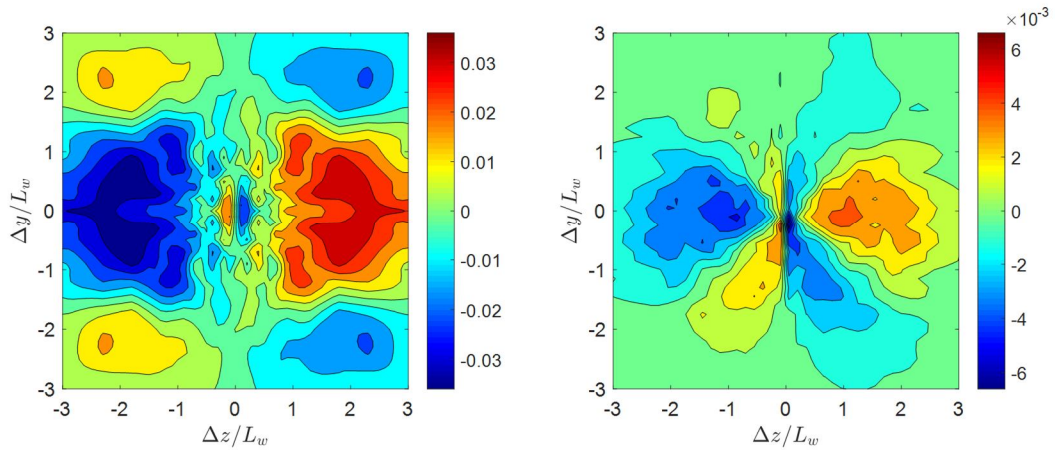


Figure C.3. R_{13} correlation comparison between the cylinder (left) and airfoil (right) wakes.

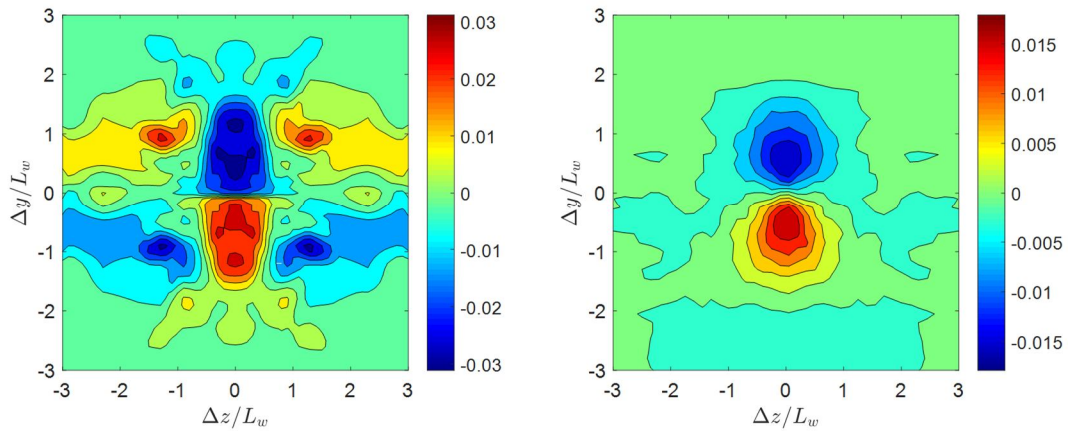


Figure C.4. R_{21} correlation comparison between the cylinder (left) and airfoil (right) wakes.

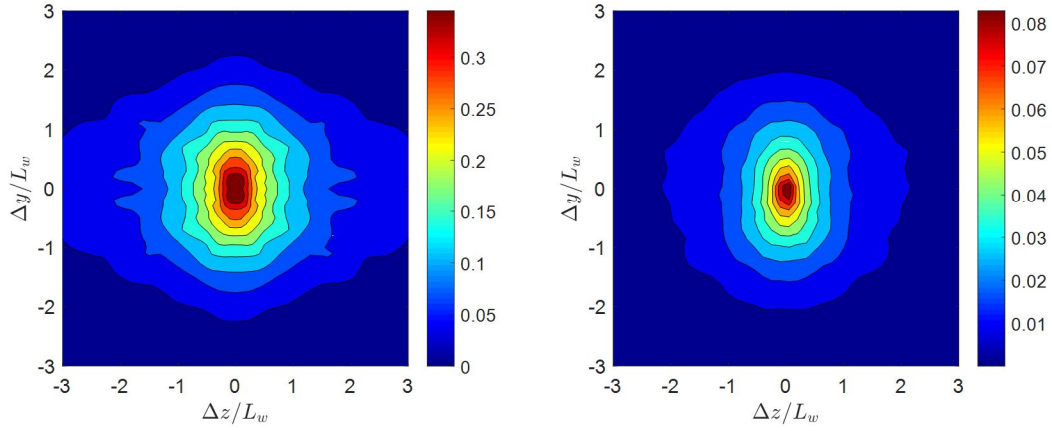


Figure C.5. R_{22} correlation comparison between the cylinder (left) and airfoil (right) wakes.

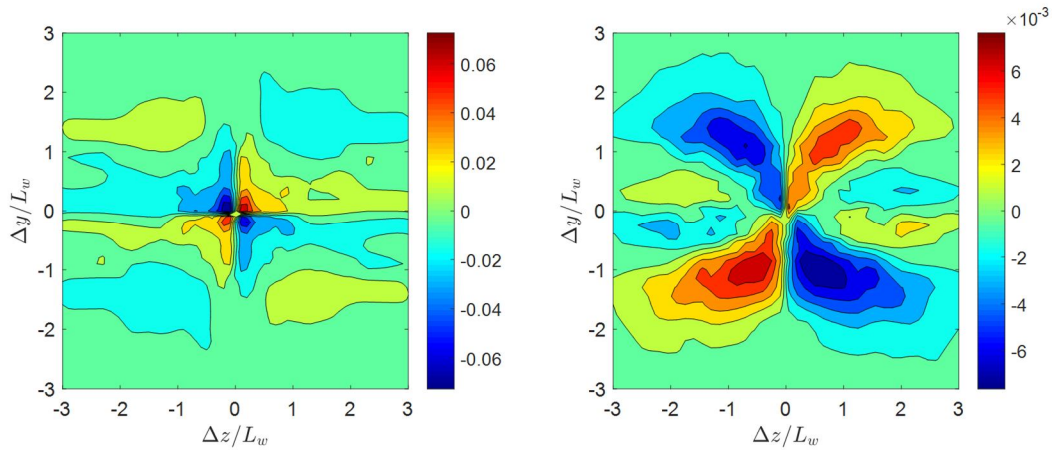


Figure C.6. R_{23} correlation comparison between the cylinder (left) and airfoil (right) wakes.

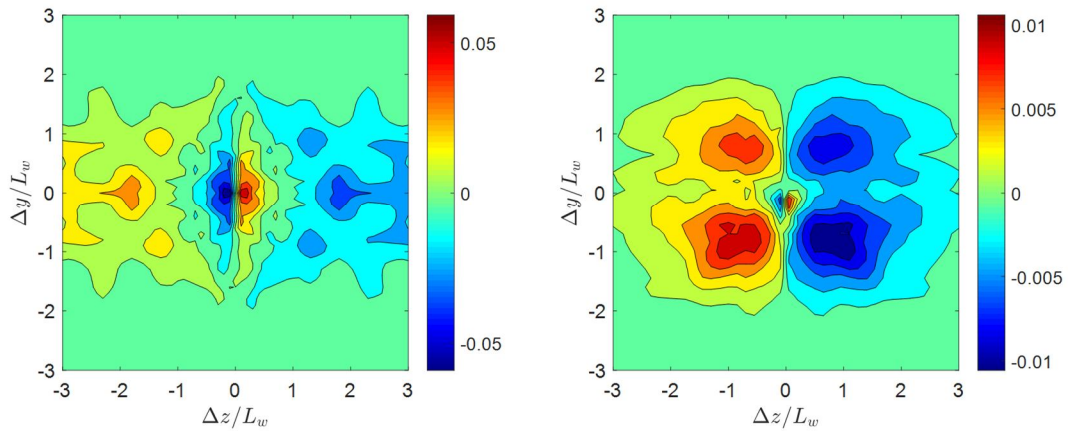


Figure C.7. R_{31} correlation comparison between the cylinder (left) and airfoil (right) wakes.

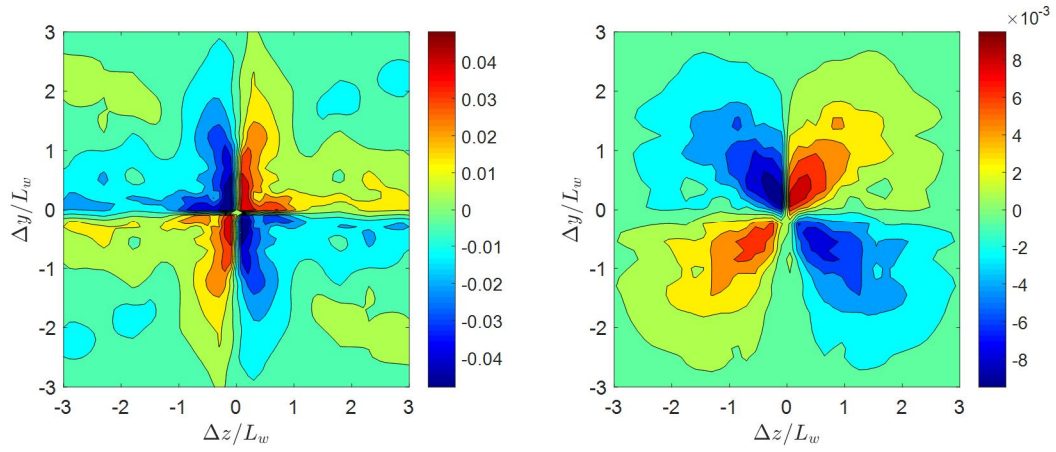


Figure C.8. R_{32} correlation comparison between the cylinder (left) and airfoil (right) wakes.

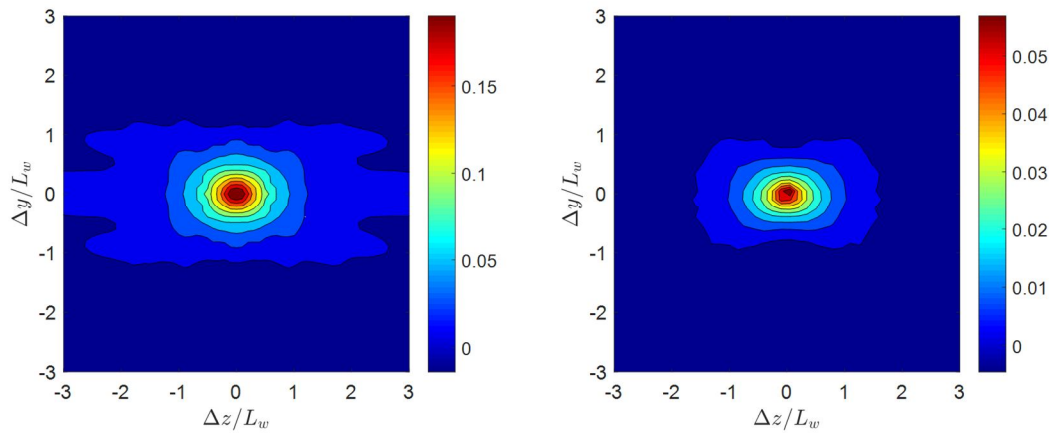


Figure C.9. R_{33} correlation comparison between the cylinder (left) and airfoil (right) wakes.

C.2 Zero Time Delay Correlation Comparison for an Anchor Point of $y/L_w = 0.5$

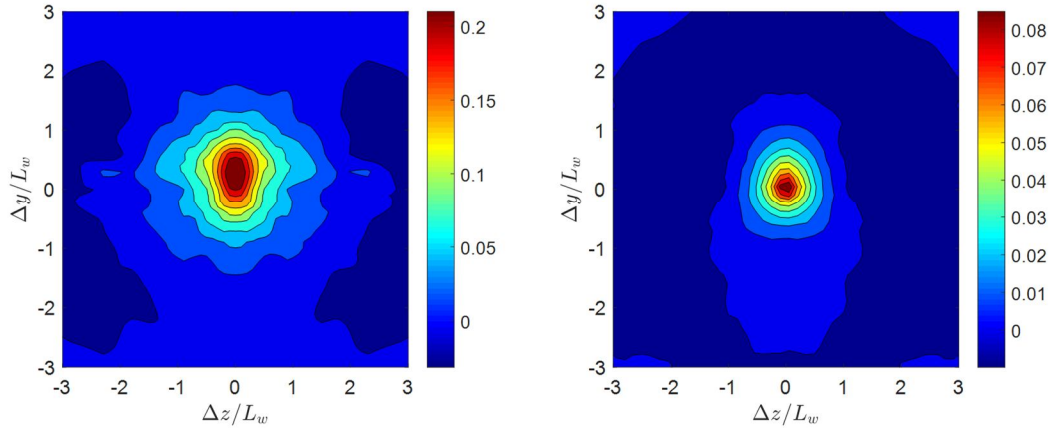


Figure C.10. R_{11} correlation comparison between the cylinder (left) and airfoil (right) wakes.

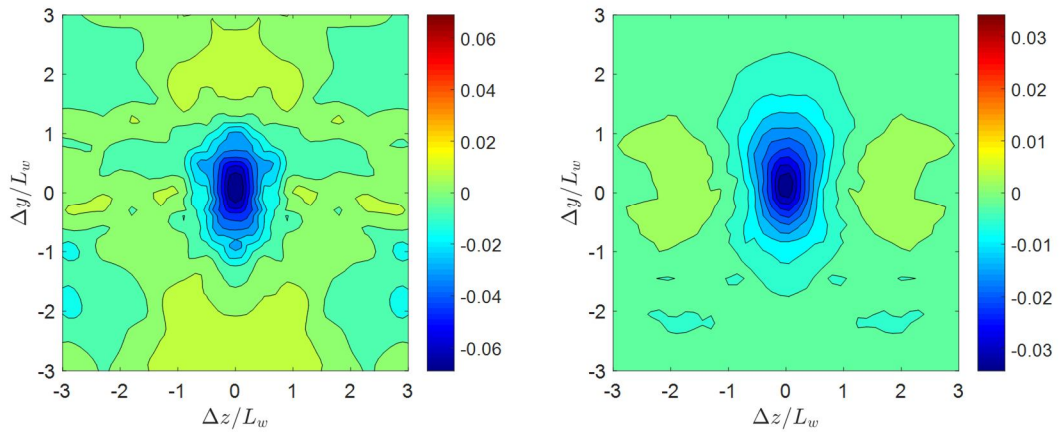


Figure C.11. R_{12} correlation comparison between the cylinder (left) and airfoil (right) wakes.

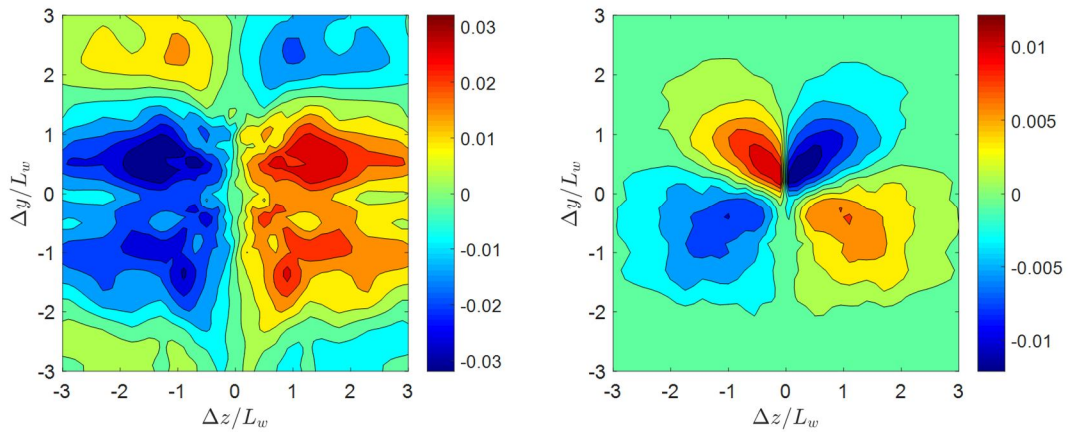


Figure C.12. R_{13} correlation comparison between the cylinder (left) and airfoil (right) wakes.

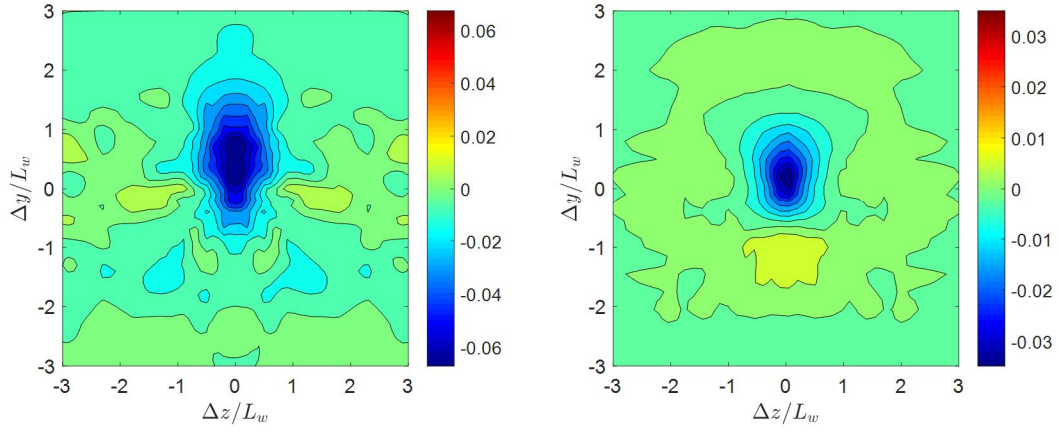


Figure C.13. R_{21} correlation comparison between the cylinder (left) and airfoil (right) wakes.

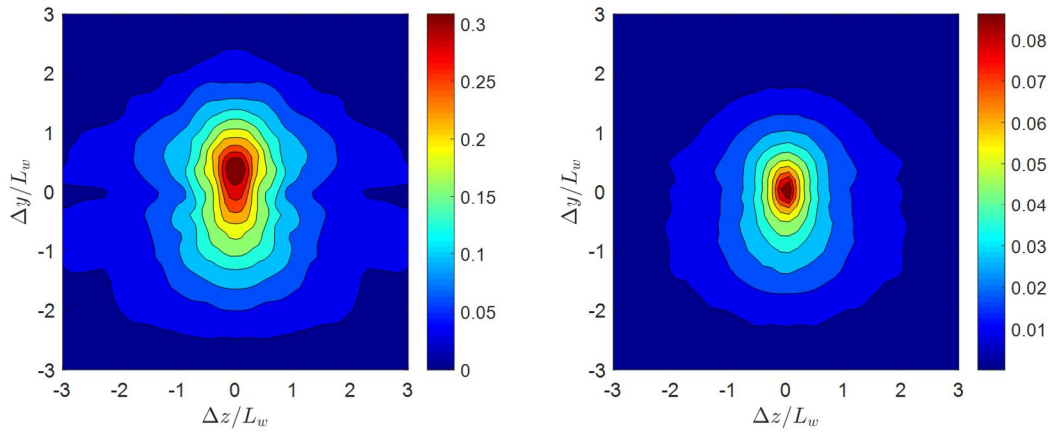


Figure C.14. R_{22} correlation comparison between the cylinder (left) and airfoil (right) wakes.

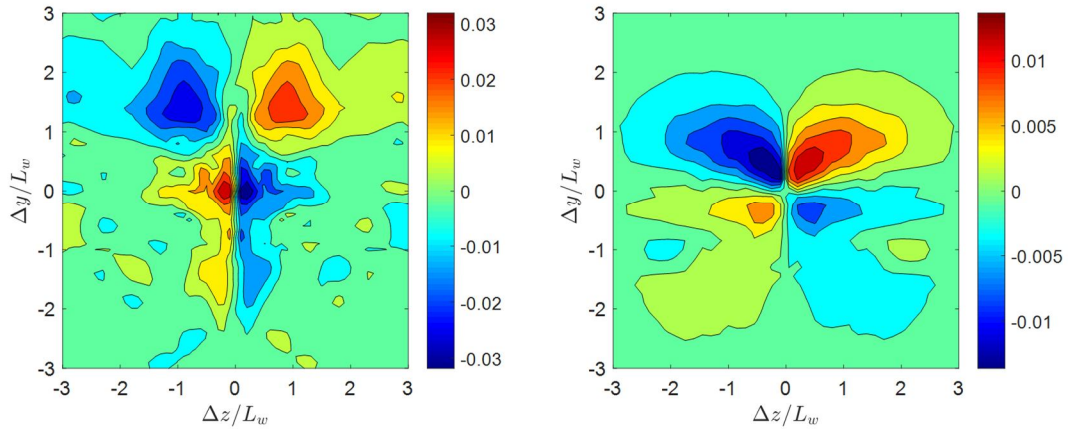


Figure C.15. R_{23} correlation comparison between the cylinder (left) and airfoil (right) wakes.

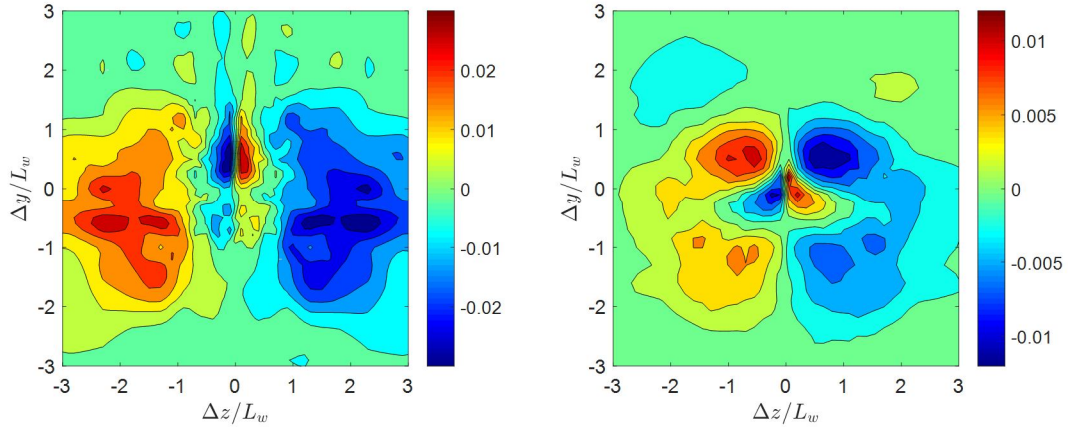


Figure C.16. R_{31} correlation comparison between the cylinder (left) and airfoil (right) wakes.

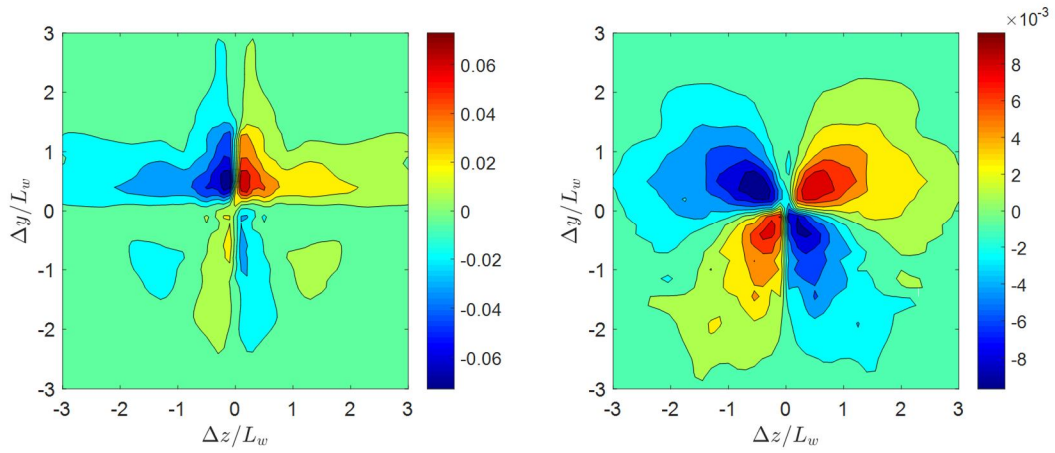


Figure C.17. R_{32} correlation comparison between the cylinder (left) and airfoil (right) wakes.

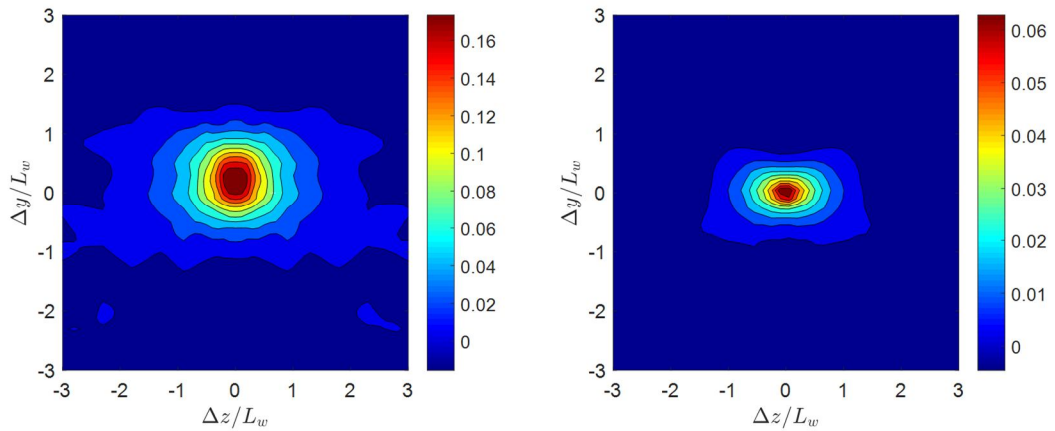


Figure C.18. R_{33} correlation comparison between the cylinder (left) and airfoil (right) wakes.

C.3 Zero Time Delay Correlation Comparison for an Anchor Point of $y/L_w = 1$

The correlation comparisons for $y/L_w = 1$ are discussed in Section 3.3.3.

C.4 Zero Time Delay Correlation Comparison for an Anchor Point of $y/L_w = 1.5$

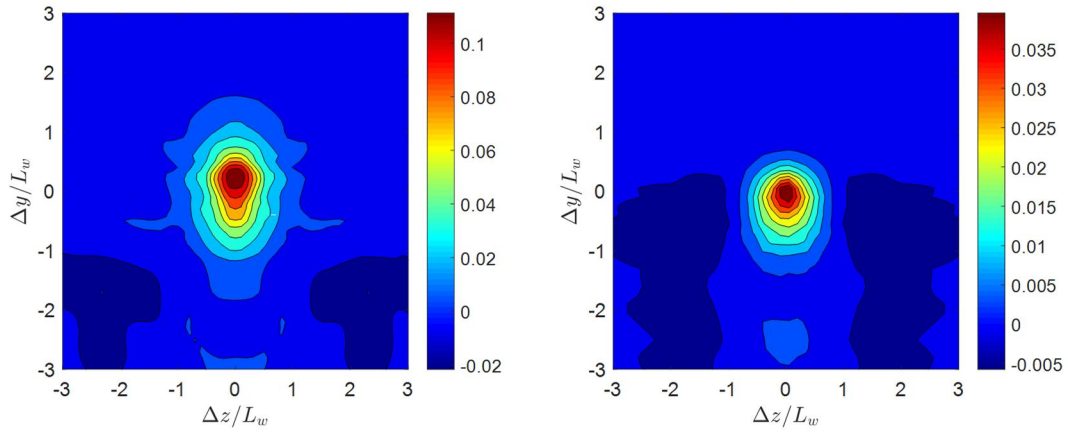


Figure C.19. R_{11} correlation comparison between the cylinder (left) and airfoil (right) wakes.

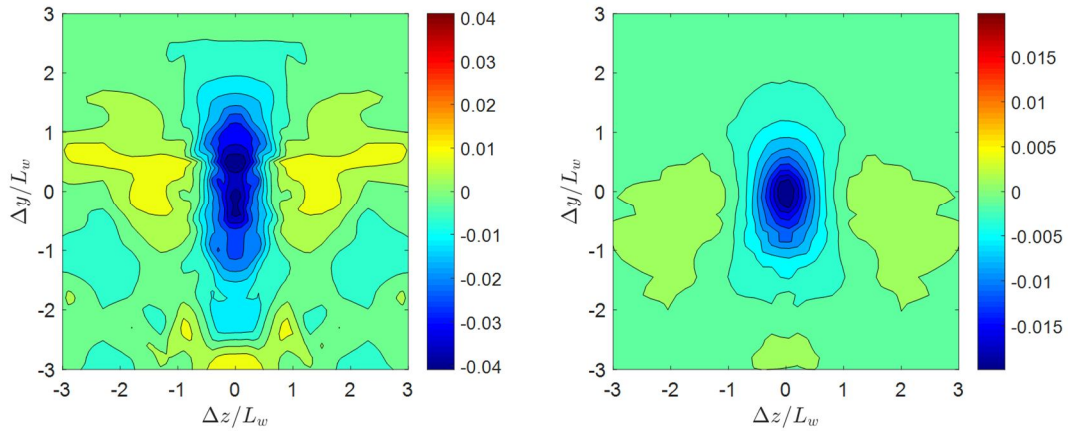


Figure C.20. R_{12} correlation comparison between the cylinder (left) and airfoil (right) wakes.

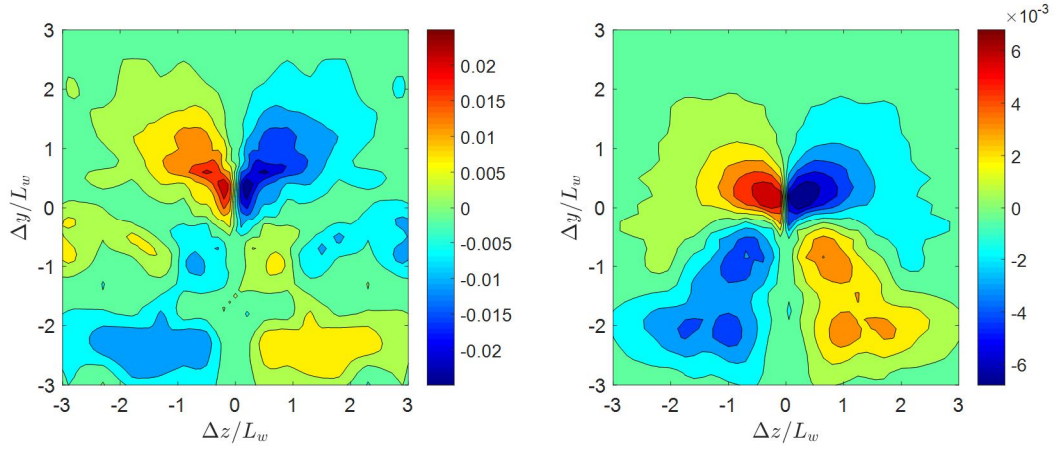


Figure C.21. R_{13} correlation comparison between the cylinder (left) and airfoil (right) wakes.

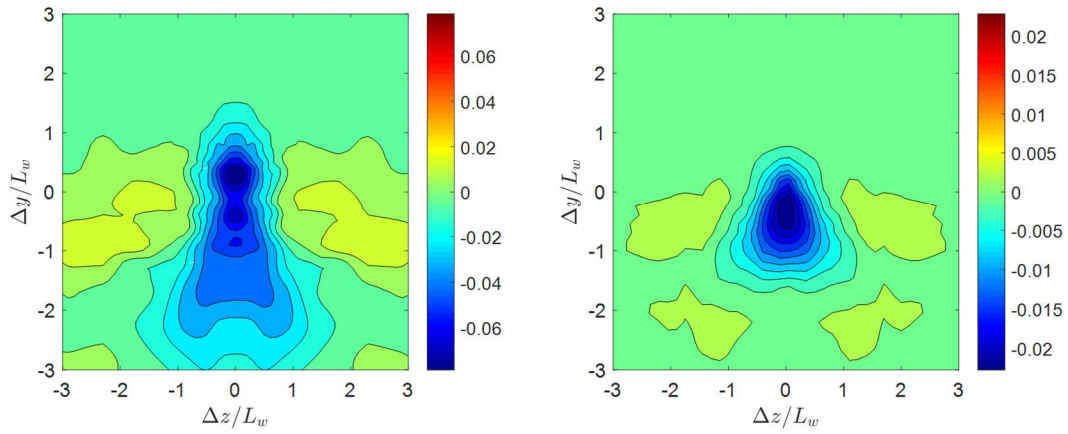


Figure C.22. R_{21} correlation comparison between the cylinder (left) and airfoil (right) wakes.

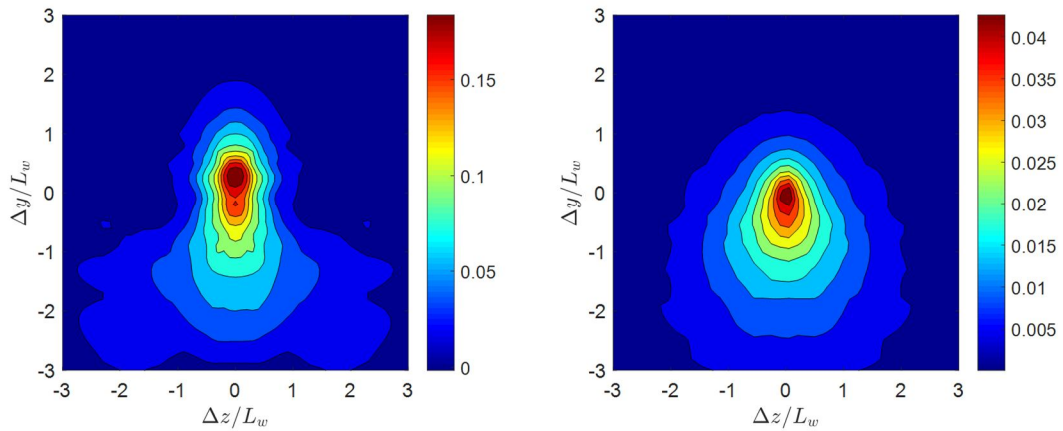


Figure C.23. R_{22} correlation comparison between the cylinder (left) and airfoil (right) wakes.

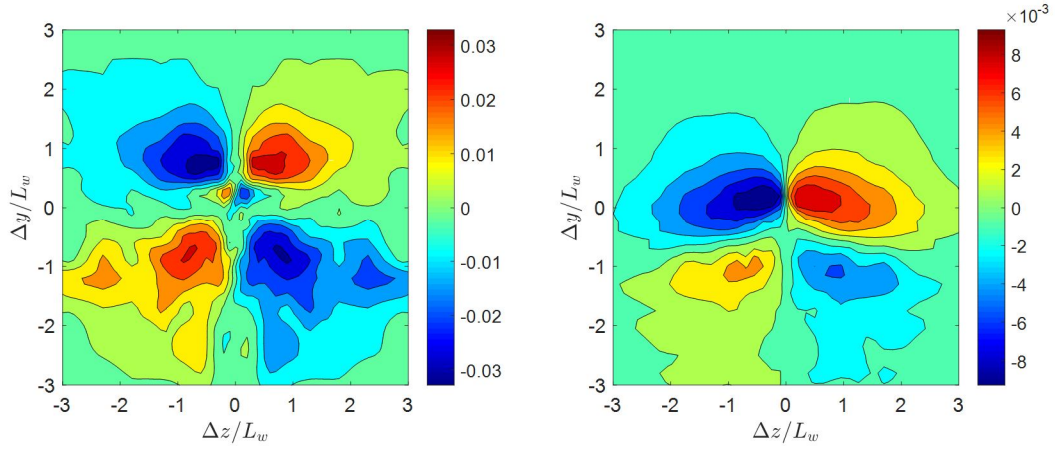


Figure C.24. R_{23} correlation comparison between the cylinder (left) and airfoil (right) wakes.

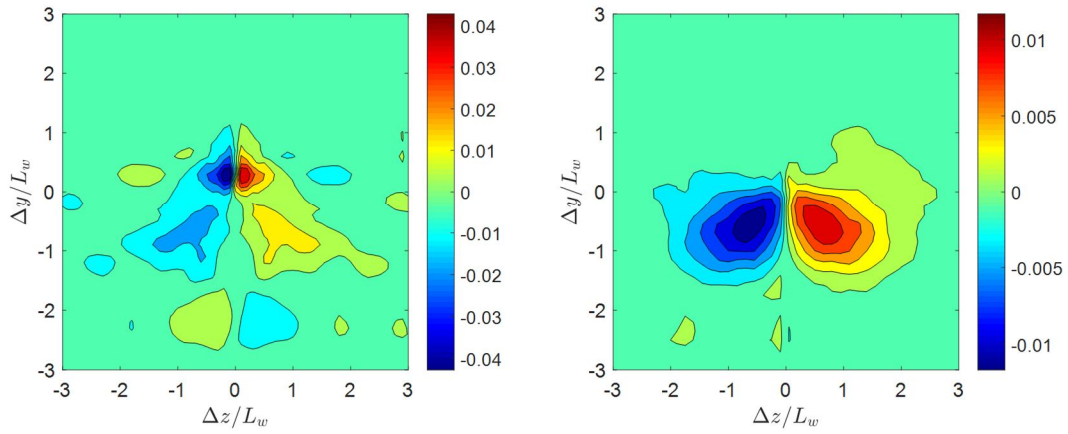


Figure C.25. R_{31} correlation comparison between the cylinder (left) and airfoil (right) wakes.

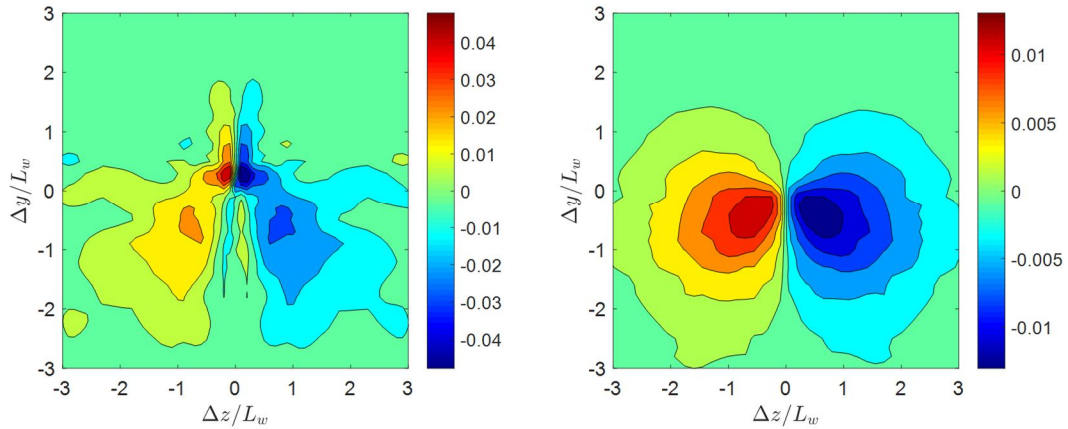


Figure C.26. R_{32} correlation comparison between the cylinder (left) and airfoil (right) wakes.

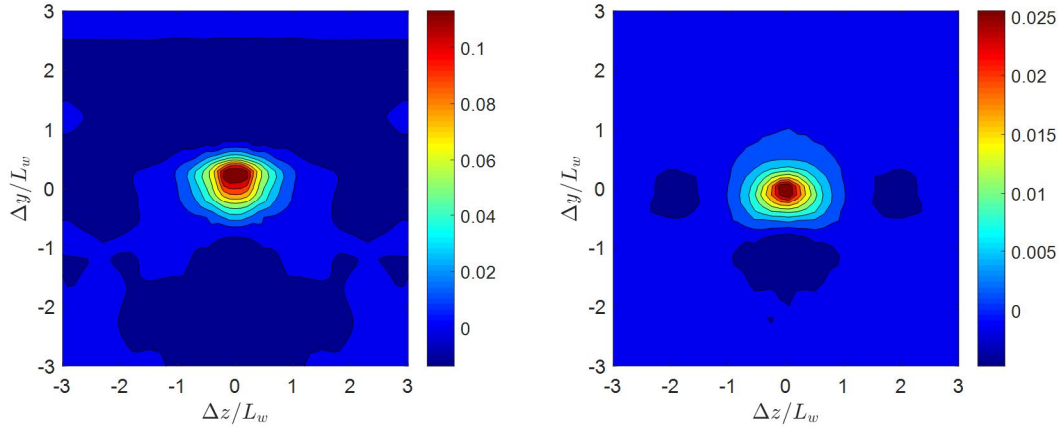


Figure C.27. R_{33} correlation comparison between the cylinder (left) and airfoil (right) wakes.

C.5 Zero Time Delay Correlation Comparison for an Anchor Point of $y/L_w = 2$

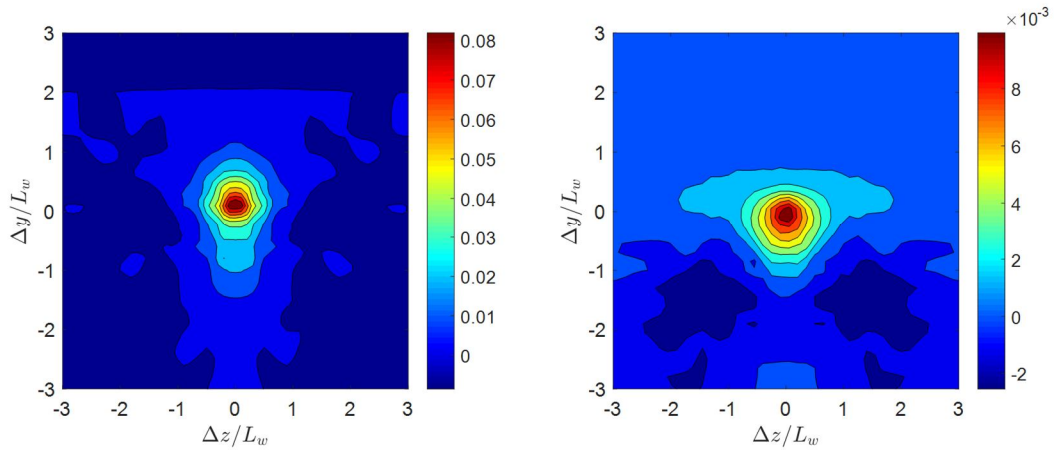


Figure C.28. R_{11} correlation comparison between the cylinder (left) and airfoil (right) wakes.

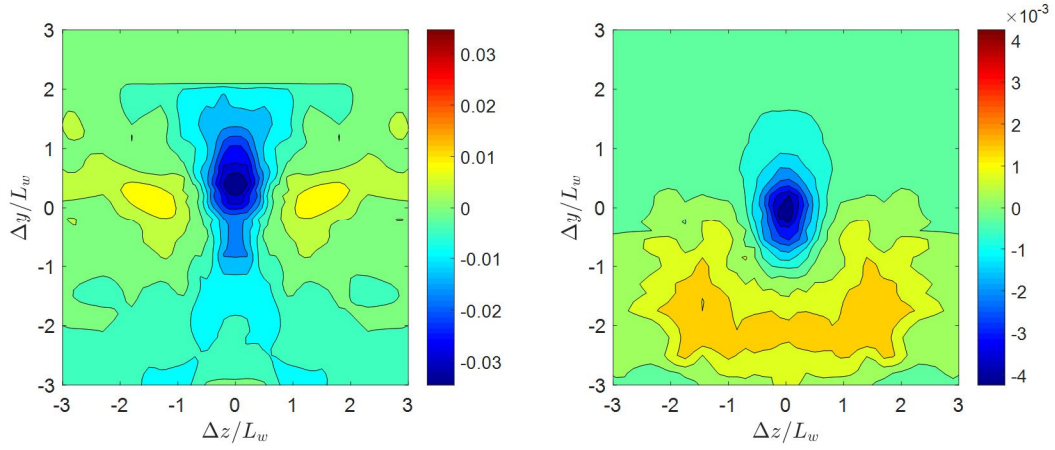


Figure C.29. R_{12} correlation comparison between the cylinder (left) and airfoil (right) wakes.

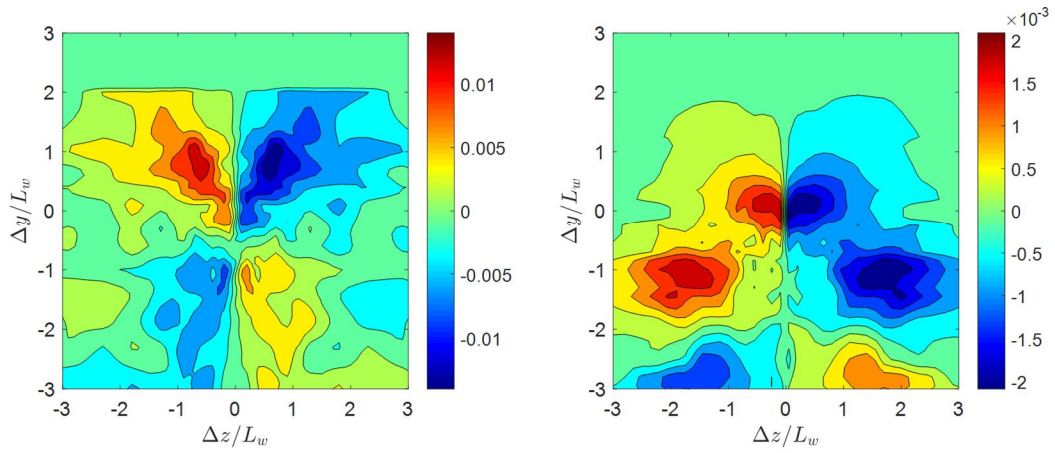


Figure C.30. R_{13} correlation comparison between the cylinder (left) and airfoil (right) wakes.

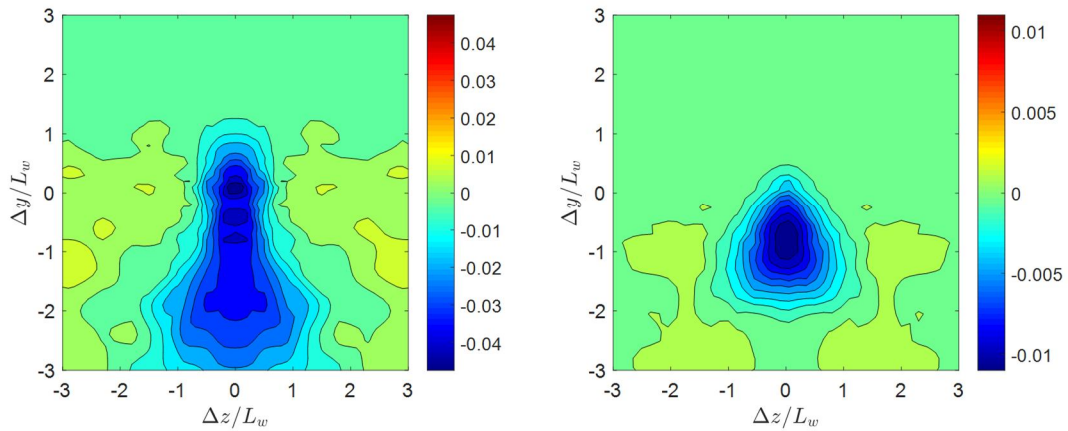


Figure C.31. R_{21} correlation comparison between the cylinder (left) and airfoil (right) wakes.

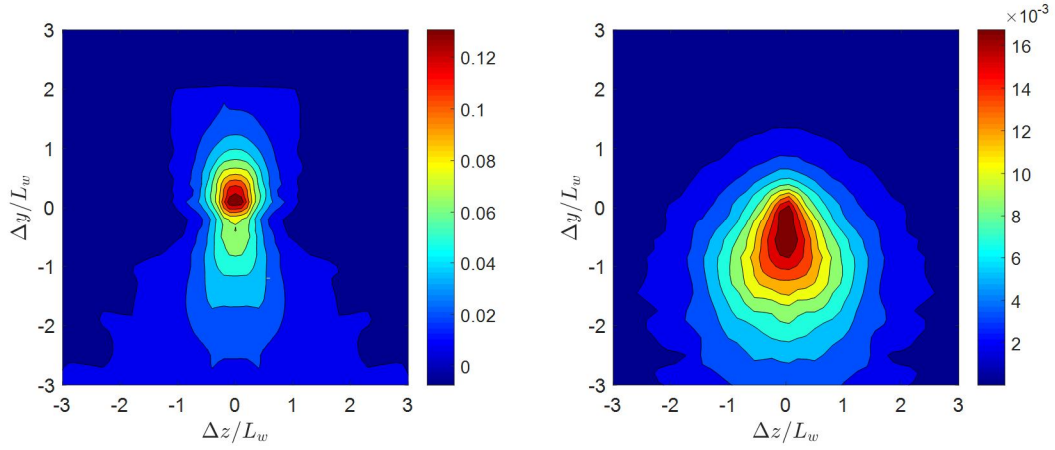


Figure C.32. R_{22} correlation comparison between the cylinder (left) and airfoil (right) wakes.

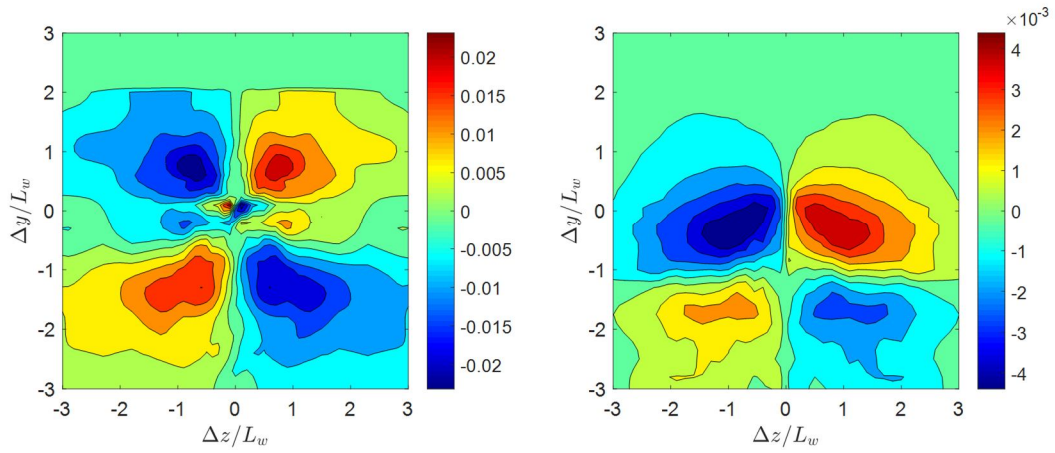


Figure C.33. R_{23} correlation comparison between the cylinder (left) and airfoil (right) wakes.

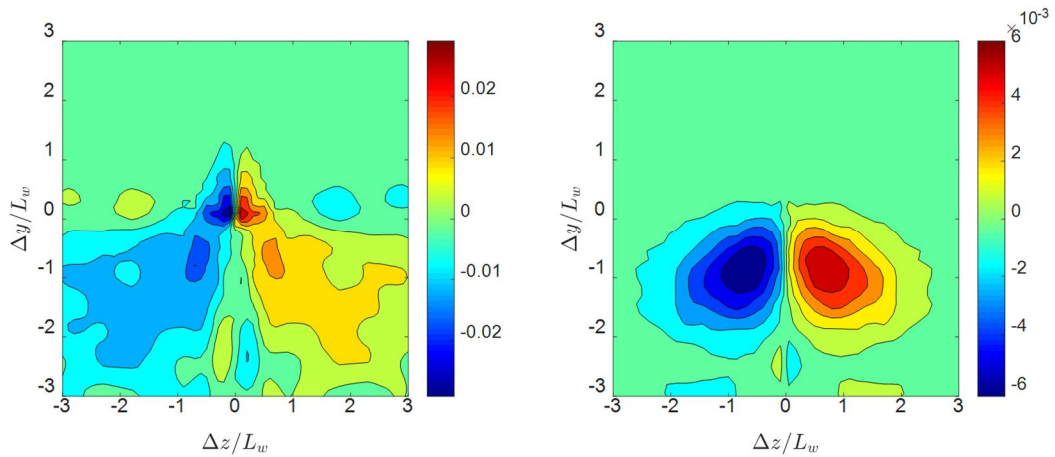


Figure C.34. R_{31} correlation comparison between the cylinder (left) and airfoil (right) wakes.

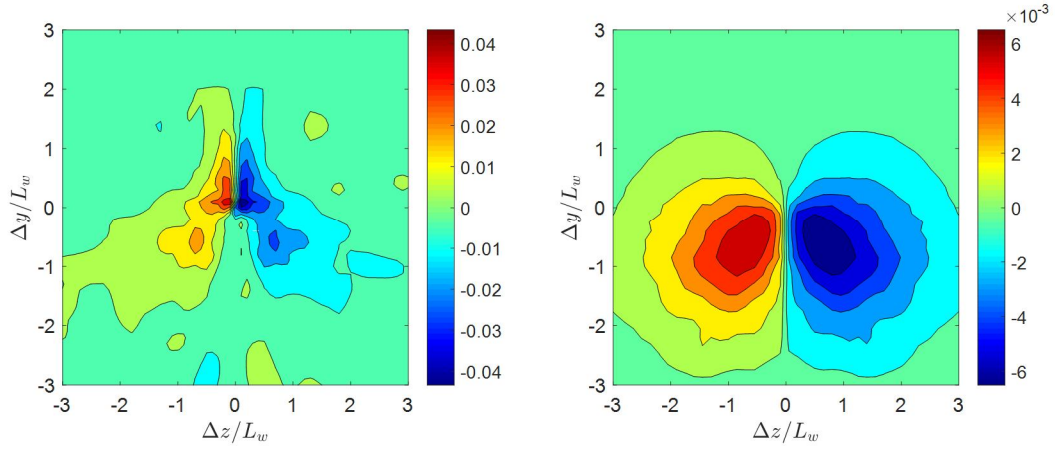


Figure C.35. R_{32} correlation comparison between the cylinder (left) and airfoil (right) wakes.

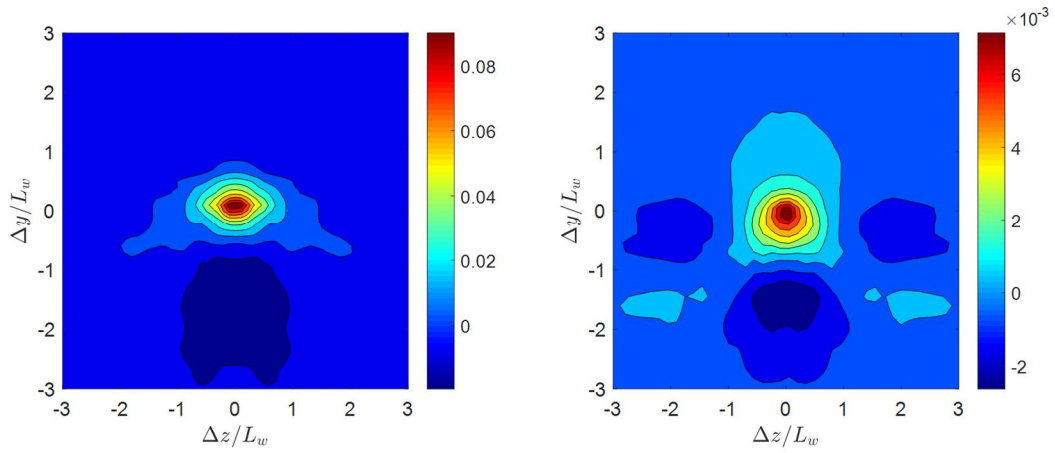


Figure C.36. R_{33} correlation comparison between the cylinder (left) and airfoil (right) wakes.

C.6 Zero Time Delay Correlation Comparison for an Anchor Point of $y/L_w = 2.5$

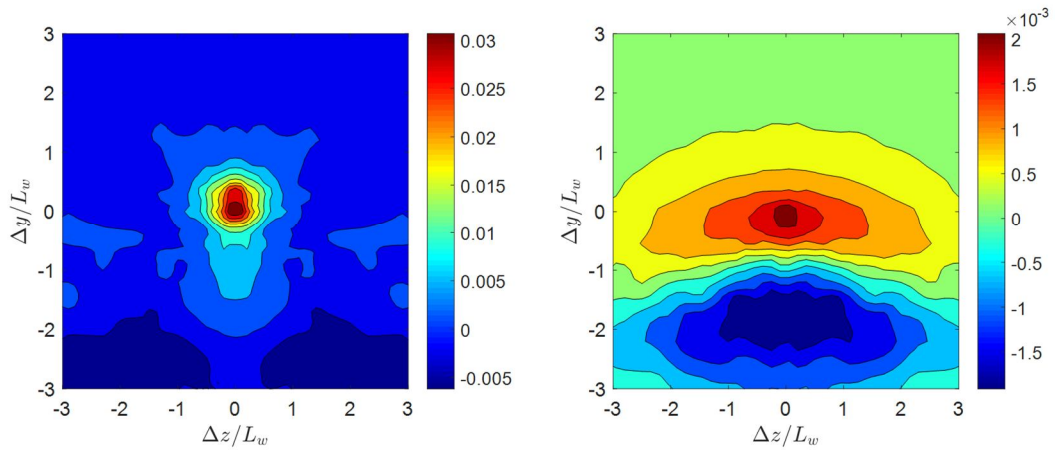


Figure C.37. R_{11} correlation comparison between the cylinder (left) and airfoil (right) wakes.

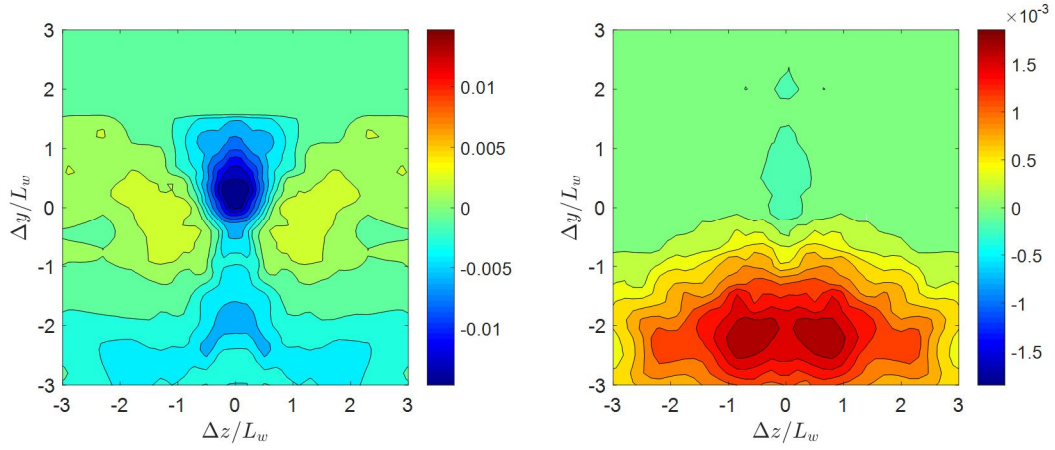


Figure C.38. R_{12} correlation comparison between the cylinder (left) and airfoil (right) wakes.

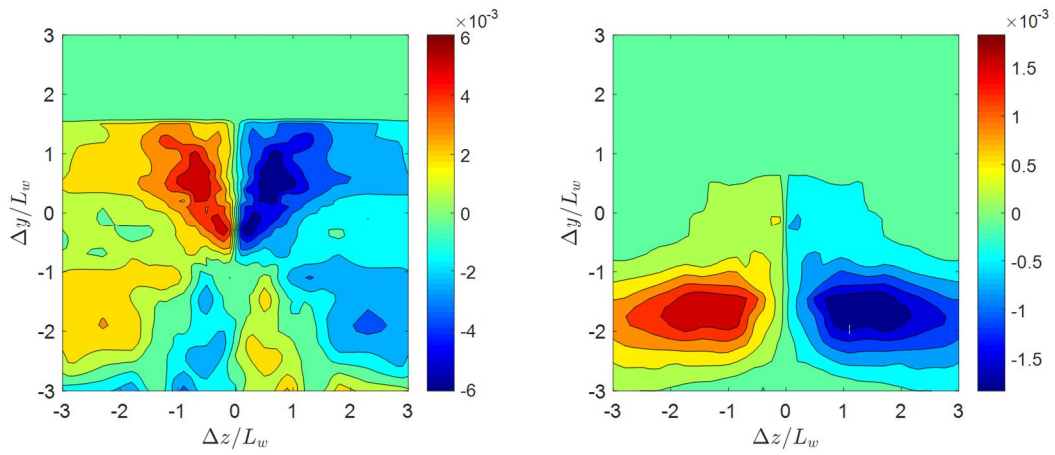


Figure C.39. R_{13} correlation comparison between the cylinder (left) and airfoil (right) wakes.

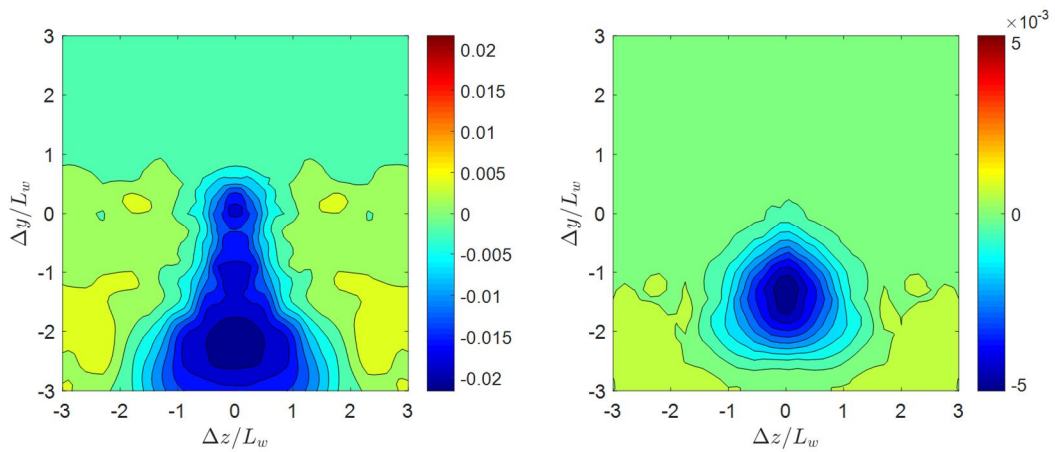


Figure C.40. R_{21} correlation comparison between the cylinder (left) and airfoil (right) wakes.

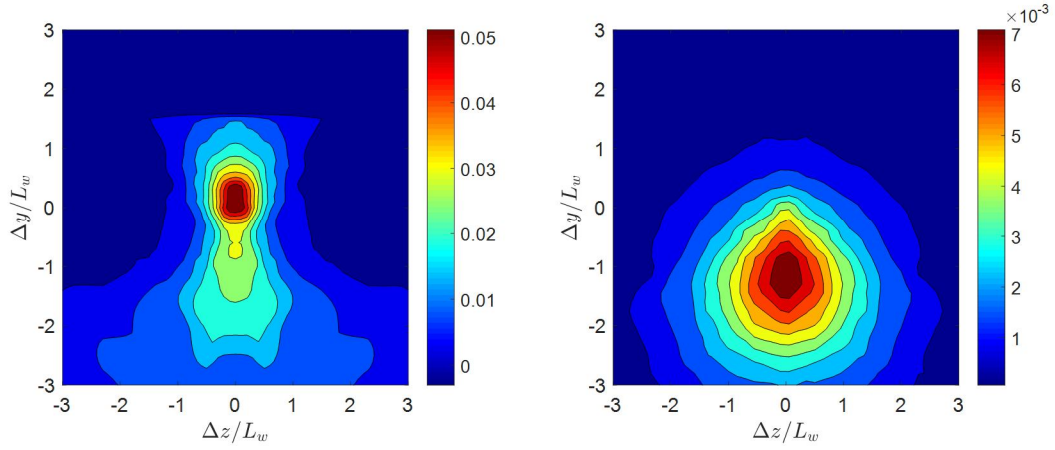


Figure C.41. R_{22} correlation comparison between the cylinder (left) and airfoil (right) wakes.

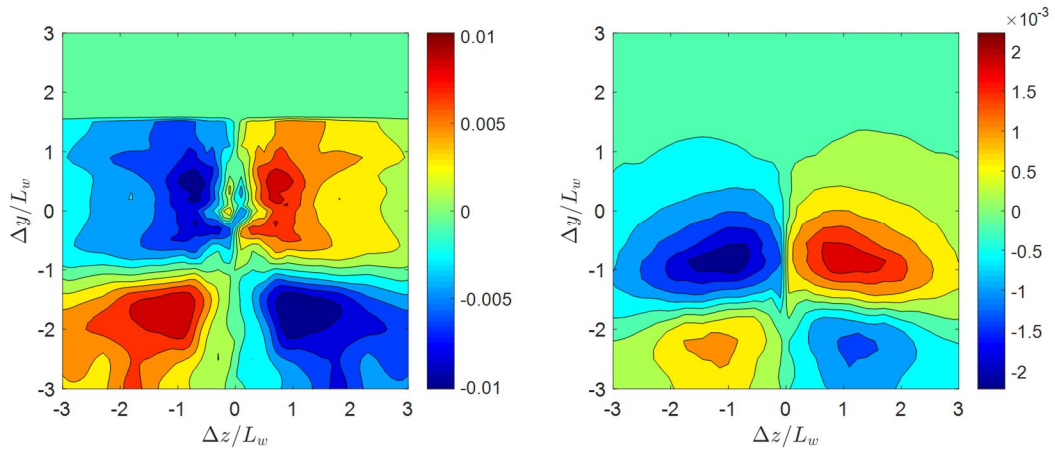


Figure C.42. R_{23} correlation comparison between the cylinder (left) and airfoil (right) wakes.

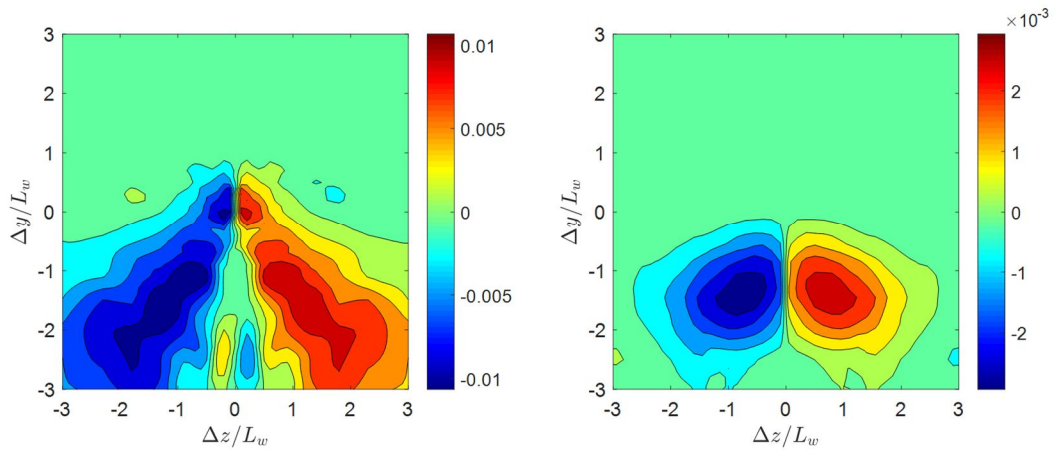


Figure C.43. R_{31} correlation comparison between the cylinder (left) and airfoil (right) wakes.

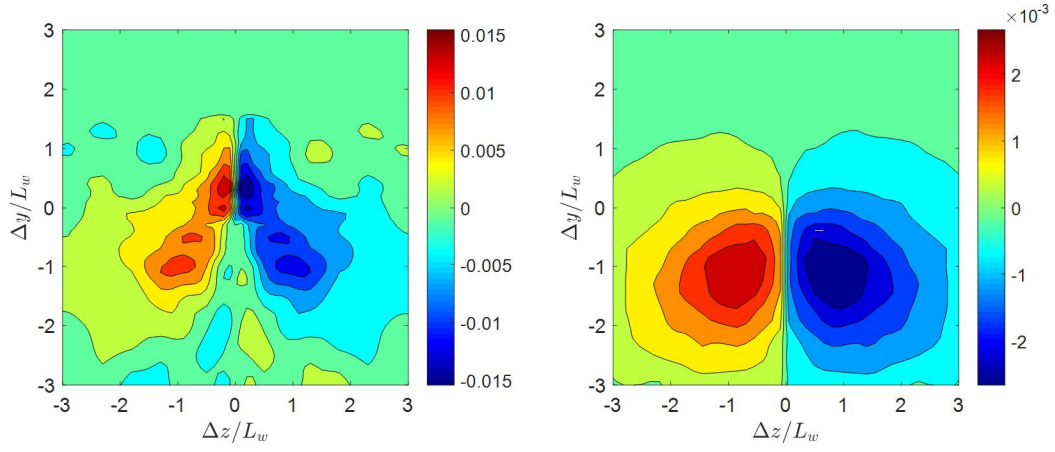


Figure C.44. R_{32} correlation comparison between the cylinder (left) and airfoil (right) wakes.

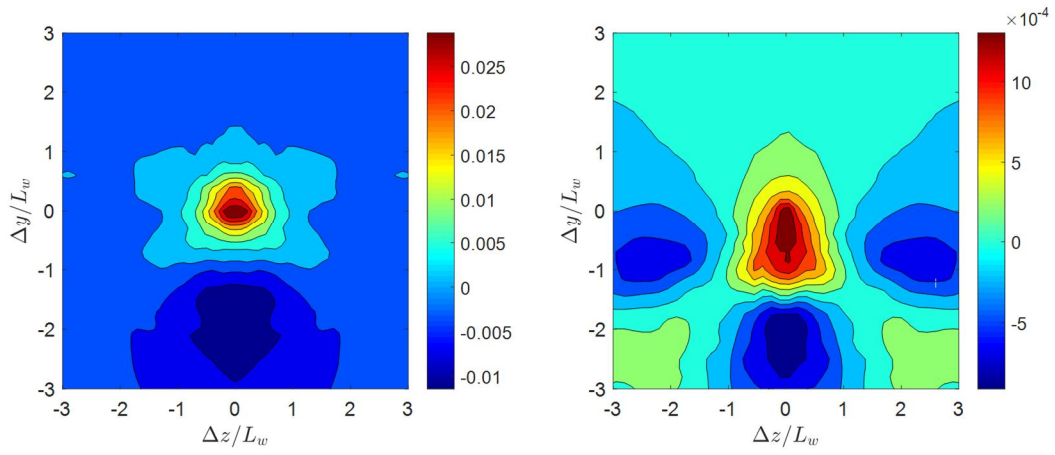


Figure C.45. R_{33} correlation comparison between the cylinder (left) and airfoil (right) wakes.